QUANTUM DYNAMICS OF EXCITED CHARGE CARRIER AT HETEROGENEOUS
INTERFACE BETWEEN SEMICONDUCTOR AND ORGANIC MOLECULE

Lesheng Li

A dissertation submitted to the faculty at the University of North Carolina at Chapel Hill in
partial fulfillment of the requirements for the degree of Doctor of Philosophy in the
Department of Chemistry.

Chapel Hill
2018

Approved by:

Yosuke Kanai

Max L. Berkowitz

Joanna M. Atkin

Jillian L. Dempsey

James F. Cahoon

ABSTRACT

Lesheng Li: Quantum Dynamics of Excited Charge Carrier at Heterogeneous
Interface between Semiconductor and Organic Molecule
(Under the direction of Yosuke Kanai)

Developing a quantitative understanding of excited charge carrier dynamics at heterogeneous interfaces between semiconductor and organic molecules is of great practical importance in advanced technologically important applications. Despite great advances in this field, there remain many aspects that are yet to be understood such as the density of charge carrier, the role of defects, and the interactions with surface ligand. To this end, we aim to develop and apply a quantitative formulation based on first-principles quantum theory to elucidate how excited carrier dynamics at semiconductor-molecule interfaces depend on the atomistic details.

In this work, we systematically investigated several aspects of excited carrier dynamics at semiconductor-molecule interfaces via first-principles quantum mechanics simulations that are synergistically combined with the fewest-switches surface hopping algorithm, G_0W_0 many-body perturbation theory calculations, and first-principles molecular dynamics. We conclude that hot electron transfer to chemisorbed molecules was observed but was short-lived on the molecules. Interfacial electron transfer was found to be largely decoupled from hot electron relaxation within the semiconductor. While hot electron relaxation was found to take place on a time scale of several hundred femtoseconds, the subsequent interfacial electron transfer was slower by an order of magnitude. Meanwhile, this secondary process of picosecond electron transfer was found to be comparable in time scale to typical electron trapping into defect states in the energy gap.

We then investigated how molecular details such as surface coverage and adsorbate species influence hot electron transfer. Counterintuitively, increasing surface coverage was found to suppress hot electron transfer probability because the increased delocalization of the hot electron accepting molecular states change the nonadiabatic couplings at the interface. In addition, the adsorbate species itself is an important factor in hot electron transfer not simply because of energy level alignments, but because the transfer is quite sensitive to nonadiabatic couplings.

Finally, we examined the extent to which exchange-correlation approximations influence the interfacial charge transfer at a representative heterogeneous interface. We showed how the charge transfer kinetics are influenced by the exchange-correlation approximation through lattice movement, nonadiabatic couplings, and energy level alignments. The interfacial electron transfer time scale was found to vary by as much as, but not more than, one order of magnitude.

To my parents, Yujiao and Anlin.
To Jingwen.

ACKNOWLEDGEMENTS

TABLE OF CONTENTS

LIST OF TABLES

LIST OF FIGURES

LIST OF ABBREVIATIONS

BET	Back-electron transfer
BO	Born-Oppenheimer
CBM	Conduction band minimum
CPA	Classical-path approximation
DFT	Density functional theory
DOS	Density of states
DSSC	Dye-sensitized solar cell
EA	Electron affinity
EOM	Equation of motion
ET	Electron transfer
FFT	Fast Fourier transform
FPMD	First-principles molecular dynamics
FSSH	Fewest-switches surface hopping
GGA	Generalized gradient approximation
G_0W_0	One-shot GW calculation
HET	Hot electron transfer
HF	Hartree-Fock
HOMO	Highest occupied molecular orbital
IE	Ionization energy, same as ionization potential
IET	Interfacial electron transfer
IP	Ionization potential, same as ionization energy
KS	Kohn-Sham

KS-DFT	Kohn-Sham Density functional theory
LHS	Left-hand side
LUMO	Lowest unoccupied molecular orbital
MBC	Many-body correction
MBPT	Many-body perturbation theory
MD	Molecular dynamics
NA	Nonadiabatic
NAC	Nonadiabatic coupling
NAMD	Nonadiabatic molecular dynamics
PBE	Perdew-Burke-Erzerhof
PBE0	Perdew-Burke-Erzerhof with 0.25 Hartree-Fock exchange
PDOS	Projected density of states
PES	Potential energy surface
PPA	Plasmon-pole approximation
QD	Quantum dot
QP	Quasi-particle
RHS	Right-hand side
RPA	Random-phase approximation
sc-GW	Self-consistent GW
TD-KS	Time-dependent Kohn-Sham
TSH	Trajectory surface hopping
VBM	Valence band maximum
XC	Exchange-correlation

CHAPTER 1: INTRODUCTION

When a photon with energy $\hbar\omega \geq E_g$ is first adsorbed by a semiconductor (with an energy band gap of E_g), the immediate aftermath is the photogeneration of an electron-hole pair.[1] In the single-particle description of quantum mechanics, excited electrons with excess energy above the conduction band minimum (CBM) of a material are called hot electrons.[1-2] Similarly, excited holes with energy below the valence band maximum (VBM) are called hot holes. The term *hot carrier* refers to the fact that prior to any scattering with lattice phonons, the photoexcited electron/hole has energy in excess of the fundamental band gap and thus is considered to be *hot*. Hot carriers lose their excess energy by *relaxation* within the manifold of the conduction/valence band electronic states through coupling with lattice phonons (i.e. atomic vibrations) to the band edges (VBM or CBM) as shown schematically in **Figure 1.1**.
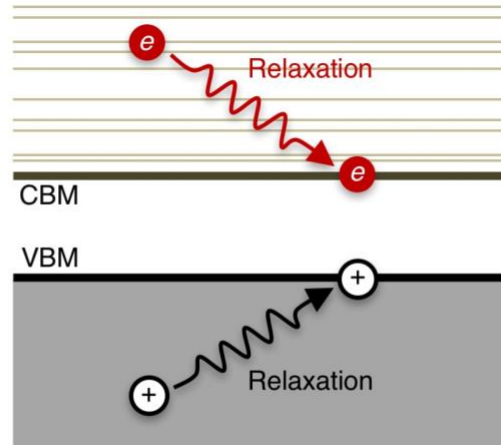
Figure 1.1 | Schematic representation of hot carrier relaxation within the manifold of semiconductor conduction/valence band electronic states.

This hot carrier relaxation process is of great practical importance in various optical and electronic device technologies[3-11] including solar energy conversion[10,12-13] and light emitting diodes (LEDs).[2,14-17] Also, it is a scientifically intriguing process in regard to the underlying physics associated with the coupling between the electronic and ionic degrees of freedom.
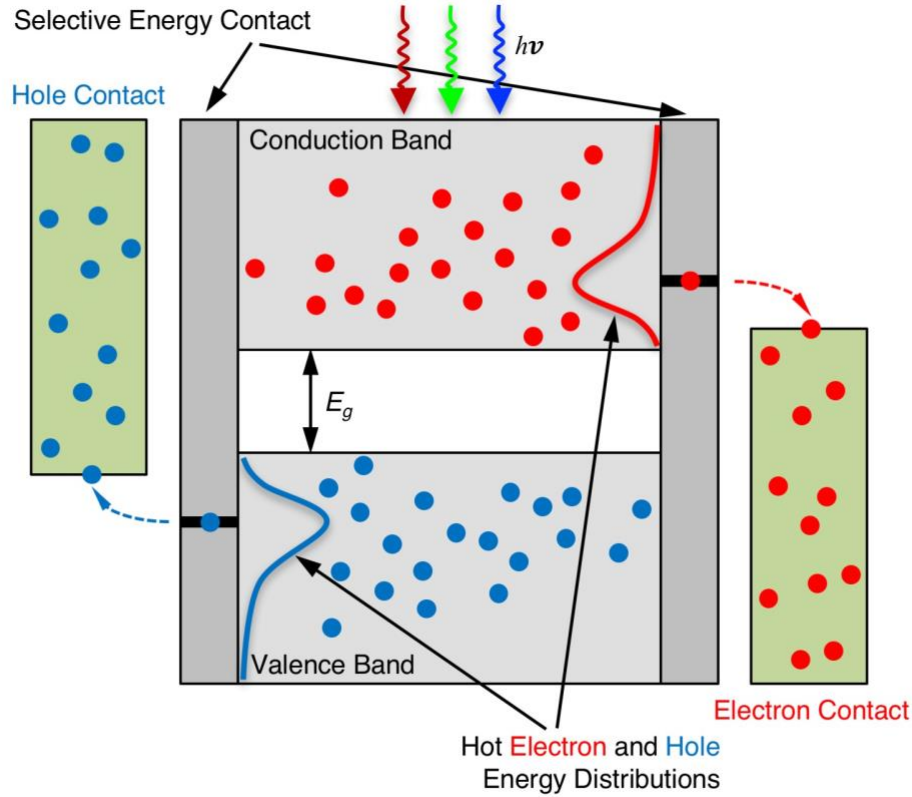
Figure 1.2 | Schematic and band diagram of an ideal hot carrier solar cell.

In the context of solar energy conversion (i.e. solar cells), the hot carrier relaxation process represents the dominant energy loss mechanism by which a significant portion of the absorbed solar energy is lost as heat. Therefore, with the intent of finding ways to reduce such a substantial relaxation loss component, the concept of hot carrier solar cell (HCSC) has emerged (**Figure 1.2**). When Ross and Nozik[12] first proposed the so-called hot carrier solar cell concept in 1982 as a

special class of solar cells, the idea was that one could take advantage of the photogenerated hot carriers (hot electrons and hot holes) before they have enough time to relax to the band edges (VBM for hot holes and CBM for hot electrons).[1,12] Thus, the practical realization of the concept for HCSC ultimately relies on finding a way to increase the relaxation time of the hot carriers so that they can be efficiently collected via the selective energy contact (SEC) to do work before losing their excess energy.[12,18]
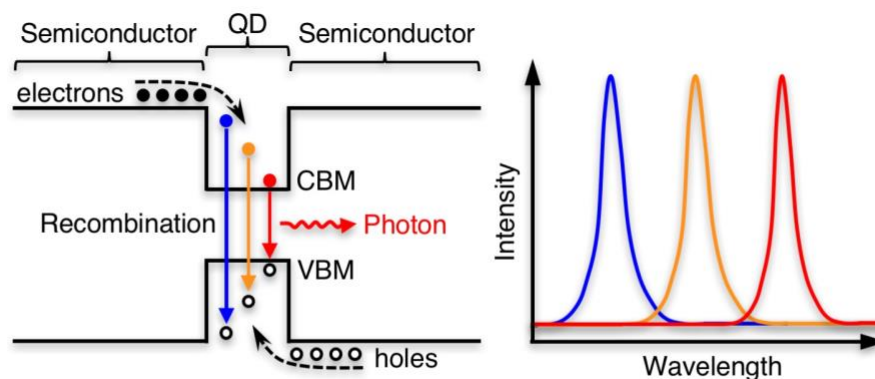
Figure 1.3 | Schematic diagram of hot carrier dynamics in the context of QD-LEDs and how it could affect the performance of QD-LEDs.

In the field of quantum dot light-emitting diodes (QD-LEDs),[14] where hot carriers are injected from electrodes into a semiconductor quantum dots (QDs) layer to yield electroluminescence (**Figure 1.3**), the idea is to have photoemission occurring only according to the fundamental energy gap of the material, i.e. between the CBM and VBM, or equivalently between the lowest unoccupied molecular orbital (LUMO) and the highest occupied molecular orbital (HOMO). In order for QD-LEDs to have a specific narrow emission wavelength for a particular size of the QDs, hot carriers need to be prevented from electron-hole recombination before they lose their excess energy to phonons. In other words, a fast relaxation process of the hot carriers is of the utmost

importance for QD-LEDs[2,19] in order that the excess energy of hot carriers can be transferred efficiently to photons instead of being wasted by phonons as illustrated in **Figure 1.3**.

Recognizing the critical role of hot carrier relaxation in different technologies, a quantitative description of hot carrier dynamics in semiconductor materials and even more complicated systems (such as semiconductor-molecule heterogeneous interfaces) has become important for designing materials for a particular technological aim. Therefore, considerable efforts have been dedicated to investigating hot carrier dynamics at various heterojunctions, such as QD core-shell,[20] semiconductor-QDs,[21-23] semiconductor-metal,[24-28] and semiconductor-molecule.[29-30] Despite great advances in this field, there remain many aspects that still not understood, such as the density of hot carriers,[31] the role of defects,[32-34] the size of the QDs,[35-36] and the interactions with the surface ligands.[37] Among these different factors that have been posited to control the hot carrier dynamics, the role of surface ligands, and more specifically the role of interfacial electron transfer (IET) across the heterogeneous interface, remains particularly unclear due to the substantial dependence on the specifics of the surface adsorbed molecules.[38-39] The fundamental understanding and quantitative characterization of the hot carrier dynamics at heterogeneous interface between an organic molecule and a semiconductor surface is of great interest in recent years especially because many nanomaterials have a large surface-to-volume ratio and the role of surface ligand becomes increasingly more important.[39] Such an understanding also helps to address various optoelectronic issues (e.g. non-radiative back reaction) that exist in the molecule-solid interfaces in popular photochemical solar cells. To this end, illustrating hot carrier dynamics at heterogeneous interfaces (such as IET processes) between a semiconductor material and organic molecules becomes critical to various technologically important applications, such as optical and electronic devices.[3-11]

4
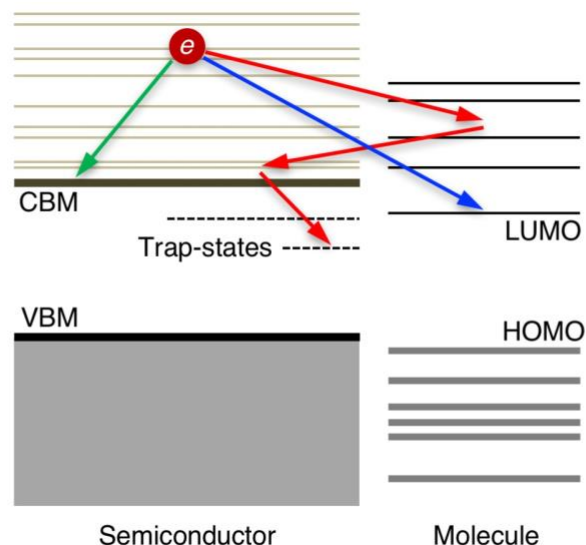
Figure 1.4 | Demonstration of the electronic energy level alignments at a typical semiconductor-molecule interface and how hot carrier processes could take place at such a heterogeneous interface.

The dynamics of excited electrons at the interface between a semiconductor material and adsorbed molecule are particularly relevant in photovoltaic (PV) and photoelectrochemical (PEC) devices that are based on the dye-sensitized solar cell (DSSC) concept.[3,40-41] Within DSSCs, an electron injected from an electronically excited adsorbate can undergo several distinct processes in the semiconductor,[42-43] including a rapid relaxation to the semiconductor CBM and drift under the internal electric field. The excited electron could also be trapped by localized electronic states below the semiconductor CBM, which are often associated with surface defects. This could be further followed by a number of additional processes such as electron-hole recombination, interfacial electron transfer, and de-trapping. No matter the order of these dynamical processes, transfer of the injected electron back to the oxidized molecule (or to the electrolyte molecule) is of great concern in DSSCs because the transfer negatively impacts device performance.[42,44-45] Although transient absorption spectroscopy measurements have been extensively used to investigate excited electron dynamics, isolating the spectral signatures and hot carrier dynamics

that are specific to distinctive dynamical processes is still challenging. This is because several dynamical processes with similar time scales[46] are operating simultaneously at the heterogeneous interfaces[42-43] during hot carrier relaxation, as illustrated in **Figure 1.4**.

These dynamical processes can occur in parallel, they compete with each other and ultimately determine the efficiency of the devices. Most importantly, the interplay among these kinetic processes that hot carriers can undergo significantly obfuscate the details of hot carrier dynamics.[47-48] In spite of the enormous amount of effort that researchers have devoted to semiconductor-molecule interfaces, many details of hot carrier dynamics that occur at interfaces remain unknown and are inherently challenging to uncover.[44] These difficulties originate from the fact that there exist two parts of interest involved in hot carrier dynamics at the semiconductor-molecule heterogeneous interfaces: (i) the semiconductor material and (ii) the surface molecules. The former is usually studied by solid-state physicists, while the latter is generally investigated by chemists.[49] Both aspects of these heterogeneous interfaces have their own areas of scientific interest: organic molecules have discrete localized electronic states, unique vibrational spectra, and well-defined directional bonds. Semiconductor materials, on the other hand, have continuous bands of delocalized electronic and vibrational states, can be easily modified and doped, and contain numerous defects that disrupt regular bonding patterns. In addition, the electronic structure of the semiconductor material is also affected by its size, shape, and morphology.[44] Realizing all of these difficulties, developing a comprehensive knowledge of the hot carrier dynamics in complex systems (such as heterogeneous interfaces between semiconductor material and organic molecules) calls for accurate modeling of excited carrier dynamics at the atomic level.

To this end, we aim to develop and apply a quantitative formulation based on first-principles (*ab initio*) quantum theory to elucidate how hot carrier processes at semiconductor-molecule

heterogeneous interfaces depend on the atomistic details, such as the molecular chemisorption, density of states (DOS) in the semiconductor conduction band, and the surface molecule. As we have discussed above, unlike charge transfer from the molecule to the semiconductor surface or hot carrier relaxation in bulk semiconductors, several dynamical mechanisms are operating simultaneously at the semiconductor-molecule interfaces and their relative importance is at the heart of elucidating the hot carrier process thoroughly. We turn to first-principles quantum theory simulations because they are able to provide a unique perspective on the interfacial electron dynamics and most closely mimic the processes as they can occur in nature.[44] First-principles simulation complements the simplified phenomenological models,[50-56] which allow us to systematically investigate the influence of various interface characteristics of the hot carrier dynamics by varying model parameters. The atomistic simulation treats the interfaces in full, realistic detail, and describes the evolving geometric and electronic structure of the organic molecule, the semiconductor surface, and the electrolyte in real time. The *ab initio* treatment of the interfaces makes it possible to avoid fitting parameters and to build the theory starting from the fundamental laws of physics.

While numerical simulation from first-principles will yield a wealth of detailed insights, key questions are how the hot carrier dynamics depends on the adsorption mode of the molecules, and what are the time scales associated with spatial localization of the carrier on the adsorbed molecule. Quantifying this localization time scale, for example, allows us to assess the importance of other possible processes such as radiative electron-hole recombination and redox reactions, and different technological applications rely on the difference in the characteristic time scales of these distinct processes. In the remainder of this dissertation, we will investigate hot carrier dynamics at

semiconductor-molecule heterogeneous interfaces from several aspects via first-principles quantum mechanics simulations.

First, we employ first-principles electron dynamics simulations to investigate how the molecular details influence the quantum dynamics of excited electrons at the semiconductor-molecule type-II heterojunctions. A representative interface between the hydrogen-terminated silicon (111) surface and a dye molecule cyanidin was investigated here because silicon, being the foundation of modern electronic devices, has been studied extensively in the past decade,[57-59] and continues to draw attention.[60] As we have discussed previously, the transfer of the injected electron back to the oxidized molecule (or to the electrolyte molecule) is of great concern in DSSCs because the transfer negatively impacts device performance.[42,44-45] This so-called back-electron transfer (BET) is often described using an effective two-state model, symbolically denoted as $Semiconductor(e^-) - Molecule^+ \rightarrow Semiconductor - Molecule$. With TiO_2 as the semiconductor material, BET is generally rate-limited by the intra-oxide hopping transport, and a very long time scale on the order of microseconds has been reported.[61-63] In some other cases, such as Sn-doped In_2O_3 nanoparticles (nanoITO), the electron transfer itself dominates the BET kinetics,[63] exhibiting a rather slow time scale on the order of nanoseconds.[64] The interplay among various competing mechanisms involved in the BET remains poorly understood. At the same time, recent experimental works revealed that interfacial electron transfer from semiconductor to adsorbed molecules could be quite fast with a time scale of several hundred femtoseconds, or even sub-hundred femtoseconds.[65] These fast interfacial electron transfer rate constants are quite distinct from the nanosecond to milliseconds time scale[62-63,66] that are typically observed for interfaces between molecules and typical oxide materials with defects. These ambiguities led us to investigate the "intrinsic" interfacial electron transfer process from the semiconductor to the

adsorbed molecule at a typical semiconductor-molecule interface. Using first-principles dynamics simulations, we show that the electron transfer can be quite fast when no defects are present to trap the hot electron at the semiconductor surface. Hot electron transfer to the chemisorbed molecule was observed but was short-lived on the molecule. Interfacial electron transfer to the chemisorbed molecule was found to be largely decoupled from hot electron relaxation within the semiconductor surface. While the hot electron relaxation was found to take place on a time scale of several hundred femtoseconds, the subsequent interfacial electron transfer was slower by an order of magnitude. At the same time, this secondary process of picosecond electron transfer is comparable in time scale to typical electron trapping into defect states in the energy gap. Contrary to popular belief, hot electron transfer is not the mechanism responsible for the ultra-fast electron transfer to the adsorbed molecule. This work is the subject of the paper published in *The Journal of Physical Chemistry Letters* **2016**, *7*, 1495.[30]

In addition, for the advanced applications that based on hot carriers such as photodetector,[67-70] photovoltaic (PV),[71-73] and photocatalysis,[74] hot electron transfer (HET) at heterojunctions between different materials plays a central role in the performance of the devices. Because understanding the HET process at a molecular level is central to realizing these novel applications, considerable efforts have been dedicated to investigating HET at various heterogeneous interfaces, such as quantum dot (QD) core-shell,[20] semiconductor-QDs,[21-23] semiconductor-metal,[24-28] and semiconductor-molecule.[29-30,75] Ultimately, one hopes to establish a "design principle" at the molecular level for controlling HET for various applications. Despite great advances toward developing a molecular-level understanding in this field, the interplay among various dynamical processes with distinct time scales that hot electron could potentially go through[42-43] complicates the development of a clear understanding of hot electron dynamics.[47-48] In our recent first-

principles quantum dynamics simulation of excited electrons, the HET process from semiconductor to adsorbed molecule was indeed observed.[30] This provided us with an atomistic model that we can use to study how the HET dynamics can be tuned at the atomistic level. Following this work, we went further to investigate whether or not one could manipulate the hot electron transfer process at semiconductor-molecule heterogeneous interfaces by tuning the molecular details such as surface coverage and adsorbate species. Counterintuitively, increasing surface coverage does not enhance the HET probability, but significantly suppress such a dynamical process. This is because the increased delocalization of the hot electron accepting molecular states change the nonadiabatic couplings at the interface. In addition, adsorbate species itself is an important factor in HET process not simply because of energy level alignments, but because the transfer is quite sensitive to the nonadiabatic couplings. Our work shows that controlling of nonadiabatic couplings at the molecular level, not only the energy level alignments as often assumed, is an essential factor in developing a "design principle" for enhancing hot electron transfer. This work is the subject of the paper recently submitted to *Physical Chemistry Chemical Physics*.

Realizing the decisive role of energy level alignments and nonadiabatic couplings in modeling excited electron dynamics at heterogeneous interfaces, we finally examine the extent to which the exchange-correlation (XC) approximation influences the interfacial charge transfer by considering a representative heterogeneous interface between an extended boron-nitride sheet and a lithium ion as an "extreme-case" scenario. As nonadiabatic molecular dynamics (NAMD) has become quite popular in recent years for investigating hot carrier dynamics at semiconductor-molecule interfaces, one widely employed NAMD approach for modeling excited electron dynamics is based on fewest-switches surface hopping (FSSH) simulations within the single-particle

description[44,46,61,76] from Kohn-Sham Density Functional Theory (KS-DFT).[77] Three important ingredients are obtained directly from first-principles electronic structure calculations based on DFT for performing the FSSH simulations: (i) nonadiabatic couplings (NACs), (ii) single-particle energy levels, and (iii) atomic trajectories (lattice movement). Therefore, the quantitative accuracy of such FSSH simulations ultimately depends on the XC approximation that is used in KS-DFT framework. Recently, Lin and Akimov reported that the PBE-GGA approximation overestimates NACs up to an order of magnitude in comparison to those computed from the HSE06/PBE0-GGA-hybrid functional by considering silicon hydride molecules and silicon QDs.[78] The XC-derived differences in the NACs magnitudes were found to be size-dependent, due to the asymptotic behavior of the corresponding correlation functionals. This work sheds a key insight into how the underlying DFT electronic structure calculations could influence the NAMD simulations. Therefore, we investigate how the charge transfer kinetics is influenced by the XC approximation through the lattice movements, nonadiabatic couplings, and energy level alignments at the interface. The PBE0 hybrid XC approximation was found to yield NACs that are significantly smaller than the values obtained from the PBE-GGA approximation by an order of magnitude for localized electronic states. This difference between the two XC functionals for the calculated NACs was found to derive mainly from the wave function characteristics rather than from the lattice movement although first-principles molecular dynamics trajectories, along which NACs are obtained, differ noticeably between the two XC functionals. Using the NACs and single-particle energy level alignments at different levels of theory (KS-DFT and G_0W_0), FSSH simulations were performed to model the electron transfer dynamics at the interface. The electron transfer time scale was found to vary as much as, but not more than, one order of magnitude. The time scale was found to be quite sensitive to both NACs and energy level alignments. While the order of

11

magnitude consistency for the charge transfer rate is encouraging even for this rather extreme model of heterojunction interface, continued advancement in electronic structure methods is required for quantitatively accurate determination of the transfer rate. This work is the subject of the paper published in *Journal of Chemical Theory and Computation* **2017**, *13*, 2634.

The remaining dissertation is organized as follows. CHAPTER 2 provides a background to the computational methods used throughout the dissertation, including fewest-switches surface hopping, density functional theory and Kohn-Sham picture, first-principles molecular dynamics, many-body perturbation theory with GW approximation, and the workflow for numerical simulation of hot carrier dynamics. CHAPTER 3 discusses the excited electron dynamics at a representative semiconductor-molecule type-II interfaces. CHAPTER 4 provides the discussion on how surface coverage and surface adsorbate species affect the hot electron transfer process from semiconductor to molecule. CHAPTER 5 investigates the exchange-correlation approximation dependence on interfacial charge transfer dynamics. The final chapter (CHAPETER 6) presents the conclusions related to the contents that included in this dissertation.

CHAPTER 2: THEORETICAL AND NUMERICAL METHODS

Hot charge carrier dynamics at semiconductor-molecule heterogeneous interfaces depend ultimately on several factors, such as the energy level alignments and the extent of quantum mechanical coupling between the electronic structures of the semiconductor material and the molecule. Therefore, developing a comprehensive knowledge of hot carrier processes calls for accurate modeling of excited electron dynamics at the atomistic level because impartial interpretation of spectroscopic measurements is challenging when various dynamical processes operate with similar time scales simultaneously at the interfaces.[46] To this end, nonadiabatic molecular dynamics (NAMD)[43,46,79-81] has become quite popular in recent years for investigating hot carrier dynamics at semiconductor-molecule interfaces.[30,43,75,82-84] While significant advancement has been made in simulating hot carrier dynamics from first-principles theory (no empirical parameters from experiments are employed) in the past few years,[43,75,82-87] such as using the fewest-switches surface hopping approach as described in the following section, the approach currently suffers from the practical limitation of having inaccurate description of interfacial electronic structure. In particular, the use of Kohn-Sham density functional theory (KS-DFT) is problematic for describing the energy level alignments at the heterogeneous interfaces in practice.[88-89]

In order to overcome the practical and formal limitation discussed above in the existing theoretical formulations, we introduce the following two improvements that are essential for the present investigations:

(1) Efficient calculation of nonadiabatic couplings, which describe the coupling of electrons to atomic vibrations, within first-principles molecular dynamics simulations.

(2) Incorporation of many-body interaction in the single-particle picture of independent electrons (i.e. quasi-particle description) through solving the Dyson's equation using many-body perturbation theory.

2.1 Fewest-Switches Surface Hopping

The concept of trajectory surface hopping (TSH) was originally proposed by Tully and Preston in 1971 to include nonadiabatic effects (such as nonadiabatic molecular collisions) into classical molecular dynamics (MD) as an extension.[90] Within TSH, nuclei are assumed to move classically on a single potential energy surface (PES) until an avoided surface crossing or other region of large nonadiabatic coupling is reached. At such points the trajectory is split into two branches, each of which follows a different PES. This treatment is different from classical MD where only one PES is used to calculate the forces acting on a particle. In Tully's formulation,[46,90] a system is prepared in a single adiabatic state, which determines the "active surface". Electrons are treated quantum mechanically, and evolve according to Schrödinger equation or Schrödinger-like equation. At each time step, the probability of an instantaneous transition of an electron between potential energy surfaces (i.e. a "hop") is determined based on a phenomenological hopping criterion. If a hop occurs, the active surface is redefined. The sudden switching of the electronic states is a feature of the standard surface hopping procedure.[90] In the original formulation of TSH, there are an indefinite number of hops that a particle could go through between potential energy surfaces, where the excessive hopping outside of the region of the electronic crossings essentially lead to dynamics that are more similar to a weighted average of the two adiabatic states. This can lead to

unphysical dynamics outside of the electronic crossings.[90] Later in 1990, Tully proposed an algorithm which minimizes the number of state switches, subject to maintaining the correct statistical distribution of state populations at all times.[46] Such an algorithm is therefore named as "fewest-switches surface hopping" (FSSH). Compared to the original TSH algorithm, the "fewest-switches" criterion is derived specifically to limit the electronic hops to the region of electronic crossings (i.e. with strong nonadiabatic couplings).

The FSSH approach[44,46,61,76] was further extended into a formulation based on the single-particle description within the so-called classical-path approximation (CPA) as formulated by Prezhdo and co-workers.[43-44] Here, instead of using many-body adiabatic states as in Tully's original surface hopping method, Prezhdo proposed the employment of single-particle wave functions as the states where the hops could take place. In addition, the CPA assumes a classical equilibrium path that is representative of the system's nuclei at all times and surface hops do not significantly influence the nuclear dynamics.

Within the single-particle FSSH approach, the instantaneous probability for an electron transition (hop) from state k to state j in time Δt is governed by

$$g_{kj}(t) = \left\{ \frac{2}{\hbar} \Im m \left(\rho_{kj} H_{jk} \right) - 2 \Re e \left(\rho_{kj} D_{jk} \right) \right\} \Delta t / \rho_{kk}(t) \qquad (2.1)$$

where ρ is the density matrix for the excited electron, D is the nonadiabatic coupling (NAC) matrix, and H is the single-particle Hamiltonian matrix for the excited electron. The probability for a stochastic hop from state k to state j is given by

$$P_{k \rightarrow j}(t) = \max(0, g_{kj}(t)) B_{k \rightarrow j}(t) \qquad (2.2)$$

and

$$B_{k \to j}(t) = \begin{cases} \exp\left(-\dfrac{\varepsilon_j - \varepsilon_k}{k_B T}\right) & if \ \varepsilon_j \geq \varepsilon_k \\ 1 & if \ \varepsilon_j \leq \varepsilon_k \end{cases} \tag{2.3}$$

where $\varepsilon_{k,j}$ are the single-particle energies for satisfying detailed balance.

The density matrix for an excited electron can be set up with density operator

$$\hat{\rho}(t) = |\phi(t)\rangle\langle\phi(t)| \tag{2.4}$$

where ϕ is the wave function of the excited electron. We can then obtain the time-evolution of the density matrix element by using the Liouville-von Neumann equation[91]

$$i\hbar \frac{d}{dt}\rho = [H, \rho] - i\hbar[D, \rho]. \tag{2.5}$$

The second term on the right-hand side arises because the electronic state depends on the (time-dependent) positions of classical nuclei. In the adiabatic basis, the time evolution of the density matrix element can be written as

$$i\hbar\dot{\rho}_{ij} = \sum_i \left[(\varepsilon_l \delta_{il} - i\hbar D_{il})\rho_{lj} - \rho_{il}(\varepsilon_l \delta_{lj} - i\hbar D_{lj}) \right] \tag{2.6}$$

where ε_l is the single-particle energies of state l, and D_{il} is the NAC matrix element between state i and state l. As shown in EQUATION 2.6, NACs and single-particle energies are the two essential ingredients in this approach, and they can be obtained from first-principles quantum mechanical calculations as follows.

2.1.1 Nonadiabatic couplings

The NACs can be expressed as

$$\begin{aligned} D_{ij} &= \left\langle \psi_i(R(t)) \left| \frac{\partial}{\partial t} \right| \psi_j(R(t)) \right\rangle \\ &= \left\langle \psi_i(R(t)) | \nabla_R | \psi_j(R(t)) \right\rangle \cdot \frac{dR}{dt} \end{aligned} \tag{2.7}$$

16

$$= \frac{\langle \psi_i(R(t)) | \nabla_R \widehat{H} | \psi_j(R(t)) \rangle}{\varepsilon_j(R(t)) - \varepsilon_i(R(t))} \cdot \frac{dR}{dt}$$

where D_{ij} is the NAC between two states i and j, $\psi_i(R(t))$ and $\varepsilon_i(R(t))$ are the single-particle

eigenfunction and eigenvalue for state i at the nuclear coordinate $R(t)$, and H is the Kohn-Sham

(KS) Hamiltonian. We implemented the numerical calculation of NACs using the time-derivative

by enforcing the phase continuity as described in refs 30,92-93. The NACs can be calculated

efficiently *on-the-fly* within the first-principles molecular dynamics (FPMD) simulations. We

follow the prescription by Hammes-Schiffer and Tully for calculating the NACs numerically, from

KS adiabatic wave functions at adjacent time steps.[76] In practice, the NACs are calculated at

discrete time steps, and accurate sampling is crucial because NAC becomes significant rather

infrequently for heterogeneous systems such as semiconductor-molecule interfaces. Inadequate

sampling of NAC therefore could qualitatively impact the electron dynamics. The *on-the-fly*

calculations in FPMD simulations allow us to obtain accurately sample NACs efficiently even for

very large systems containing a few thousand electrons.

2.1.2 Single-particle energies

Single-particle energy level alignments at semiconductor-molecule interfaces were modeled

using quasi-particle (QP) energies within the G$_0$W$_0$ approximation (details will be discussed in

SECTION 2.3). QP energies were obtained from

$$\varepsilon_i^{QP}(t) = \varepsilon_i^{KS}(t) + \left[1 - \left\langle \psi_i(t) \left| \frac{\partial \Sigma(\omega)}{\partial \omega} \right|_{\omega = \varepsilon_i} \right| \psi_i(t) \right\rangle \right]^{-1}$$

$$\cdot \langle \psi_i(t) | \Sigma(r, r'; \varepsilon_i) - v_{XC}(r)\delta(r - r') | \psi_i(t) \rangle$$

(2.8)

where $\varepsilon_i^{KS}(t)$ is the KS energies from FPMD simulations and Σ is the self-energy operator; the

second term on the right-hand side represents the many-body correction (MBC), $\Delta\epsilon_i(t)$, using the

KS wave functions $\psi_i(t)$ at time t. Because of the very high computational cost associated, even within the G$_0$W$_0$ approximation, it is computationally impractical to take into account the time-dependence of the QP energies. Instead, we obtain the many-body corrections on top of KS energies at the equilibrium geometry, and we apply the same (time-independent) many-body corrections to correct individual time-dependent KS energies to obtain the time-dependent QP energies along the atomic trajectory, i.e. $\Delta\epsilon_i(t) = \varepsilon_i^{KS}(t) + \Delta\epsilon_i(t = 0)$. We have examined the validity of this approximation for different interfaces as discussed in each chapter.

2.2 Density Functional Theory and the Kohn-Sham Picture

By using density functional theory (DFT), one can determine the electronic ground state and energy exactly, provided that the universal density functional $F(\rho)$ is known. The problem at present is practical rather than conceptual, because of the inherent difficulty in solving the full many-body problem. The main difficulty is that electrons interact among themselves via Coulomb two-body forces. As a consequence, the presence of an electron in one region of space influences the behavior of other electrons in other regions, so they cannot be considered as individual entities. This is called the *quantum many-body problem*. A convenient strategy is to separate the classical electrostatic energy (Hartree term) from the quantum mechanical exchange and correlation energy contributions.[94] Therefore, the energy of a many-body electronic system can be written in the following way:

$$E = T + V_{ext} + \frac{1}{2}\int \frac{\rho(r)\rho'(r')}{|r-r'|}drdr' + E_{xc} \qquad (2.9)$$

where T is the kinetic energy, V_{ext} is the interaction with external fields, the third term on the right-hand side is the classical electrostatic interaction energy corresponding to a charge distribution $\rho(r)$ (i.e. the Hartree term), and E_{xc} is the exchange and correlation energy which is defined as:

$$E_{xc} = \frac{1}{2} \int \frac{\rho(r)\rho(r')}{|r - r'|} [g(r,r') - 1] dr dr' \tag{2.10}$$

where $g(r,r')$ is the two-electron correlation function (which turns out to be the pair correlation function of electrons[95]). Within the Kohn-Sham approach,[96] a set of self-consistent independent-electron Schrödinger-like equations are solved to obtain the density and the total energy of the system, where an approximation for the exchange-correlation potential of the electrons is required for practical calculations. These equations are referred to as the Kohn-Sham (KS) equations:

$$\hat{H}_{KS} \varphi_i^{KS}(r) = \varepsilon_i^{KS} \varphi_i^{KS}(r) \tag{2.11}$$

where $\varphi_i^{KS}(r)$ are called KS orbitals, ε_i^{KS} are the eigenvalues of the KS orbitals, and $\hat{H}_{KS}$ is the KS Hamiltonian which can be expressed in the following form:

$$\hat{H}_{KS} = -\frac{1}{2}\nabla^2 + v_{ext}(r) + v_h(r) + v_{XC}(r) \tag{2.12}$$

where the first term is the kinetic energy, $v_{ext}(r)$ is the interaction with external field, $v_h(r)$ is the Hartree term, and $v_{XC}(r)$ is the exchange-correlation potential, which can be expressed as

$$v_{XC}(r) = \frac{\delta E_{XC}(\rho)}{\delta \rho(r)} \tag{2.13}$$

where the exchange-correlation energy term $E_{XC}(\rho)$ is a functional of the electron density ρ, and is often approximated in practice. In other words, KS equation is the one electron Schrödinger-like equation of a fictitious system of non-interacting electrons that generate exactly the same electron density as any given system of interacting electrons.[96] We should note that KS orbitals are the result of a mathematical construction devised in order to simplify the problem. Although they do not have an inherent physical meaning by themselves, we can use them to construct the electron density according to the following equation:

$$\rho(r) = 2 \sum_{i=1}^{N_s} |\varphi_i(r)|^2 \tag{2.14}$$

where we have chosen the closed shell situation, with the occupation numbers 2 for $i \leq N_s$ and 0 for $i > N_s$, with $N_s = N/2$, the number of doubly occupied orbitals.

As we have discussed in previous section, the probability of a hop in the FSSH method assumes the accuracy of nonadiabatic couplings as well as energy level alignments as shown in EQUATION 2.6. In a system such as the interface between a molecule and a semiconductor surface, the energy level alignments are very important in order to accurately describe the kinetic processes such as hot carrier dynamics. However, the absolute values according to KS-DFT calculations often show large errors compared to experiments, leading to less accurate energy level alignments. Thus, KS-DFT calculations may not provide the energy level alignments that are accurate enough to perform further surface hopping calculations. Another approach is to use many-body perturbation theory (MBPT) with the GW approximation. The Green's function represents the probability of observing an electron (or a hole) at position r, at time t given that there was an electron (a hole) at position r' at time t'. In this sense, it constitutes a generalization of the static pair correlation function $g(r, r')$ to the time domain. Once the Green's function of the many-electron system is obtained, then the total energy, electronic density, momentum distribution, density of states, electronic excitations, and any other properties of interest can be determined. Therefore, the energy correction from MBPT with the GW approximation can adjust the KS eigenvalues before performing surface hopping calculations, giving rise to a more accurate description of the hot carrier dynamics. Details of many-body perturbation theory within the GW approximation will be discussed in SECTION 2.4.

2.3 First-Principles Molecular Dynamics

First-principles molecular dynamics (FPMD), also referred to as *ab-initio* molecular dynamics (AIMD), is an approach to simulate the same dynamics as classical MD, but instead of pre-defining the potentials used throughout the simulation, the forces acting on the nuclei are calculated *on-the-fly* during the simulation using electronic structure theory. In this section, we will assume that all the nuclei (together with their core electrons) can be treated as classical particles. And we only consider the systems for which a separation between the classical motion of the atoms and the quantum motion of the electrons can be achieved, i.e. under the Born-Oppenheimer (BO), or adiabatic, approximation. Such an assumption is regularly made and is generally valid for many chemical systems.

To be concise, the BO approximation assumes that the motion of the electrons is entirely decoupled from the motion of the nuclei, and they can therefore be separated. This is because the time scale associated with the motion of nuclei is usually much longer than that of the electrons. For any given ionic configuration, it is possible to calculate the self-consistent electronic ground state, and consequently the forces acting on the ions by using the Hellmann-Feynman theorem.[97] The obtained ionic forces allow then to evolve the classical nuclei trajectories in time. Thus, the general approach of FPMD is to calculate the ground state electronic system based on a specific configuration of nuclei from a first-principles electronic structure calculation, and to advance the classical nuclei using Newton's equation of motion where forces can be determined from the ground state electronic structure. The force acting on the nuclei can be expressed as

$$F_I = -\nabla_I E_I = -\nabla_I [\langle \Psi_0 | H_e | \Psi_0 \rangle] \tag{2.15}$$

where ∇_I is the gradient in the electronic coordinates based on the displacement in the ion, Ψ_0 is the ground state many-body wave function, which is a Slater determinant of the single-particle

ground state KS orbital in the KS picture. Feynman showed that if the many-body wave function is an eigenfunction or a linear combination of eigenfunctions of the electronic Hamiltonian, $\hat{H}_e$, EQUATION 2.15 can be simplified to the following form[98]

$$M_I \ddot{\boldsymbol{R}}_I = -\langle \Psi_0 | \nabla_I \hat{H}_e | \Psi_0 \rangle \tag{2.16}$$

where M_I is the mass of the ion and $\ddot{\boldsymbol{R}}_I$ is the acceleration of the nucleus. Within the description of KS-DFT, $\hat{H}_e$ is the KS Hamiltonian and the forces can be determined for a specific nuclear configuration by evaluating the expression $\nabla_I \hat{H}_e^{KS}$. Therefore, a practical algorithm of FPMD could be summarized as follows:[97]

(1) Self-consistent solution of the KS equations for a given ionic configuration $\boldsymbol{R}_I$;

(2) Calculation of the forces acting on the ions via the Hellmann-Feynman theorem;

(3) Integration of the Newton's equations of motion for the nuclei;

(4) Update of the ionic configuration.

2.4 Many-Body Perturbation Theory

2.4.1 Many-body correction and quasi-particle description from GW calculations

In the context of quantum field theory, the quasi-particle energies describe the single-particle energies of the interacting excited electron/hole and they are accessible using the Green's function formalism.[99] By solving Dyson's equation with the so-called GW approximation to the self-energy operator Σ in the context of many-body perturbation theory (MBPT), the quasi-particle (QP) energies can be obtained by applying the many-body corrections (MBCs) on top of the KS eigenvalues

$$\varepsilon_k^{QP} = \varepsilon_k^{KS} + \frac{\langle \psi_k(R(t)) | \Sigma(\varepsilon) - v_{XC} | \psi_k(R(t)) \rangle}{Z(\varepsilon)} \tag{2.17}$$

where the second term at the right-hand side is the MBC and v_{xc} is the exchange-correlation potential in the KS Hamiltonian. Within GW approximation, self-energy operator Σ is obtained from the Green's function (G) and the screened Coulomb interaction (W), and Z is the renormalization factor which is a derivative of the self-energy operator with respect to the energy.

2.4.2 One-particle Green's function

One-particle Green's function (also called as single-particle Green's function)[99] is an important concept in computing electronic excitations, involving both adding and removing one electron from the system. By using this concept, one is able to obtain a better fit to experimental data of photoemission or inverse photoemission. The time-ordered one-particle Green's function is defined as

$$G^{(1)}(1,2) = -i\langle\Psi_0^N|\hat{T}\hat{\psi}(1)\hat{\psi}^\dagger(2)|\Psi_0^N\rangle \tag{2.18}$$

where $1 \equiv (r_1, t_1)$, and $2 \equiv (r_2, t_2)$ are Hedin's compact notations to indicate space coordinates r and time t, and Ψ_0^N is the ground state many-body wave function of the system containing N electrons, $\hat{T}$ is the time-ordering operator, $\hat{\psi}(r,t)$ and $\hat{\psi}^\dagger(r,t)$ are field operators in the Heisenberg representation for annihilation and creation operators, which destroy or create an electron at position r and at time t. Atomic units ($\hbar = m = e = 1$) are used here. The time-ordering operator $\hat{T}$ has the following format

$$\hat{T}[A(x)B(y)] = \begin{cases} A(x)B(y) & if \quad x_0 > y_0 \\ \pm B(y)A(x) & if \quad x_0 < y_0 \end{cases} \tag{2.19}$$

Here x_0 and y_0 denote the time-coordinates of points x and y. If $t_1 > t_2$ in EQUATION 2.18, then the Green's function $G^{(1)}$ gives the probability amplitude that a particle added to the system at time t_2 at position r_2 will be found at time t_1 at position r_1. On the other hand, if $t_2 > t_1$, then a particle is removed from the system and the Green's function describes the time-evolution of the

corresponding hole.[100] Hence the Green's function can be interpreted as a propagator of a state that involves adding or removing an electron or hole (as shown in **Figure 2.1**), which indicates that one can use the Green's function to describe the electron affinities and ionization potentials, and to simulate photoemission or inverse photoemission experiments.
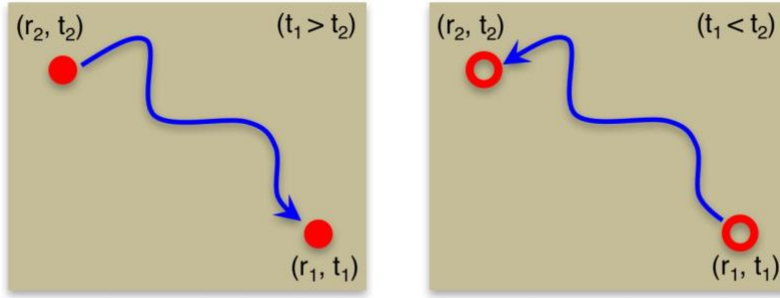
Figure 2.1 | Interpretation of the one-particle Green's function.

If we assume that the Hamiltonian and field operator are not an explicit function of time, we can show that the time-ordered Green's function will depend only on the time difference τ where $\tau = t_1 - t_2$, by using Schrödinger representation of the field operator

$$\hat{\psi}(1) = e^{i\hat{H}t}\hat{\psi}(1)e^{-i\hat{H}t} \tag{2.20}$$

and the relation

$$\hat{H}|N,0\rangle = E_{N,0}|N,0\rangle \tag{2.21}$$

where we used the short-hand notation of $|N,0\rangle$ to represent the ground state many-body wave function of a system with N electrons Ψ_0^N, we can represent the one-particle Green's function as

$$G^{(1)}(r_1,t_1,r_2,t_2) = G^{(1)}(r_1,r_2;\tau)$$

$$= -ie^{iE_{N,0}\tau}\langle N,0|\hat{\psi}(r_1)e^{-i\hat{H}\tau}\hat{\psi}^\dagger(r_2)|N,0\rangle\theta(\tau) \tag{2.22}$$

$$+ ie^{-iE_{N,0}\tau}\langle N,0|\hat{\psi}^\dagger(r_2)e^{i\hat{H}\tau}\hat{\psi}(r_1)|N,0\rangle\theta(-\tau)$$

EQUATION 2.22 is referred to as the Schrödinger representation of the one-particle Green's function.

2.4.3 Lehmann representation of the one-particle Green's function

In order to remove the time operators inside the expectation values of the Schrödinger representation of the one-particle Green's function in EQUATION 2.22, we insert into the one-particle Green's function a complete set of eigenstates of the system with M particles, $|M, n\rangle$, where n is a general label to describe the possible excited states for the system. Since the states form a complete set, we can write the closure relation

$$\sum_{M,n} |M, n\rangle\langle M, n| = 1 \tag{2.23}$$

and also

$$\widehat{H}|M, n\rangle = E_{M,n}|M, n\rangle \tag{2.24}$$

Introducing the closure relationship between the pairs of exponentials in the expression of the one-particle Green's function as in EQUATION 2.22, we have the following form:

$$G^{(1)}(r_1, r_2; \tau)$$

$$= -i \sum_{M,n} e^{i(E_{N,0} - E_{M,n})\tau} \langle N, 0|\widehat{\psi}(r_1)|M, n\rangle\langle M, n|\widehat{\psi}^\dagger(r_2)|N, 0\rangle \theta(\tau)$$

$$+ i \sum_{M,n} e^{-i(E_{N,0} - E_{M,n})\tau} \langle N, 0|\widehat{\psi}^\dagger(r_2)|M, n\rangle\langle M, n|\widehat{\psi}(r_1)|N, 0\rangle \theta(-\tau) \tag{2.25}$$

Most often, it is more convenient to work with the Fourier transform of the one-particle Green's function.

$$G^{(1)}(r_1, r_2; \omega) = \frac{1}{2\pi} \int_{-\infty}^{\infty} G^{(1)}(r_1, r_2; \tau) e^{i\omega\pi} d\tau \tag{2.26}$$

Therefore, EQUATION 2.25 can then be transformed to the following form via Fourier transform from the time domain to the frequency domain:

$$G^{(1)}(r_1, r_2; \omega) = \sum_{M,n} \frac{\langle N, 0 | \hat{\psi}(r_1) | M, n \rangle \langle M, n | \hat{\psi}^\dagger(r_2) | N, 0 \rangle}{\omega - (E_{M,n} - E_{N,0}) + i\eta}$$

$$+ \sum_{M,n} \frac{\langle N, 0 | \hat{\psi}^\dagger(r_2) | M, n \rangle \langle M, n | \hat{\psi}(r_1) | N, 0 \rangle}{\omega + (E_{M,n} - E_{N,0}) - i\eta}$$

(2.27)

where the infinitesimals $\pm i\eta$ reflect the time ordering, i.e. $i\eta$ means adding one electron and $-i\eta$ means removing one electron from the system. In addition, in EQUATION 2.27, the expectation value of $\langle N, 0 | \hat{\psi}(r_1) | M, n \rangle$ and $\langle M, n | \hat{\psi}^\dagger(r_2) | N, 0 \rangle$ are non-zero only when $M = N + 1$; while $\langle N, 0 | \hat{\psi}^\dagger(r_2) | M, n \rangle$ and $\langle M, n | \hat{\psi}(r_1) | N, 0 \rangle$ are different from zero only if $M = N - 1$. Thus, the one-particle Green's function can be written as

$$G^{(1)}(r_1, r_2; \omega) = \sum_{M,n} \frac{\langle N, 0 | \hat{\psi}(r_1) | N + 1, n \rangle \langle N + 1, n | \hat{\psi}^\dagger(r_2) | N, 0 \rangle}{\omega - (E_{N+1,n} - E_{N,0}) + i\eta}$$

$$+ \sum_{M,n} \frac{\langle N, 0 | \hat{\psi}^\dagger(r_2) | N - 1, n \rangle \langle N - 1, n | \hat{\psi}(r_1) | N, 0 \rangle}{\omega + (E_{N-1,n} - E_{N,0}) - i\eta}.$$

(2.28)

Let's first consider the energy terms appearing at the denominators in EQUATION 2.28, they can be written as

$$(E_{N+1,n} - E_{N,0}) = (E_{N+1,n} - E_{N+1,0}) + (E_{N+1,0} - E_{N,0})$$

(2.29)

and

$$-(E_{N-1,n} - E_{N,0}) = E_{N,0} - E_{N-1,n} = (E_{N,0} - E_{N-1,0}) + (E_{N-1,0} - E_{N-1,n})$$

(2.30)

The energy difference $E_{N+1,n} - E_{N,0}$ represents the minimum energy needed to add one electron to a system of N electrons. It is the electron affinity (EA):

$$EA = E_{N+1,n} - E_{N,0}$$

(2.31)

The energy difference $E_{N,0} - E_{N-1,n}$ represents the minimum energy needed to remove one electron from a system with N electrons. It is the ionization energy (IE) or ionization potential (IP):

$$IE = IP = E_{N,0} - E_{N-1,n} \tag{2.32}$$

It can be shown that $IE \leq EA$ so that if we define

$$\varepsilon_g = EA - IE = \left(E_{N+1,n} - E_{N,0}\right) - \left(E_{N,0} - E_{N-1,n}\right) \tag{2.33}$$

The quantity of ε_g is positive. Actually, for an atomic or molecular system, we have $IE\ (energy\ of\ HOMO) < EA\ (energy\ of\ LUMO)$; in a solid, we define the chemical potential μ such that $IE \leq \mu \leq EA$. Therefore, EQUATION 2.33 is always true. Now, coming back to the denominators in EQUATION 2.28, the first term at the right-hand side of EQUATION 2.29 is always positive or zero, and the second term at the right-hand side of EQUATION 2.29 is EA; the first term at the right-hand side of EQUATION 2.30 is IE, and the second term at the right-hand side of EQUATION 2.30 is always negative or zero. Here, we define a very useful term, the excitation energy of the system

$$\varepsilon_n = \begin{cases} E_{N,0} - E_{N-1,n}, & when\ \varepsilon_n < \mu \\ E_{N+1,n} - E_{N,0}, & when\ \varepsilon_n > \mu \end{cases} \tag{2.34}$$

Now, let's consider the numerators in the one-particle Green's function. If we define the Lehman amplitudes as

$$\phi_n(r) = \begin{cases} \langle N-1,n|\hat{\psi}(r)|N,0\rangle, & when\ \varepsilon_n < \mu \\ \langle N,0|\hat{\psi}(r)|N+1,n\rangle, & when\ \varepsilon_n > \mu \end{cases} \tag{2.35}$$

the numerators of the one-particle Green's function as in EQUATION 2.28 can be re-written as

$$\langle N,0|\hat{\psi}^\dagger(r_2)|N-1,n\rangle\langle N-1,n|\hat{\psi}(r_1)|N,0\rangle = \phi_n^*(r_2)\phi_n(r_1) \tag{2.36}$$

$$\langle N,0|\hat{\psi}(r_1)|N+1,n\rangle\langle N+1,n|\hat{\psi}^\dagger(r_2)|N,0\rangle = \phi_n(r_1)\phi_n^*(r_2) \tag{2.37}$$

Therefore, the one-particle Green's function in EQUATION 2.28 can be written as the following form

$$G^{(1)}(r_1, r_2, \omega) = \sum_n \frac{\phi_n(r_1)\phi_n^*(r_2)}{\omega - \varepsilon_n + i\eta sgn(\varepsilon_n - \mu)}. \tag{2.38}$$

EQUATION 2.38 is referred to as the Lehmann representation of Green's function. Here, η is a positive infinitesimal that is introduced to perform the Fourier transform, and sgn is the sign function. Within the Lehmann representation, the poles of the time-ordered single-particle Green's function represent the energies necessary to add or remove an electron. In general, these calculated energies are far from trivial, because when one electron is added to or removed from the system, all the other electrons will re-adjust accordingly. Therefore, Green's function $G^{(1)}$ can be used to represent all of these correlation effects.[100]

2.4.4 Equation of motion for one-particle Green's function

Starting from the equation of motion (EOM) for the Heisenberg annihilation and creation field operators ($\hat{\psi}^\dagger$ and $\hat{\psi}$), a hierarchy of EOM for one-particle Green's function can be derived. The detailed derivation of EOM for one-particle Green's function is given in APPENDIX A. For the one-particle Green's function, it gives

$$\left[i\frac{\partial}{\partial t_1} - H_0(r_1)\right]G^{(1)}(1,2) + i\int d3 \cdot v(1^+,3)G^{(2)}(1,3;2,3^+) = \delta(1,2) \qquad (2.39)$$

where

$$H_0(r_1) = -\frac{1}{2}\nabla^2 + V_{ext} \qquad (2.40)$$

and

$$v(1,2) = \frac{1}{|r_1 - r_2|}\delta(t_1 - t_2). \qquad (2.41)$$

Note that we have adopted Hedin's simplified notation $1 \equiv (r_1, t_1)$ and $1^+ \equiv (r_1, t_1 + \eta)$, where η is a positive infinitesimal. The $G^{(2)}$ term in EQUATION 2.39 is the two-particle Green's function which has the following formation:

$$G^{(2)}(1,2;3,4) = (i)^2\langle N,0|T[\hat{\psi}(r_1,t_1)\hat{\psi}(r_2,t_2)\hat{\psi}^\dagger(r_3,t_3)\hat{\psi}^\dagger(r_4,t_4)]|N,0\rangle. \tag{2.42}$$

The existence of two-particle Green's function in EQUATION 2.39 indicates that the one-particle Green's function depends ultimately on the two-particle Green's function. If we have a close look at the structure of the EOM for the one-particle Green's function, we can distinguish the first and second term in EQUATION 2.39 as the non-interacting and interacting terms, respectively. We assume that the non-interacting part can be always be solved exactly by

$$\left[i\frac{\partial}{\partial t_1} - \hat{H}_0(r_1)\right]G_0^{(1)}(1,2) = \delta(1,2) \tag{2.43}$$

which defines the independent-particle (non-interacting) Green's function G_0.

2.4.5 Hartree and Hartree-Fock approximation

Because we are only interested in the interacting term in the expression of EOM for the one-particle Green's function, let's look at it in details. Using EQUATION 2.41 and EQUATION 2.42, we can have the expression for the interacting term $\delta(t_1^+ - t_3)G^{(2)}(1,3;2,3^+)$

$$\begin{aligned}
&\delta(t_1^+ - t_3)G^{(2)}(1,3;2,3^+)\\
&\quad = (i)^2\langle N,0|T[\hat{\psi}(r_1,t_1)\hat{\psi}(r_3,t_1^+)\hat{\psi}^\dagger(r_2,t_2)\hat{\psi}^\dagger(r_3,t_1^{++})]|N,0\rangle
\end{aligned} \tag{2.44}$$

We can arrive at EQUATION 2.44 because if $\delta(t_1^+ - t_3) \neq 0$, then $t_1^+ = t_3$, thus we have

$$\hat{\psi}(r_3,t_3) = \hat{\psi}(r_3,t_1^+) \tag{2.45}$$

and

$$\hat{\psi}^\dagger(r_3,t_3^+) = \hat{\psi}^\dagger(r_3,t_1^{++}) \tag{2.46}$$

Now, the question is how to understand the interacting part $\delta(t_1^+ - t_3)G^{(2)}(1,3;2,3^+)$. Actually, we can re-write EQUATION 2.44 to the following form

$$\delta(t_1^+ - t_3)G^{(2)}(1,3;2,3^+)$$

$$= \delta(t_1^+ - t_3)\left[G^{(1)}(1,2)G^{(1)}(3,3^+) + G^{(1)}(1,3^+)G^{(1)}(3,2)\right] \tag{2.47}$$

where the first and second term in the bracket on the right-hand side is the direct term and exchange term, respectively. Finally, we can easily use **Figure 2.2** to interpret this interacting part, which indicates that each particle is allowed to propagate independently according to the one-particle Green's function.
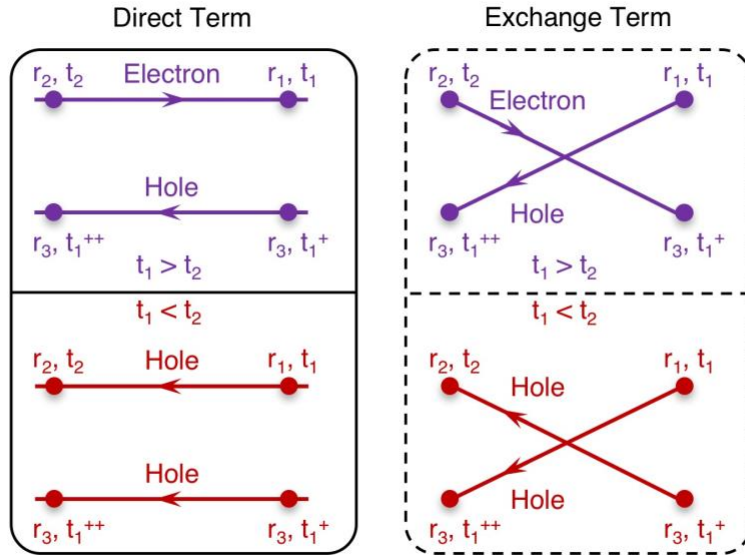
Figure 2.2 | Direct term and exchange term in the interacting part of the EOM for one-particle Green's function.

Let's first consider the direct term in the EOM for the one-particle Green's function as an approximation to the two-particle Green's function, i.e. just consider the direct part:

$$\delta(t_1^+ - t_3)G^{(2)}(1,3;2,3^+) = \delta(t_1^+ - t_3)\left[G^{(1)}(1,2)G^{(1)}(3,3^+)\right] \tag{2.48}$$

By doing so, we can have the EOM for the one-particle Green's function as the following form

$$\left\{\left[i\frac{\partial}{\partial t_1} - H_0(r_1)\right] + i\int d3 \cdot v(1^+,3)G^{(1)}(3,3^+)\right\}G^{(1)}(1,2) = \delta(1,2). \tag{2.49}$$

Note that the above expression is a simple independent-particle like equation, which is similar to the independent-particle Green's function G_0 that we had already discussed in EQUATION 2.43, but with an additional potential term, $i \int d3 \cdot v(1^+, 3) G^{(1)}(3, 3^+)$, which is nothing but a Hartree potential with the following formation

$$V_H(1) = i \int d3 \cdot v(1^+, 3) G^{(1)}(3, 3^+) = \int \frac{n(r_3, t_1)}{r_1 - r_3} dr_3 \qquad (2.50)$$

Then we can have the EOM for one-particle Green's function as:

$$\left[i \frac{\partial}{\partial t_1} - H_0(r_1) - V_H(1) \right] G^{(1)}(1, 2) = \delta(1, 2). \qquad (2.51)$$

The next step is to take both the direct and exchange terms as an approximation to the two-particle Green's function as shown in EQUATION 2.47. Inserting EQUATION 2.47 into EQUATION 2.39, we can have the EOM for one-particle Green's function as:

$$\left[i \frac{\partial}{\partial t_1} - H_0(r_1) - V_H(1) \right] G^{(1)}(1, 2) + i \int d3 \cdot v(1^+, 3) G^{(1)}(1, 3^+) G^{(1)}(3, 2)$$
$$= \delta(1, 2) \qquad (2.52)$$

where the interaction term is now a non-local operator. It can be shown that it is the Green's function variation of the exchange interaction appearing in the Hartree-Fock approximation.[100]

In order to have a good understanding of the direct and exchange terms, let's first have a look at the $V_H(1)$ term in EQUATION 2.51. $\delta(1, 2)$ is non-zero only if $1 \equiv 2$. Thus, the particle (electron/hole) is not going anywhere. This is actually a static state. The electron density at position r_3 at time t_1, $n(r_3, t_1)$ will affect the particle propagation from $2 \rightarrow 1$. Therefore, we can arrive at the expression for $V_H(1)$ as in EQUATION 2.50.

For the exchange term, instead of propagating from 2 directly to 1, it is also possible that the particle propagates from 2 to 3, and then to 1. Such a process can be illustrated in **Figure 2.3**. The

electron density at position r_3 at time t_1^+, $n(r_3, t_1^+)$ will affect the propagation from 3^+ to 1. Thus, we have the expression of $v(1^+, 3)$ in EQUATION 2.52.
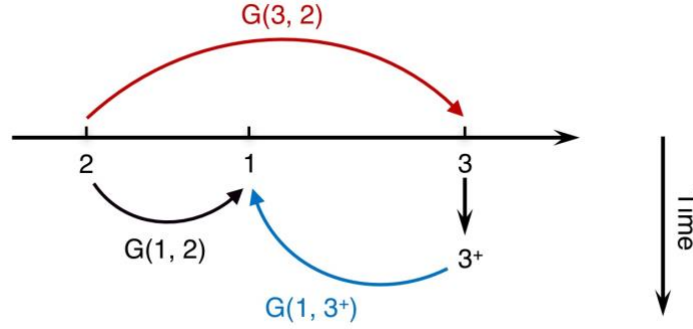
Figure 2.3 | Interpretation of the exchange term in the interacting part of the EOM for one-particle Green's function.

2.4.6 Self-energy operator

When we consider both the direct and exchange terms in the two-particle Green's function, we have the EOM of the one-particle Green's function as shown in EQUATION 2.52, now let's reform EQUATION 2.52 to the following form

$$\left[i\frac{\partial}{\partial t_1} - H_0(r_1) - V(1)\right]G^{(1)}(1,2) - i\int d3 \cdot \Sigma(1,3)G^{(1)}(3,2) = \delta(1,2) \qquad (2.53)$$

where Σ is the self-energy operator, and $V(1)$ can be expressed as

$$V(1) = \phi(1) + V_H(1) \qquad (2.54)$$

where $\phi(1)$ is any external potential (such as an experimental probe) that will vanish in the end. By comparing EQUATION 2.52 and EQUATION 2.53, one notices that we have used the self-energy operator Σ to approximate the $v(1^+, 3)G^{(1)}(1, 3^+)$ term. Thus, the particle is considered to move into a mean-field determined by the self-energy term Σ, which serves as an effective potential.

By using Fourier transform, we can re-write EQUATION 2.53 into the following form within energy domain

$$[\omega - H_0(r_1) - V(r,\omega)]G^{(1)}(r_1,r_2; \omega) - \int \Sigma(r_1,r_3; \omega)G(r_3,r_2; \omega)dr_3$$

$$= \delta(r_1 - r_2)$$

(2.55)

or adopting a matrix notation

$$(\omega - H_0 - V)G - \Sigma G = 1$$

(2.56)

Right multiply EQUATION 2.56 by G^{-1}, we can have the following relationship

$$G^{-1} = \omega 1 - H_0 - V - \Sigma$$

(2.57)

By comparing with the non-interacting expression as in EQUATION 2.49, we can further have

$$G^{-1} = G_0^{-1} - \Sigma$$

(2.58)

2.4.7 Dyson's equation and quasi-particle equation

From EQUATION 2.58, we can have the following expressions via left-multiply by G_0 and right-multiply by G:

$$G_0 G^{-1} G = G_0 G_0^{-1} G - G_0 \Sigma G$$

(2.59)

$$G_0 = G - G_0 \Sigma G$$

(2.60)

$$G = G_0 + G_0 \Sigma G$$

(2.61)

Here, EQUATION 2.61 is called the first-order Dyson's equation. We can also have Dyson's equation in a higher-order expansion from the second-order to the fourth-order:

$$G = G_0 + G_0 \Sigma (G_0 + G_0 \Sigma G)$$

(2.62)

$$G = G_0 + G_0 \Sigma [G_0 + G_0 \Sigma (G_0 + G_0 \Sigma G)]$$

(2.63)

$$G = G_0 + G_0 \Sigma \{G_0 + G_0 \Sigma [G_0 + G_0 \Sigma (G_0 + G_0 \Sigma G)]\}$$

(2.64)

For the first-order Dyson's equation, we can write it within the energy domain as

33

$$G^{(1)}(r_1, r_2; \omega) = G_0^{(1)}(r_1, r_2; \omega)$$

$$+ \int G_0^{(1)}(r_1, r_3; \omega) \Sigma(r_3, r_4; \omega) G^{(1)}(r_4, r_2; \omega) d(34) \tag{2.65}$$

We can also write it within the time domain as

$$G^{(1)}(1,2) = G_0^{(1)}(1,2) + \int G_0^{(1)}(1,3) \Sigma(3,4) G^{(1)}(4,2) d(34) \tag{2.66}$$

Here, $G_0^{(1)}$ is the Green's function of a mean-field system (that we have discussed in SECTION 2.4.6) defined by the single-particle Hamiltonian $\hat{h}_0$ with the following expression

$$\hat{h}_0 = H_0 + V_H \tag{2.67}$$

where H_0 and V_H are given in EQUATION 2.40 and EQUATION 2.50, respectively. We can understand this first-order Dyson's equation easily through the Feynman diagram[101] as shown in **Figure 2.4**.
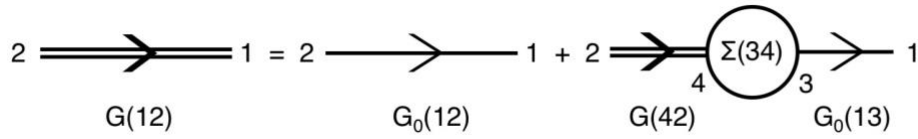
Figure 2.4 | Feynman diagram interpretation of the first-order Dyson's equation.

By inserting the Lehmann representation of Green's function as in EQUATION 2.38 into EQUATION 2.65, we see that the wave functions $\phi_n(r)$ and energies ε_n obey the quasi-particle equation with the following form (derivation of quasi-particle equation is detailed in APPENDIX B)

$$\hat{h}_0(r_1)\phi_n(r_1) + \int \Sigma(r_1, r_2; \varepsilon_n)\phi_n(r_2) dr_2 = \varepsilon_n \phi_n(r_1) \tag{2.68}$$

Although EQUATION 2.68 looks similar to the one-particle equations of mean-field approaches such as Hartree, Hartree-Fock or DFT, it does not constitute a mean-field formulation, since the self-energy takes all dynamic many-electron processes into account. Consequently, the wave functions

$\phi_n(r)$ and energies ε_n must not be understood as single-particle quantities. In fact, they are nothing but Lehmann amplitudes and excitation energies as defined in EQUATION 2.34 and EQUATION 2.35.

2.4.8 Hedin's equations and the GW approximation to the self-energy

Based on the Dyson's equation, we have already established a connection between the fully interacting propagator $G^{(1)}$ and the propagator $G_0^{(1)}$, where the latter is the non-interacting system through the self-energy. Through this connection, we reduced the problem of solving the Green's function $G^{(1)}$ to the calculation of the self-energy. However, as mentioned above, in the Hartree-Fock approximation of the self-energy Σ, no correlation effects have been taken into account. Thus, in order to introduce correlation effects, Hedin expressed the self-energy Σ in terms of the dynamically screened Coulomb potential W instead of the bare Coulomb potential v. W is given by:

$$W(1,2) = \int \epsilon^{-1}(1,3)v(3,2)d(3) \tag{2.69}$$

where ϵ^{-1} is defined as the inverse dielectric matrix, which describes the screening of the bare Coulomb potential due to all other electrons in the system. In 1965, Hedin[102-103] showed how to derive a set of coupled integral-differential equations whose self-consistent solution, in principle, gives the exact self-energy of the system. Therefore, one can use that self-energy to calculate the Green's function $G^{(1)}$. The following equations are Hedin's equations (a detailed derivation of Hedin's equations is given in APPENDIX C):

$$\Sigma(1,2) = i \int G(1,4)W(3,1)\Gamma(4,2;3)d(3,4) \tag{2.70}$$

$$G(1,2) = G_0(1,2) + \int G_0(1,3)\Sigma(3,4)G(4,2)d(3,4) \tag{2.71}$$

$$\Gamma(1,2;3) = \delta(1,2)\delta(1,3) + \int \frac{\delta\Sigma(1,2)}{\delta G(4,5)}G(4,6)G(7,5)\Gamma(6,7;3)d(4,5,6,7) \tag{2.72}$$

$$P = -i \int G(2,3)\Gamma(3,4;1)G(4,2)d(3,4) \tag{2.73}$$

$$W(1,2) = v(1,2) + \int v(1,3)P(3,4)W(4,2)d(3,4) \tag{2.74}$$

Here $v(1,2) = v(r_1, r_2)\delta(t_1 - t_2)$ is the bare Coulomb potential, Γ is the vertex function, P is the irreducible polarizability, and W is the screened Coulomb potential. We can easily use the diagram illustrated in **Figure 2.5** to understand the relationship among these parameters in Hedin's equations.
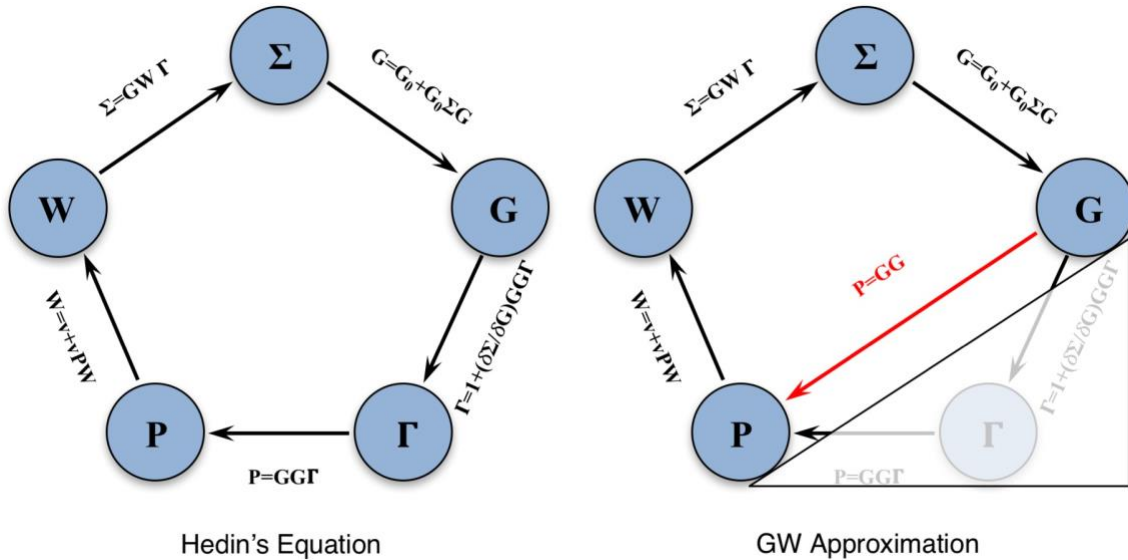
Figure 2.5 | Illustration of Hedin's equations (left) and the GW approximation (right).

In principle, Hedin's equations must be solved self-consistently to obtain the exact self-energy and the exact many-body single-particle Green's function $G^{(1)}$. However, from a computational

standpoint, obtaining the full self-consistent solution of Hedin's equations is a formidable task, even for a small molecule. A widely-used approach to approximate the solutions of Hedin's equations is the GW approximation, which starts by setting the self-energy Σ to 0, and one obtains:

$$\Gamma(1,2;3) = \delta(1,2)\delta(1,3). \tag{2.75}$$

This approximated vertex, once inserted in the full set of Hedin's equations, leads to a considerable simplification in the set of Hedin's equations. And due to the neglect of vertex corrections, the irreducible polarizability P now is expressed by:

$$P(1,2) = P_0(1,2) = -iG^{(1)}(1,2)G^{(1)}(2,1). \tag{2.76}$$

This equation defines P_0, which is the random-phase approximation (RPA) to the irreducible polarizability P, proposed by Adler[104] and Wiser.[105] Furthermore, the GW approximation (as shown in **Figure 2.5**) gives a first order expansion of the self-energy Σ of a simple direct product of the propagator $G^{(1)}(1,2)$ and the dynamically screened Coulomb potential W (1,2):

$$\Sigma(1,2) = iG^{(1)}(1,2)W(1,2). \tag{2.77}$$

Compared to the expression of self-energy within the Hartree-Fock approximation, a formal analogy between Hartree-Fock and GW is evident and is shown in **Table 2.1**.[100]

Table 2.1 | Comparison of the GW and Hartree-Fock approximations

GW approximation	Hartree-Fock approximation
Screened Coulomb potential	Bare Coulomb potential
$W(1,2) = \int \epsilon^{-1}(1,3)v(3,2)d(3)$	$v(1,2) = v(r_1,r_2)\delta(t_1 - t_2)$
GW self-energy	Hartree-Fock self-energy
$\Sigma(1,2) = iG^{(1)}(1,2)W(1,2)$	$\Sigma(1,2) = iG^{(1)}(1,2)v(1,2)$
Non-local	Non-local
Non-hermitian	Hermitian
Dynamic	Static

Ideally, the GW equations are iterated until self-consistency in all terms is reached; this is the fully self-consistent GW method (sc-GW). However, performing an sc-GW calculation even for very small system is still challenging. In addition, even though the sc-GW calculation can provide a more accurate total energy, the problem is that it will give worse spectral properties (such as band gaps and optical spectra), which is often the main reason why we use the GW method in the first place. For this reason, the most common approach employed in the *ab initio* community consists of using the best available approximation for $G^{(1)}$ and W as a starting point, and instead of iterating Hedin's equations, only perform one iteration of the equations. This is the so-called "one-shot" GW method (i.e. G_0W_0).[106-108] Since the Kohn-Sham (KS) orbitals are found to be very similar to the quasi-particle orbitals, the KS orbitals are used as the starting point for further G_0W_0 calculations.[100]
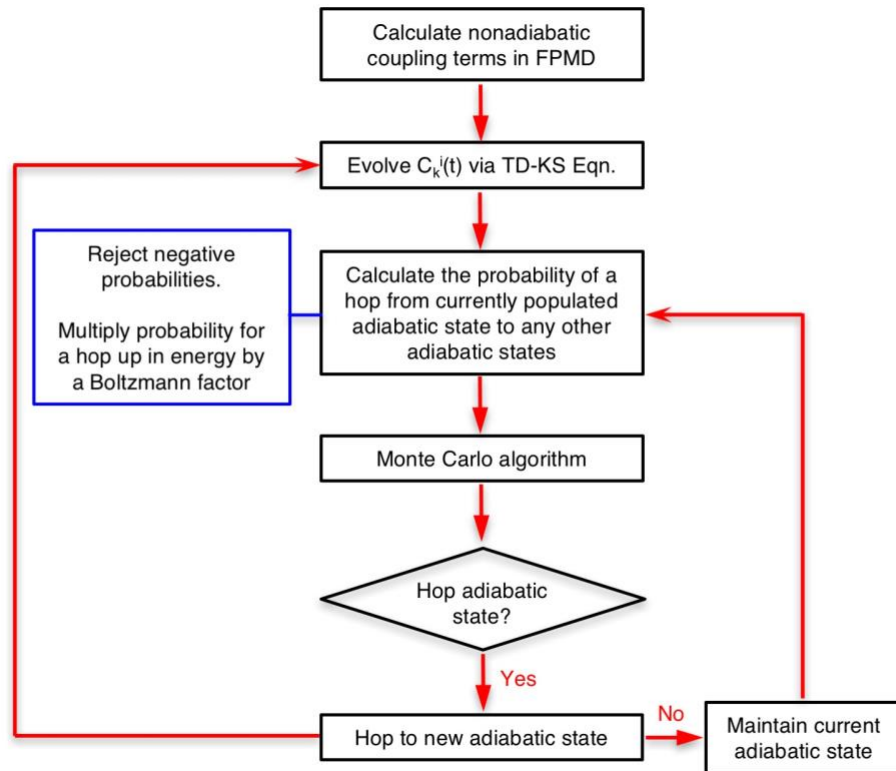
Figure 2.6 | Workflow of the numerical simulation for hot carrier dynamics.

2.5 Procedure for Simulating Hot Carrier Dynamics

With the necessary ingredients calculated from first-principle theory as discussed in the above sections, simulating hot carrier dynamics can be then performed in the following manner:

(1) Generate NACs by performing a FPMD simulation and obtain the quasi-particle energies by correcting KS energies via MBPT with G_0W_0 approximation.

(2) Evolve the expansion coefficients $c_k^i(t)$ according to the time-dependent KS equations.

(3) At each electron dynamics step in the fewest-switches surface hopping approach, calculate the hopping probability of the excited electron/hole to other electronic states and use Monte Carlo to execute the hop.

(4) Repeat the steps (2) ~ (3) to generate an ensemble of the hopping trajectories to yield adequate statistics of the overall nonadiabatic electron relaxation dynamics.

The workflow for simulating hot carrier dynamics is illustrated in **Figure 2.6**.

CHAPTER 3: EXCITED ELECTRON DYNAMICS AT SEMICONDUCTOR-MOLECULE TYPE-II HETEROJUNCTION INTERFACES

3.1 Introduction

Understanding excited electron dynamics at a heterogeneous interface is central to various optical and electronic device applications.[3-11] For instance, dynamics of highly excited electrons/holes (hot carriers) at such interfaces play an essential role in achieving high conversion efficiency in solar cells.[10,12-13] In addition to the solar energy conversion application, hot carrier dynamics at a heterojunction is of great interest also for optoelectronic applications such as light emitting diodes.[2,14-15] For instance, tailoring the coverage and type of the molecular passivation on nanoparticle surfaces enables control over the fluorescence efficiency of the nanoparticles.[16-17] Dynamics of excited electrons at the interface between a semiconductor material and adsorbed molecule is particularly important for photovoltaic (PV) and photo-electrochemical (PEC) devices that are based on the dye-sensitized solar cell (DSSC) concept.[3,40-41] Within DSSCs, the electrons injected from the electronically excited adsorbate undergo several distinct processes in the semiconductor,[42-43] including a rapid relaxation to the semiconductor conduction band minimum (CBM) and drift under the internal electric field. The excited electrons can also be trapped by localized electronic states below the CBM, which are often associated with surface defects. This could be further followed by a number of additional processes such as electron-hole recombination,

interfacial electron transfer, and de-trapping.

No matter the order of these dynamical processes, transfer of the injected electron back to the oxidized molecule (or to the electrolyte molecule) is of great concern in DSSCs, negatively impacting device performance.[42,44-45] This so-called back electron transfer (BET) is often described using an effective two-state model, symbolically denoted as Semiconductor (e⁻)-Molecule⁺→Semiconductor-Molecule. With TiO_2 as the semiconductor material, BET is generally rate-limited by the intra-oxide hopping transport, and a very long time scale of microseconds has been reported.[62-63,66] In some other cases, such as Sn-doped In_2O_3 nanoparticles (nanoITO), the electron transfer itself dominates the BET kinetics,[63] exhibiting a rather slow time scale of nanoseconds.[64] The interplay among various competing mechanisms involved in the BET remains poorly understood.

At the same time, there are a number of ultrafast spectroscopy experiments on related interfaces. Lian and co-workers have demonstrated that interfacial electron transfer to the adsorbed molecules could be very fast for small PbS quantum dots (QDs) with diameters of ~3.6 nm (with the time scale of ~370 fs)[109] and CdSe QDs with diameters of ~3 nm (with the time scale of ~60 fs).[65] More recently, Okano et al. have investigated the excited electron dynamics at a CdS/CdTe Type-II heterojunction within individual nano-rods, which were synthesized by anion exchange in CdS nano-rods.[110] Upon electronic excitation in the CdTe side, a majority of the hot electrons were found to relax to the CBM within several hundred femtoseconds. Essentially no hot electron transfer to the CdS side was observed. The interfacial electron transfer was found to take place after the hot electron relaxation on a time scale of 450 fs.

These recent experimental observations pose the question of how fast the "intrinsic" interfacial electron transfer from the semiconductor to the adsorbed molecule is at a typical semiconductor-

molecule interface. While significant advancements have been made for simulating hot carrier dynamics from first-principles theory in the last several years,[43,75,82-87] detail studies on elucidating hot carrier dynamics at semiconductor-molecule interfaces remain scarce, partly due to the difficulties in describing their electronic structure accurately for such large systems.[100] In this chapter, using first-principles electron dynamics simulations, we show that the intrinsic electron transfer to the adsorbed molecule can be quite fast when no defects are present to trap the hot electron at the semiconductor surface.

3.2 Computational Details and Interface Models

3.2.1 Computational details

Fewest-switches surface hopping (FSSH) simulation was performed in the single-particle description within the so-called classical-path approximation (CPA) as formulated by Prezhdo and co-workers.[43-44] The CPA assumes a classical equilibrium path that is representative of the system's nuclei at all times and surface hops do not significantly influence the nuclear dynamics. The validity of CPA in the context of this work is discussed in the SECTION 3.2.2. In CHAPTER 2, we have discussed that the single-particle energy and nonadiabatic couplings (NACs) are the two essential ingredients in this approach, and they are obtained from first-principles quantum mechanical calculations as follows.

(1) NAC matrix is calculated using

$$D_{ij} = \left\langle \Psi_i(R(t)) \middle| \nabla_R \middle| \Psi_j(R(t)) \right\rangle \cdot \frac{dR}{dt}$$
$$= \left\langle \Psi_i(R(t)) \middle| \frac{\partial}{\partial t} \middle| \Psi_j(R(t)) \right\rangle$$

(3.1)

We implemented the numerical calculation of NACs using the time derivative by enforcing the phase continuity as in ref 92. NACs can be calculated efficiently on-the-fly within first-principles

molecular dynamics (FPMD) simulation. We follow the prescription by Hammes−Schiffer and Tully for calculating the NACs numerically, from the Kohn-Sham (KS) adiabatic wave functions at adjacent time steps.[76] We found that the time step of 0.48 fs in the FPMD is sufficient to accurately compute the NACs as discussed in the SECTION 3.2.3. The generalized gradient approximation of Perdew−Burke−Ernzerhof (PBE)[111] was used for the exchange-correlation potential, and the KS states were expanded in a plane wave basis using norm-conserving pseudopotentials[112] with kinetic energy cutoff of 50 Ry. The first-principles molecular dynamics (FPMD) simulations were performed with the Qbox code[113] for 2 ps at 295 K.

(2) Single-particle energy level alignment at the semiconductor-molecule interfaces was modeled using quasiparticle (QP) energies within the G_0W_0 approximation. QP energies were obtained from

$$
\varepsilon_i(t) = \varepsilon_i^{KS}(t) + \left[1 - \left\langle \Psi_i \left| \frac{\partial \Sigma(\omega)}{\partial \omega} \right|_{\omega=\varepsilon_i} \right| \Psi_i \right\rangle \right]^{-1}
$$

$$
\cdot \langle \Psi_i | \Sigma(r, r'; \varepsilon_i) - V_{XC}(r)\delta(r - r') | \Psi_i \rangle
$$

(3.2)

where $\varepsilon_i^{KS}(t)$ is the KS energies from FPMD simulations and Σ is the self-energy; the second term represents the many-body correction (MBC) using the KS wave functions, Ψ_i, at the equilibrium geometry (details are discussed in SECTION 3.2.4). Quantum Espresso code[114] was used to obtain the KS wave functions. The many-body corrections were calculated using many-body perturbation theory within the "one-shot" G_0W_0 approximation,[108] starting from PBE KS wave functions and eigenvalues within random phase approximation. The G_0W_0 calculations were performed using Yambo code,[115] where the Godby−Needs plasmon-pole model[116-117] was used in calculating the dielectric function. Convergence tests on various parameters were performed and are discussed in SECTION 3.2.5.

The FSSH simulation was then performed within the CPA approximation as discussed above. This allows us to use a large number of nuclear trajectories for converging the ensemble averaged quantities because the nuclear trajectories do not depend on the hops within the CPA. First, 2116 nuclear trajectories were generated from the FPMD simulation, and each of these 1 ps long trajectories start with different positions and momenta of the FPMD simulation. Then, 500 FSSH simulations were performed for each nuclear trajectory, converging the sampling of hopping probability distribution using the Monte Carlo method (details are discussed in SECTION 3.2.6).

3.2.2 Error introduced by classical-path approximation

Because the excited electron transfers into the chemisorbed molecule as a hot carrier, we need to examine the extent to which the Classical-Path Approximation (CPA) is appropriate as discussed in CHAPTER 2. The excited electron in the chemisorbed molecule might cause the chemisorbed molecule to significantly alter the atomic positions, and this geometrical effect cannot be captured within CPA. We compared the following two cases to assess the appropriateness of CPA in our simulations:

(1) Standard deviations of atomic positions in FPMD simulations at room temperature for the chemisorbed molecule cyanidin at H-Si(111):cyanidin interface.

(2) Displacements of atomic positions of a cyanidin molecule (but hydrogen atoms are used to saturate the cleaved bonds) when the molecule is geometrically relaxed with an extra electron in a specific molecular state that corresponds to states 87/88 (the molecular state with significant hot electron population during relaxation) in the interface structure for monodentate/bidentate cases. The occupation of the electronic states was held fixed with

44

Table 3.1 | Monodentate: Standard deviation on atomic positions of the chemisorbed cyanidin molecule in FPMD simulations of the interface structure, and displacements of atomic positions of an isolated cyanidin molecule induced by having an extra electron in a specific molecular state that corresponds to #87 in the interface case.

As part of semiconductor-molecule interface in FPMD		Geometry relaxation induced by having an extra electron in the molecular state that corresponds to #87 state	
Atom	Standard Deviation (Å)	Atom	Displacements (Å)
1C	0.036487	1C	0.056706
2C	0.283306	2C	0.081123
3C	0.239654	3C	0.045784
4C	0.196484	4C	0.029661
5C	0.551888	5C	0.036823
6C	0.346555	6C	0.024060
7C	0.343811	7C	0.045505
8C	0.803117	8C	0.022756
9C	0.952087	9C	0.014274
10C	0.779498	10C	0.023341
11C	0.745119	11C	0.010787
12C	1.632180	12C	0.026771
13C	1.038640	13C	0.034565
14C	1.537290	14C	0.012587
15C	2.088770	15C	0.011473
16H	1.135280	16H	0.114029
17H	1.396730	17H	0.029925
18H	0.839628	18H	0.036701
19H	1.704180	19H	0.034258
20H	2.343450	20H	0.035349
21H	1.937400	21H	0.009907
22H	1.630590	22H	0.022139
23H	3.989730	23H	0.018628
24H	1.523440	24H	0.050554
25H	0.649686	25H	0.026543
26O	0.077913	26O(fixed)	0.000000
27O	1.134150	27O	0.041367
28O	0.536762	28O	0.041723
29O	1.692370	29O	0.018344
30O	3.709020	30O	0.036700
31O	1.388940	31O	0.034703
		32H(fixed)	0.000000

an extra electron, and the geometry was optimized from the equilibrium structure that was

obtained without the excited electron.

Table 3.2 | Bidentate: Standard deviation on atomic positions of the chemisorbed cyanidin molecule in FPMD simulations of the interface structure, and displacements of atomic positions of an isolated cyanidin molecule induced by having an extra electron in a specific molecular state that corresponds to #88 in the interface case.

As part of semiconductor-molecule interface in FPMD		Geometry relaxation induced by having an extra electron in the molecular state that corresponds to #88 state	
Atom	Standard Deviation (Å)	Atom	Displacements (Å)
1C	0.113277	1C	0.083856
2C	0.089788	2C	0.088284
3C	0.176338	3C	0.072768
4C	0.239668	4C	0.056896
5C	0.345740	5C	0.057875
6C	0.289896	6C	0.085414
7C	0.293349	7C	0.056098
8C	0.527849	8C	0.042021
9C	0.653869	9C	0.041914
10C	0.192815	10C	0.033608
11C	0.368746	11C	0.028730
12C	0.257141	12C	0.029285
13C	0.638961	13C	0.016701
14C	0.438039	14C	0.029445
15C	0.213326	15C	0.019771
16H	0.624682	16H	0.039844
17H	0.532289	17H	0.074917
18H	1.957660	18H	0.028118
19H	0.607153	19H	0.027235
20H	1.248440	20H	0.057500
21H	0.484836	21H	0.119726
22H	1.799600	22H	0.203433
23H	0.306345	23H	0.076143
24H	0.811631	24H	0.030338
25O	0.171692	25O(fixed)	0.000000
26O	0.147775	26O(fixed)	0.000000
27O	0.311093	27O	0.029850
28O	1.007290	28O	0.013274
29O	0.410534	29O	0.032269
30O	1.602260	30O	0.032014
		31H(fixed)	0.000000
		32H(fixed)	0.000000

The atomic positions of 26O (link atom between the Si(111) surface and the molecule) and

32H (which replaces the surface silicon atom that connects to 26O) were held fixed at the
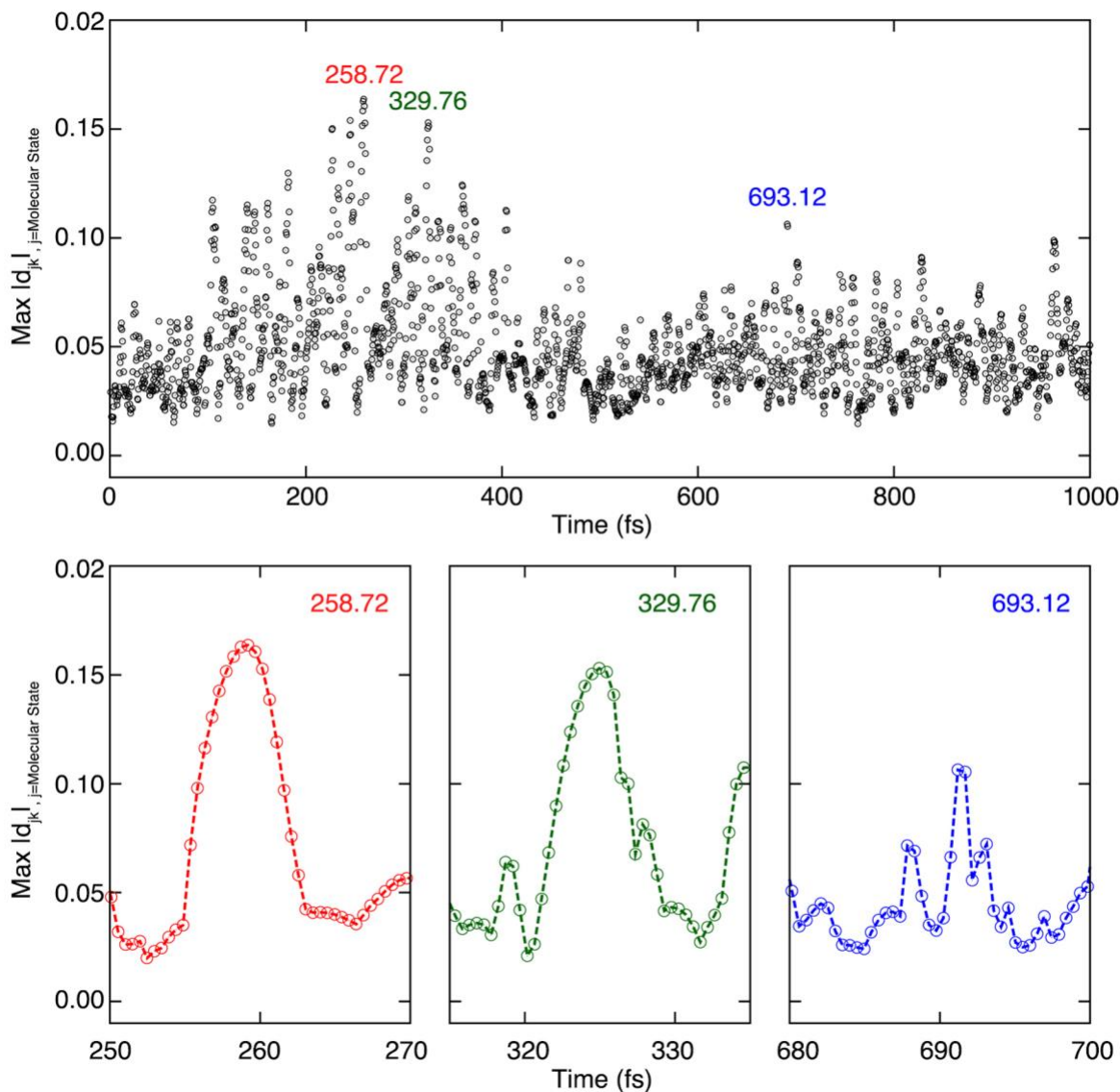
Figure 3.1 | Maximum nonadiabatic couplings (NACs) of the cyanidin LUMO at H-Si(111):cyanidin interface during the FPMD simulations. Sharp peaks in the NACs are well captured with sufficient resolution with the time step of 0.48 fs used in the simulations.

equilibrium positions for the monodentate structure; the atomic positions of 25O and 26O (link atoms between the Si(111) surface and the molecule), 31H and 32H (which replace the surface silicon atoms that connect to 25O and 26O) were held fixed at the equilibrium positions for the bidentate case. The results are given in **Table 3.1** and **Table 3.2** for monodentate and bidentate, respectively. As can be seen in **Table 3.1** and **Table 3.2**, the standard deviations of atomic positions

in FPMD simulations are much larger than the atomic position displacements that are caused by having an extra electron in the molecule. For the monodentate structure (**Table 3.1**), the averaged standard deviation of all the molecular atoms is 1.202 Å while the average atomic displacements caused by receiving the extra electron is only 0.032 Å. For the bidentate structure (**Table 3.2**), the averaged standard deviation of all the molecular atoms is 0.562 Å while the average atomic displacements caused by receiving the extra electron is only 0.047 Å. Thus, CPA used in our work does not influence the simulation results significantly.

3.2.3 Time step in FPMD simulation and nonadiabatic coupling calculations

Convergence of nonadiabatic coupling (NAC) calculation with respect to the time step in the FPMD simulation is important. Using the time step of 0.48 fs in the simulation, sharp peaks in the NACs are well captured with a sufficient resolution necessary for the FSSH simulations. The maximum NAC of the cyanidin LUMO state (which shows a significant fluctuation in energy in the simulation) is shown in **Figure 3.1**.

3.2.4 On time dependence of many-body corrections

Because of the very high computational cost associated, the many-body corrections (MBCs) were calculated for all electronic state only once at the equilibrium structure. The same (time-independent) MBCs were used to correct individual time-dependent KS energies from the FPMD simulation as discussed in CHAPTER 2. In order to verify the validity of this approximation, MBCs were calculated for a structure from FPMD simulations of H-Si(111):phenyl and compared those for the equilibrium structure. The equality comparison of the MBCs for the equilibrium structure
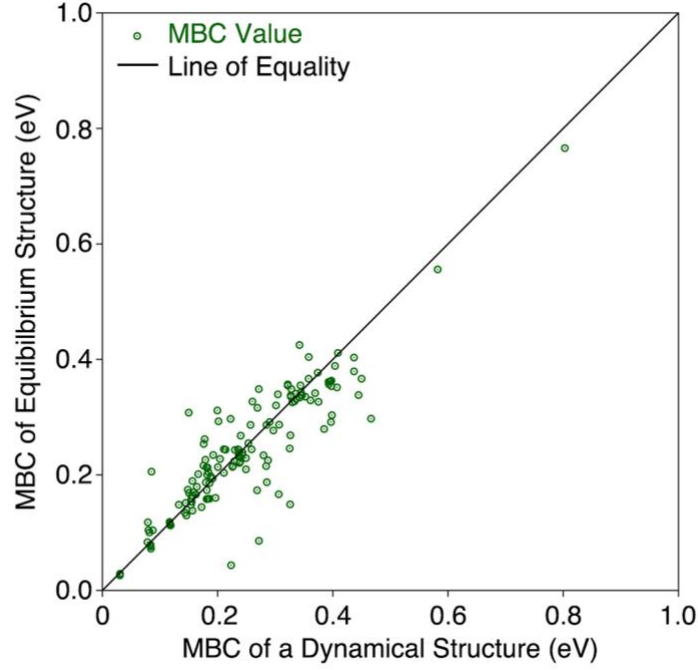
Figure 3.2 | Many-body corrections (MBCs) for the equilibrium structure and a dynamical structure from the FPMD simulation (at t=500.16 fs). The diagonal line represents the equality of MBCs for the two structures.

and a dynamical structure from the FPMD simulation (at 500 fs) is shown in **Figure 3.2**, where the data points locate close to the line of equality.

3.2.5 Convergence tests of the G_0W_0 calculation

Convergence tests of G_0W_0 calculations for H-Si(111):phenyl interface (benzene molecule attached to the surface) are shown in **Figure 3.3**. The convergence of VBM-CBM energy gap, as a representative energy difference, is shown with respect to several important parameters. The G_0W_0 calculations were performed using Yambo code.[115] The notations of all the key parameters are given as follows, and more details can be found in Ref 115: The energies are converged to within approximately ~0.025 eV.

1. Bnd is the number of states used in calculating the polarization function.
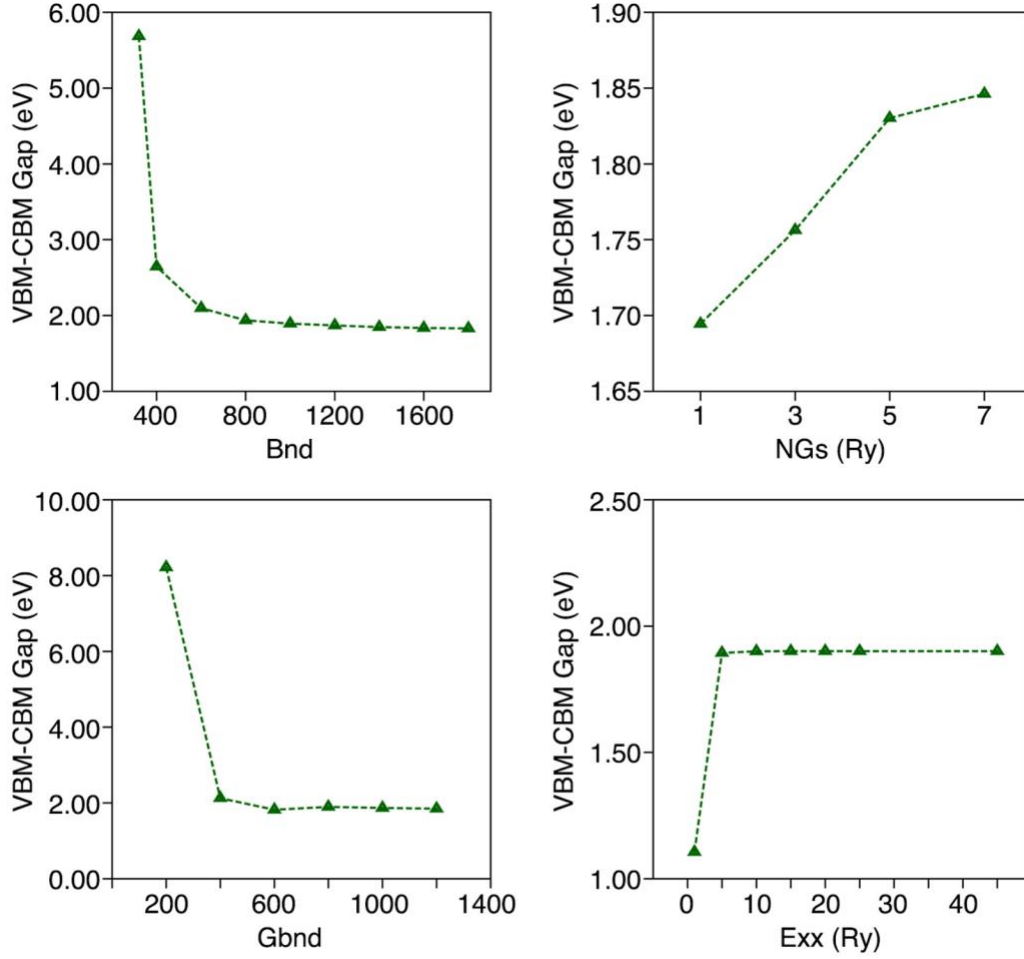
Figure 3.3 | Convergence tests on different parameters for G_0W_0 calculations. The convergence of VBM-CBM energy gap, as a representative energy difference, is shown with respect to the parameters.

2. NGs is the kinetic energy cutoff associated with the size of the integration of the polarizability function.

3. Gbnd is the number of states used in the calculation of the correlation part of the self-energy.

4. Exx is the number of plane-waves used in the calculation of the exchange self-energy.

Since these parameters are not independent, we applied the following procedures in practice:

1. Determine the converged Bnd value with large NGs (5 Ry), large Gbnd (1000), and large Exx (5 Ry);

50
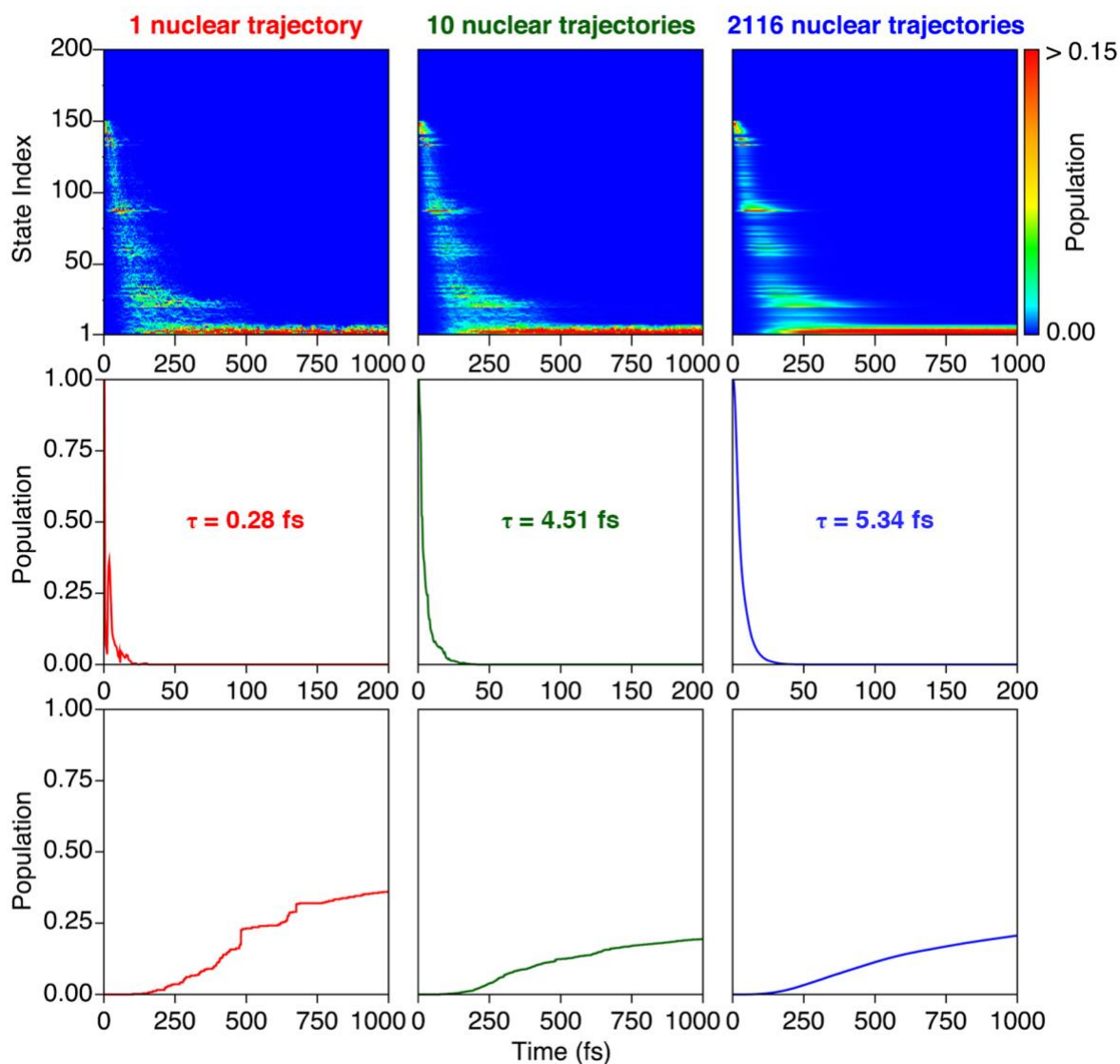
Figure 3.4 | Top row: Dependence of the population change for the excited electron on the number of 1 ps nuclear trajectories in the ensemble. Middle and bottom row: Population change for the initially fully-occupied state and for the cyanidin LUMO. The result with 2116 nuclear trajectories is fully converged.

2. Determine the converged NGs value with the converged value of Bnd (1200), large Gnd (1000), and large Exx (5 Ry);

3. Determine the converged Gbnd value with the converged values of Bnd (1200) and NGs (5 Ry), and large Exx (5 Ry);
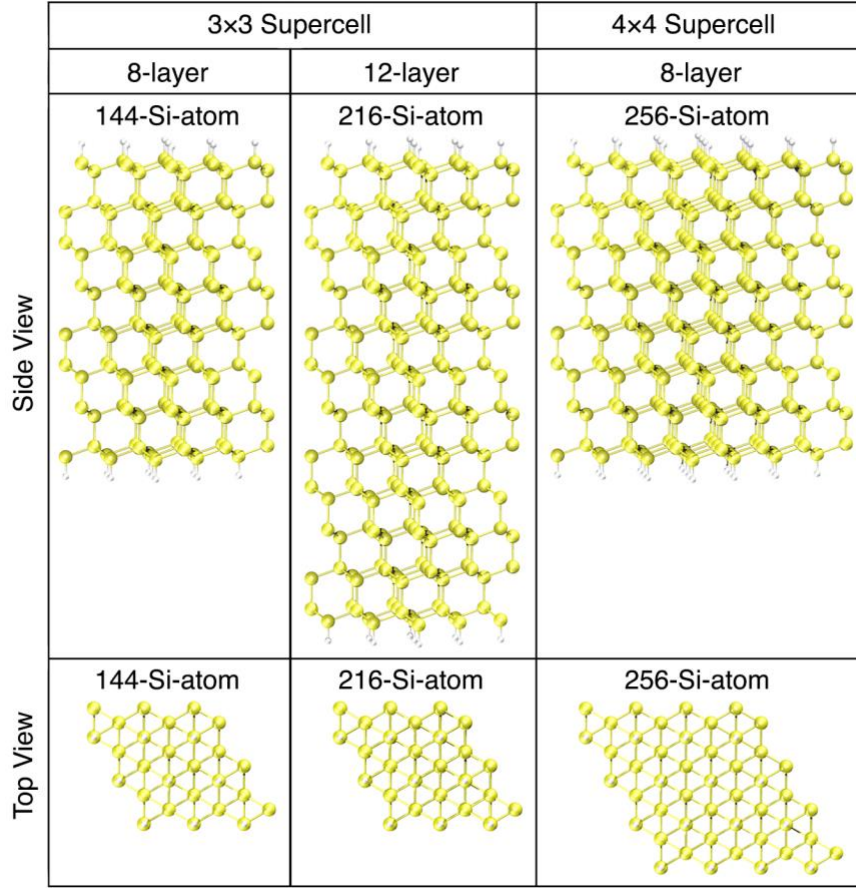
Figure 3.5 | Side and top views of the surface slab models with 144-Si-atom, 216-Si-atom, and 256-Si-atom (supercell). The bottom three layers were held fixed in bulk positions.

4. Determine the converged value for Exx with the converged values of Bnd (1200), NGs (5 Ry), and Gbnd (1200).

The final converged values for the key parameters are: 1200 for Bnd, 5 Ry for NGs, 1200 for Gbnd, and 25 Ry for Exx.

3.2.6 Convergence of hot electron dynamics with respect to nuclear trajectory ensemble

Dependence of the hot electron dynamics on the number of 1-picosecond nuclear trajectories in the ensemble is shown in the top row of **Figure 3.4**. The plots in the middle and bottom rows show the population change for the initially populated state (in the silicon state of 3.6 eV above

52
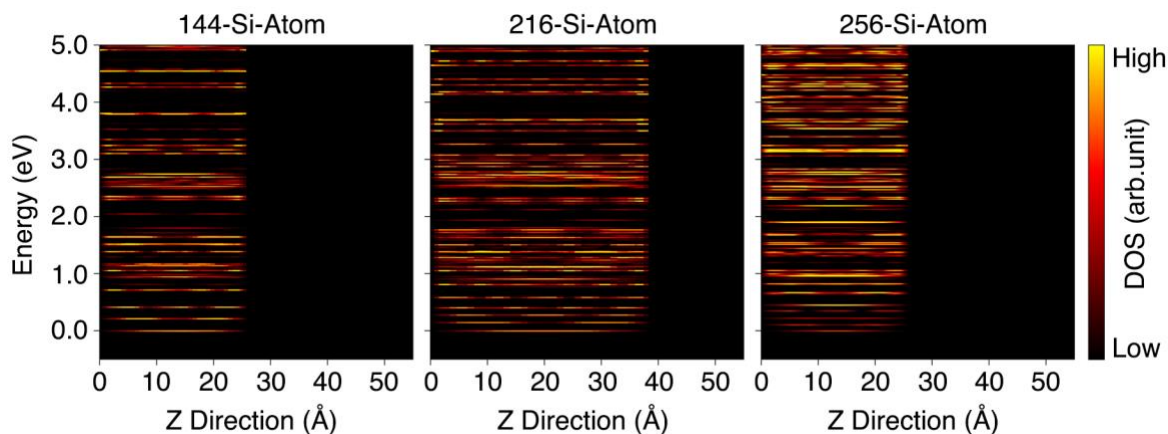
Figure 3.6 | Spatial-resolved DOS for the conduction band states of the surface slab models with 144-Si-atom (on the left), 216-Si-atom (in the middle), and 256-Si-atom (on the right). The spatial-resolved DOS is calculated by averaging electron density in the surface plane, and the silicon surface CBM is set to 0 eV as the reference energy.

surface CBM) and the cyanidin LUMO. The time constant (given in the middle row) was obtained by fitting to a single exponential function. The result with 2116 nuclear trajectories is well converged with respect to the number of nuclear trajectories in the ensemble.

3.2.7 Interface models

The H-Si(111) surface was modeled using a 3×3 supercell with eight layers of 144-Si-atom surface slab in this work as shown in the left side of **Figure 3.5**. The bottom three layers were held fixed in the bulk positions. The slab was separated from its periodic image along the surface normal by a vacuum region of 15 Å such that the interaction between the repeating slabs is negligible. Two other H-Si(111) surface slab models were used to examine the finite size error of the model: a 4×4 supercell with eight layers (256-Si-atom), and a 3×3 supercell with twelve layers (256-Si-atom) as shown in **Figure 3.5**. The spatial-resolved density of states based on KS single-particle energies are shown in **Figure 3.6** for the three surface slab models. The hot electron dynamics based on KS single-particle energies for the 144-Si-atom, 216-Si-atom, and 256-Si-atom H-Si(111)
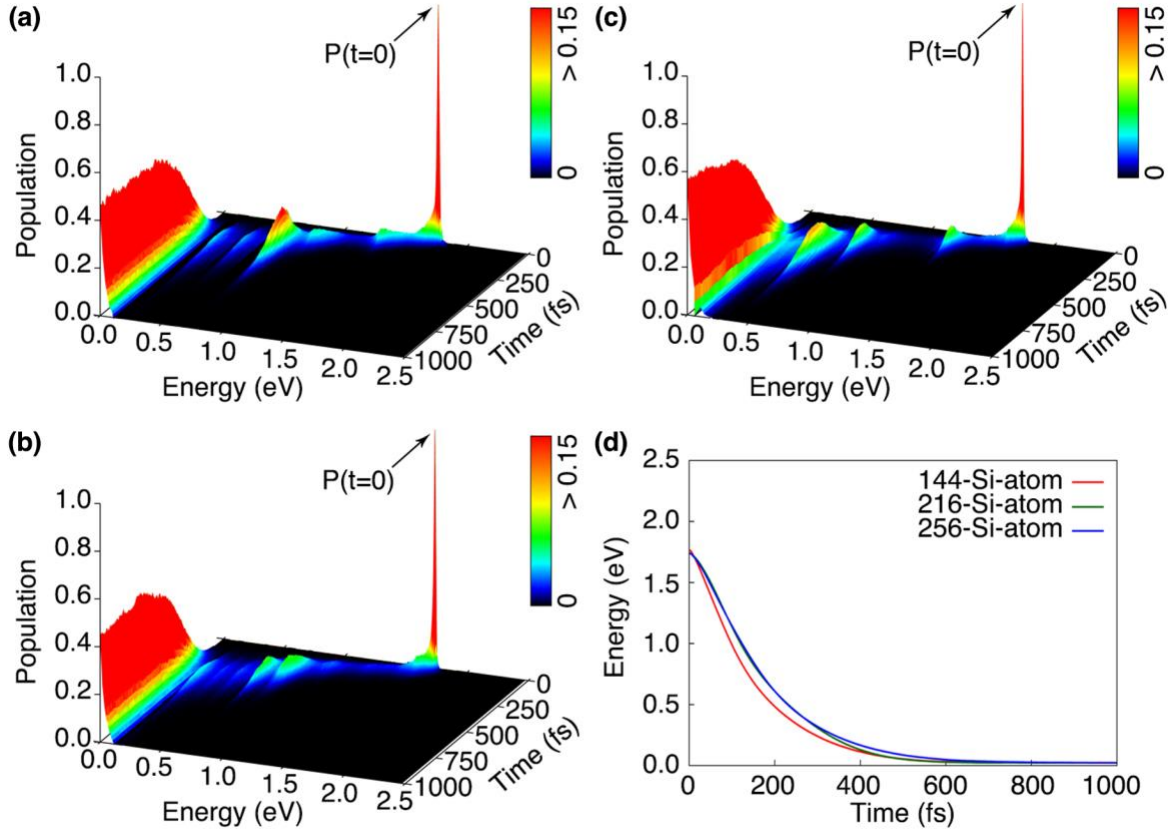
Figure 3.7 | Population change for the excited electron using (a) 144-Si-atom, (b) 216-Si-atom, and (c) 256-Si-atom H-Si(111) surface slab models. (d) Time evolution of the averaged energy of the excited electron for the 144-Si-atom (red), 216-Si-atom (green), and 256-Si-atom (blue) H-Si(111) surface slab models.

surface models are shown in **Figure 3.7a-c**, respectively. In addition, the time evolutions of the averaged energy of the excited electron for the 144-Si-atom, 216-Si-atom, and the 256-Si-atom H-Si(111) surface models are shown in **Figure 3.7d**. The averaged energy $\bar{\varepsilon}(t)$ is calculated as

$$\bar{\varepsilon}(t) = \sum_k \varepsilon_k(t) p_k(t) \tag{3.3}$$

where $\varepsilon_k(t)$ is the energy of the electronic state k, and $p_k(t)$ is the electron population in the state k.

For the clean H-Si(111) surface, all the three slab models exhibit similar relaxation features, and they give very similar decay constants for the average energy of the excited electron: 147.41

fs, 165.86 fs and 173.18 fs for the 144-Si-atom, 216-Si-atom, and 256-Si-atom surface slabs, respectively. For the 144-Si-atom model, the relaxation time using the QP energies is determined as 226.46 fs. Experimental relaxation time for the excited electron in bulk silicon and silicon surface has been reported to be approximately few hundred femtoseconds, depending on various details such as the carrier density, excitation energy, and also a specific experimental signal to which exponential decay fit was made.[58-59,118-121] Although precise details of the hot electron relaxation process are somewhat affected for regimes with low population (< 0.15) by the finite-size error when using the 144-Si-atom slab model, interfacial electron transfer (which is found to be largely decoupled from the hot electron relaxation process as will discussed in the SECTION 3.2) is likely unaffected.

A representative semiconductor-molecule interface between a hydrogen-terminated Si(111) surface[122] and a natural dye molecule cyanidin is considered in this work because the H-Si(111) semiconductor surface can be controllably synthesized with minimal defects.[122] We considered a low surface coverage of approximately 11% in terms of the Si-H units (see **Figure 3.8**). To study the adsorption dependence, monodentate and bidentate adsorption modes were considered as shown in **Figure 3.8a, b**. We employed a quantum dynamics simulation approach based on accurate electronic energy levels at the heterogeneous interface,[88] by synergistically combining fewest switches surface hopping algorithm,[46,76] G_0W_0 many-body perturbation theory calculation,[106-108] and first-principles molecular dynamics[123] (details see CHAPTER 2).

3.3 Results and Discussion

Figure 3.8c, d shows the spatial-resolved density of states (DOS) for conduction band states in the surface normal direction (Z axis). The surface's CBM is set to 0 eV as the reference energy,
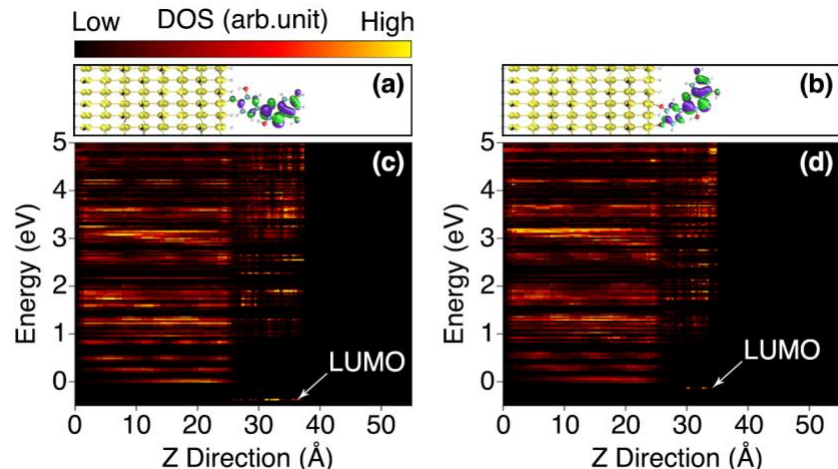
Figure 3.8 | Interface structures of the H-Si(111):cyanidin interface in (a) monodentate and (b) bidentate adsorption modes, isosurface of the single-particle Kohn-Sham electronic wave function for the molecule's LUMO is also shown at top. The spatial-resolved density of states (DOS) for the conduction band states of the (c) monodentate and (d) bidentate adsorption modes. The spatial-resolved DOS is calculated by averaging electron density in the surface plane, and the silicon surface CBM is set to 0 eV as the reference energy.

and the LUMO refers to the lowest unoccupied electronic state with its spatial character only within the adsorbed cyanidin, which is assumed to be in the oxidized state. The oxidized state here represents the situation after an excited electron is injected from the adsorbed molecule. The LUMO state is located energetically lower than the CBM by 0.37 eV and 0.13 eV for the monodentate and bidentate adsorptions, respectively. We initiate the first-principles simulation by placing the excited electron in a high-lying silicon state (~3.6 eV above the CBM). The excited electron population change for an ensemble of atomic trajectories at room temperature is shown in **Figure 3.9** as a function of time and average energy of electronic states for the H-Si(111):cyanidin interfaces. As can be seen in **Figure 3.9**, a non-negligible magnitude of hot electron transfer into a molecular state was observed. The accepting molecular states are quite high in energy at 2.3 eV and 2.4 eV above the CBM for mondentate and bidentate adsorptions, respectively. The states are indexed as 87 (mondentate) and 88 (bidentate) in **Figure 3.9**. We note here that, except for the
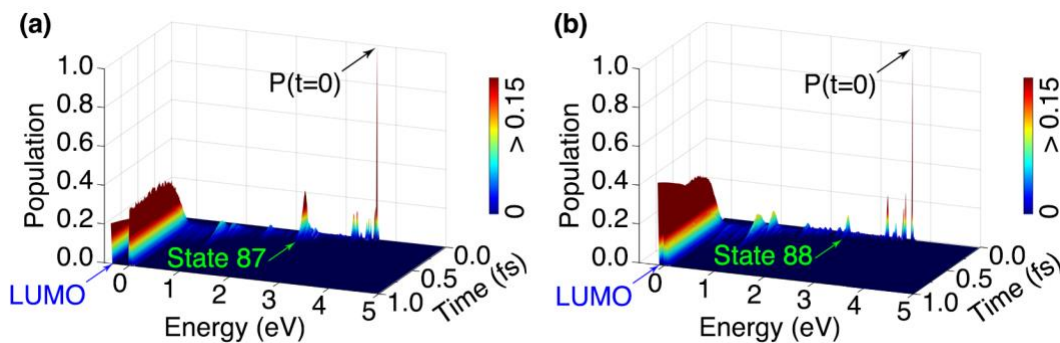
Figure 3.9 | Population change for the excited electron in (a) monodentate and (b) bidentate H-Si(111):cyanidin interface. Cyanidin's LUMO is located energetically below the surface CBM (E=0 eV) for both adsorption modes.
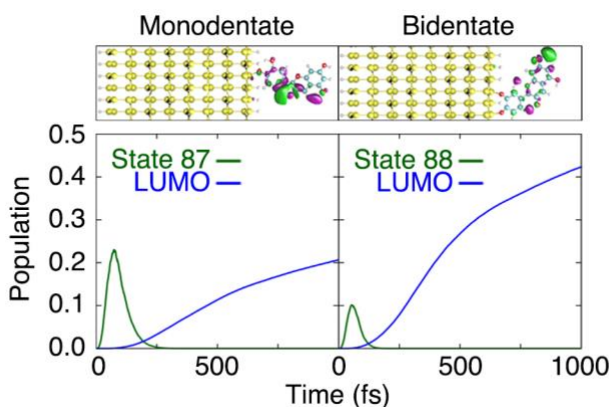
Figure 3.10 | Top: isosurface of the single-particle Kohn-Sham electronic wave function for the molecular state 87 (monodentate) and 88 (bidentate). Bottom: population change in the molecular state 87 (monodentate), state 88 (bidentate), and cyanidin LUMO.

LUMO, the state 87/88 is the only electronic state that is solely localized on the adsorbed cyanidin molecule. The transfer rate into these molecular states is quite fast even though they are spatially well localized within the molecule as shown in **Figure 3.10**. For these two molecular states, nonadiabatic couplings (NACs, which are often referred to also as vibronic couplings in literature) indicate significant coupling to some semiconductor states as shown in **Figure 3.11**. Despite the very fast transfer rate into the molecule, the resident time of the hot electron within the molecule is quite short, and fitting the population of the electronic states 87 and 88 to Gaussian curves gives full widths at half maximum of 80.64 fs and 58.08 fs for the monodentate and bidentate adsorptions,
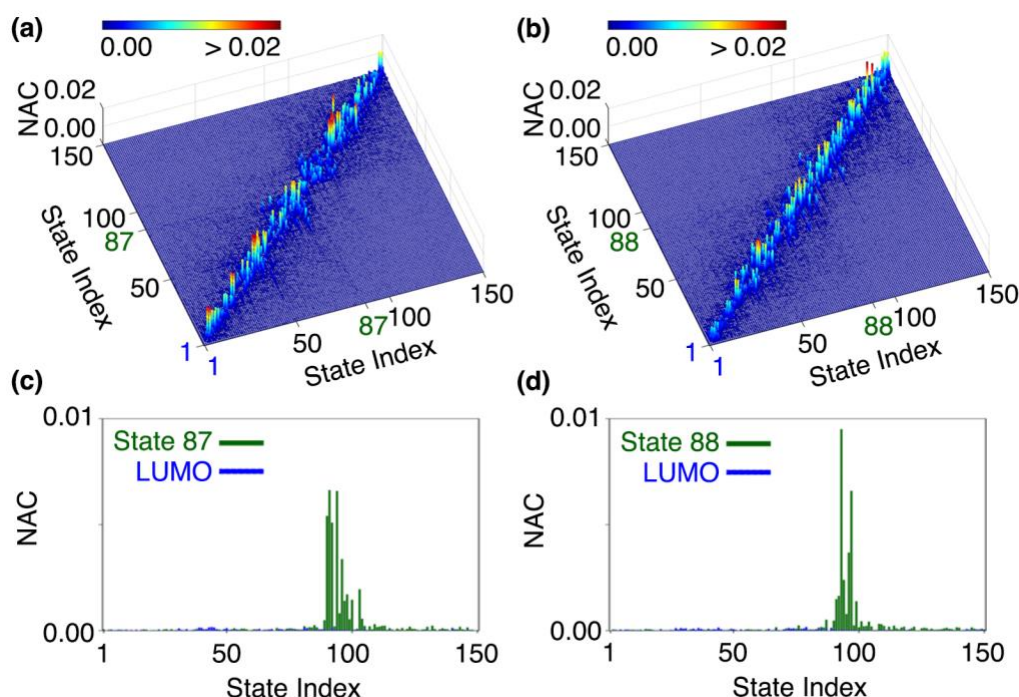
Figure 3.11 | Time-averaged nonadiabatic couplings (NACs) matrix of the unoccupied states (in atomic units) for (a) monodentate and (b) bidentate adsorption modes. The NACs for the cyanidin LUMO and molecular state 87/88 are shown for comparison in (c) monodentate and (d) bidentate. The state index of the cyanidin LUMO is set to 1 as the reference. NACs are particularly large close to the diagonal line.

respectively (see **Figure 3.10**). The hot electron transfers back to the semiconductor without remaining in the molecule for an extended time. Consequently, the hot electron relaxation takes place almost entirely within the semiconductor. Appreciable transfer of the excited electron from the silicon surface to the chemisorbed cyanidin occurs only after the electron has relaxed near the bottom of the conduction band.

As can be seen in **Figure 3.11**, the molecular LUMO does not show strong NACs to semiconductor states, and the electron transfer to the LUMO is rather gradual when compared to the hot electron transfer to states 87/88 as discussed above (see **Figure 3.10**). Beyond ~0.8 ps, the entire population can be accounted for in the semiconductor states within 10 k_BT (~0.25 eV) above the CBM and the molecular LUMO as shown in the left panel of **Figure 3.12**. This allows us to
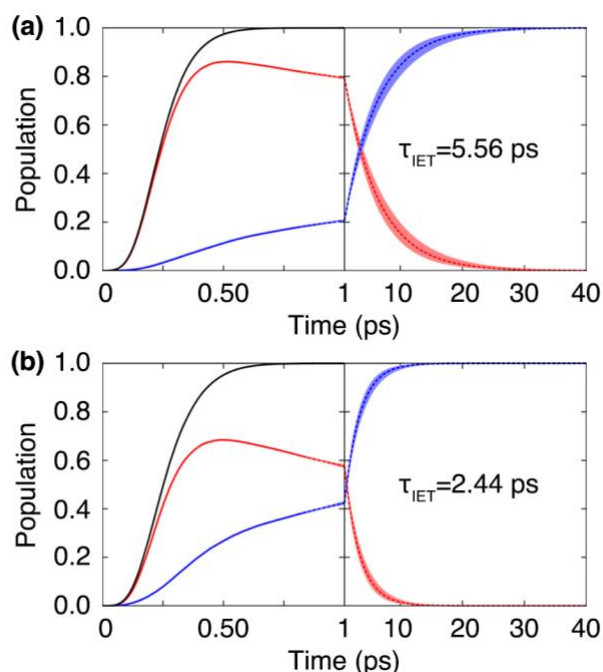
Figure 3.12 | Population change in the cyanidin LUMO (blue), silicon states within 10 k_BT above the surface CBM (red), and their sub-total (black) in the (a) monodentate and (b) bidentate adsorption modes.

employ an effective two-state kinetic model between the semiconductor and the chemisorbed molecule to efficiently describe the dynamics at longer time scales. This is convenient especially since first-principles simulation of the electron dynamics is computationally very demanding and currently not practical for more than several picoseconds. The right panel of **Figure 3.12** shows the population change according to the two-state kinetic model for time beyond 1 ps. The shaded regions indicate an uncertainty that stems from fitting the model to the first-principles simulation data for obtaining the rate constant. The time constants for the interfacial electron transfer were found to be 5.56 ps and 2.44 ps for the monodentate and bidentate adsorptions, respectively. For the electron population in the cyanidin LUMO to reach the equilibrium Boltzmann distribution for the monodentate and bidentate cases, it takes approximately 37.7 ps and 16.7 ps, respectively.

Our simulation predicts a typical intra-band relaxation time of several hundred femtoseconds, and the interfacial electron transfer to the adsorbed molecule's LUMO is largely decoupled from the relaxation process. A similar finding was also reported by Okano et al. for "ideal" CdS/CdTe Type-II heterojunction interfaces that are formed within individual nano-materials.[110] In their study, the interfacial electron transfer was observed to take place subsequently after the hot carrier relaxation of several hundred femtoseconds, and the interfacial electron transfer itself was characterized with a time scale of 450 fs. In the present work on the H-Si(111):cyanidin semiconductor-molecule interface, the interfacial electron transfer rate is found to be a few picoseconds. This transfer rate is approximately an order of magnitude slower than the rates observed experimentally at PbS QD-methylene blue (~370 fs) and CdSe QD-methylviologen (~60 fs) interfaces by Lian and co-workers.[65,109] At the same time, the picoseconds transfer rate in the present work is much faster than the nano- to microseconds time scales that are typically reported experimentally for oxide-molecule interfaces.[62-63,66] Such an enormous difference is indicative of additional processes in those experiments at oxide-molecule interfaces that are outside of the two-state model description. Given the defective nature of typical oxide materials, defect-induced electronic states might trap the excited electron rapidly below the conduction band. We indeed observe that trapping of the excited electron by a defect state can be very fast when we include a missing hydrogen dangling-bond defect at the H-Si(111) surface in our simulation. Our simulation shows that this process takes place on the time scale of a few picoseconds.

A possibility of the excited electron been trapped by surface defects was investigated by performing the simulations of the H-Si(111) surface slab with a missing-hydrogen dangling-bond at the surface, where the hot excited electron initially occupies the same high-lying silicon states (~ 3.6 eV above the surface CBM). The induced defect state energy level was found to be located
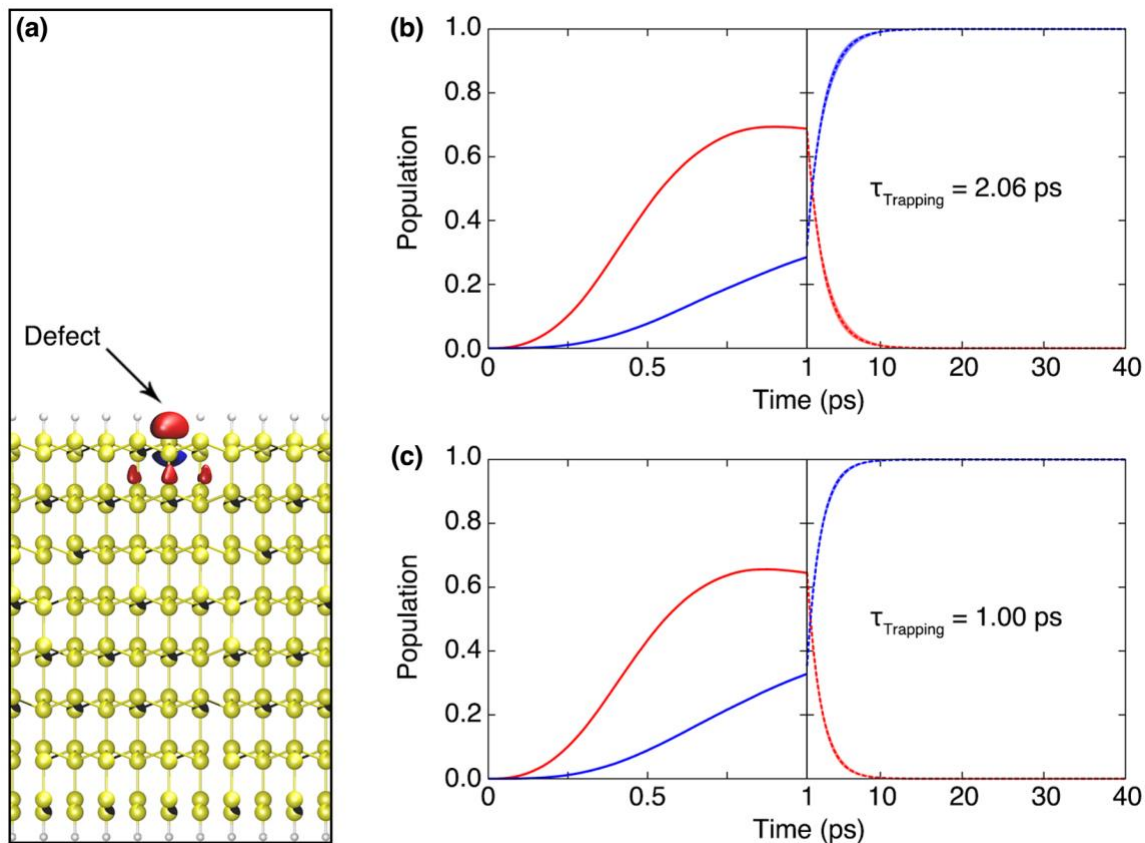
Figure 3.13 | (a) Isosurface of the defect electronic state that is induced by having a missing hydrogen atom at the surface. Population evolution of the electronic states within 10 k_BT above the surface CBM (red) and of the defect electronic state (blue) (b) when the defect state is located 1.10 eV below the surface CBM and (c) when the defect state is shifted to 0.60 eV below the surface CBM.

at 1.10 eV below the silicon surface CBM. Isosurface of the single-particle KS electronic wave function for this localized defect state is shown in **Figure 3.13a**. Employing the same two-state model between the silicon states within 10 k_BT above the surface CBM (in red) and the defect state (in blue), **Figure 3.13b** shows the population changes over time. The rate constant for the hot electron trapping was determined to be 2.06 ps. We also assessed the sensitivity of this trapping rate with respect to the energy difference by manually shifting the defect state energy to be at -0.60 eV with respect to the surface CBM. This yielded a similar trapping rate of 1.00 ps as shown in **Figure 3.13c**.

3.4 Summary

In conclusion, our work shows that, the interfacial electron transfer from semiconductor to the adsorbed molecule is largely decoupled from the fast hot electron relaxation process at a representative semiconductor-molecule Type-II interface between H-Si(111) surface and cyanidin molecule. Similar to QD-molecule interfaces,[65,109] we found that the interfacial electron transfer is quite fast with a time constant of a few picoseconds. However, the corresponding time scale is much shorter than the typical time scales reported for back electron transfer (BET) between a semiconductor and a molecule in the case of oxide materials.[62-63,66] These findings point to the importance of excited electron trapping by defect-induced states below the conduction band for understanding the overall BET mechanism for oxide materials. Our future work will focus on how different types of defects play an important role in oxide materials. How electron transfer among adsorbed molecules might influence the resident time of hot electron transfer in the molecule is another interesting question for a future study.

CHAPTER 4: DEPENDENCE OF HOT ELECTRON TRANSFER ON SURFACE COVERAGE AND ADSORBATE SPECIES AT SEMICONDUCTOR-MOLECULE HYBRID INTERFACES

Submitted by Li, L.; and Kanai, Y. to *Physic. Chem. Chem. Physic.*

4.1 Introduction

Novel concepts based on hot charge carriers have attracted great attention in recent years for various technological applications, ranging from photodetector,[67-70] photovoltaic (PV),[71-73] to photocatalysis.[74] In these applications, hot electron transfer (HET) at heterojunctions between different materials plays a central role in the performance of the devices. For instance, hot carriers are extracted through the selective energy contacts before thermalization in the hot carrier solar cell concept.[12,18] Particularly, HET from the semiconductor material to adsorbed molecule is of great concern in PV and photoelectrochemical (PEC) devices that are based on dye-sensitized solar cells (DSSCs),[3,40-41] since such an electron transfer process negatively impacts the device performance.[42-45]

Because understanding the HET process at a molecular level is central to realizing these novel applications, considerable efforts have been dedicated to investigating HET at various heterogeneous interfaces, such as quantum dot (QD) core-shell,[20] semiconductor-QDs,[21-23] semiconductor-metal,[24-28] and semiconductor-molecule.[29-30,75] Ultimately, one hopes to establish a "design principle" at the molecular level for controlling HET for various applications.

Despite great advances toward developing a molecular-level understanding in this field,[43,75,82-87] the interplay among various dynamical processes with distinct time scales that hot electron could potentially go through[42-43] complicates the development of a clear understanding of hot electron dynamics.[47-48] In our recent first-principles quantum dynamics simulation of excited electrons, the HET process from semiconductor to adsorbed molecule was observed.[30] This provided us with an atomistic model that we can use to study how the HET dynamics can be tuned at the atomistic level. In this work, we focus on the surface coverage of the adsorbed molecules and consider two widely-used dye molecules of Cyanidin and Alizarin.

In this chapter, we present a first-principles study on elucidating the impact of surface coverage and molecular species on the HET process at semiconductor-molecule heterojunctions. Our calculations were performed using a computational approach[30,124] that combines first-principles molecular dynamics (FPMD) simulation and the single-particle fewest-switches surface hopping (FSSH) algorithm.[44,46,61,76] The detailed procedure has been discussed in our earlier works.[30,124] In order to obtain a better description of the energy level alignments at the heterogeneous interface, many-body perturbation theory calculations at the "one-shot" G_0W_0 level[106-108] were used to correct the Kohn-Sham (KS) eigenvalues from DFT calculations.

4.2 Computational Details and Interface Models

4.2.1 Computational details

The FPMD simulations were performed for a duration of 2 ps with a time step of 0.48 fs at 295 K using a modified version of the Qbox code.[113] The KS wave functions were represented in a plane-wave basis using norm-conserving pseudopotentials[112] with energy cutoff of 50 Ry. The generalized gradient approximation parameterized by Perdew, Burke, and Ernzerhof (PBE)[111] was

used for the exchange-correlation functional. The KS single-particle energies and nonadiabatic couplings (NACs, which are also referred to as vibronic couplings in literature) were obtained from the FPMD simulation on-the-fly using the numerical prescription by Hammes-Schiffer and Tully.[76] NAC matrix is calculated as

$$
D_{ij} = \langle \Psi_i(R(t)) | \nabla_R | \Psi_j(R(t)) \rangle \cdot \frac{dR}{dt}
$$

$$
= \langle \Psi_i(R(t)) | \frac{\partial}{\partial t} | \Psi_j(R(t)) \rangle
$$

(4.1)

We implemented the numerical calculation of NACs using the time derivative by enforcing the phase continuity as in ref 92, and follow the prescription by Hammes-Schiffer and Tully for calculating the NACs numerically.[76]

Quasi-particle (QP) energies were calculated in the context of many-body perturbation theory, starting from the KS wave functions and energies. Many-body corrections were calculated within the so-called "one-shot" G_0W_0 approximation,[106-108] starting from the PBE-KS wave functions and eigenvalues with the random-phase approximation for the screened Coulomb interaction and the Godby-Needs plasmon-pole model[116-117] was used in calculating the dielectric function. The G_0W_0 calculations were performed at the equilibrium geometry using the Yambo code,[115] with the KS wave functions obtained from the Quantum Espresso code.[114] The convergence tests for the G_0W_0 calculations were carefully performed.[30] The excited electron dynamics was then modeled by performing the FSSH simulations,[44,46,61,76] using the QP energies from the G_0W_0 calculation and the NACs from the FPMD simulation. The FSSH simulations were performed within the classical-path approximation (CPA) as described in ref [30]. This allows us to use a large number of atomic trajectories for converging the ensemble-averaged quantities because the trajectories do not depend on the hops when the CPA is adapted. First, an ensemble of 2116 trajectories was generated by taking a 1 ps trajectory from various different temporal points in the FPMD simulation. Thus, each

of these 1 ps long trajectories starts with different positions and momenta for atoms. Then, 500 FSSH simulations were performed for each trajectory, converging the sampling of the hopping probability distribution using the Monte Carlo method.

It is useful to comment on this first-principles approach, contrasting it to the recent first-principles Boltzmann Transport Equation (BTE) approach which describes the flow of collective electrons and phonons in phase space.[125] These two approaches are designed to describe the carrier dynamics in different limits of charge carrier density, and therefore their appropriateness depends on the context in which these approaches are employed. The present approach based on FSSH method[43-44] simulates the time-dependent statistical description on a single excited electron for an ensemble of the system (i.e. many interfaces with a single excited electron), and it is suitable when coupling to the lattice movement (i.e. ions) is a dominate factor in controlling the relaxation of the excited electron. In such a simulation, the time-dependence of the probabilistic distribution can be modeled by performing ensemble of FSSH stochastic simulation runs, and the detailed balance condition is satisfied. At the same time, carrier-carrier scattering is not present in this approach unlike the BTE method. In the first-principles BTE approach, statistical behavior of a collection of carriers is modeled by propagating probability density function in time. Bernardi and co-workers made significant advances for the first-principles BTE approach in recent years.[125-126] They have demonstrated calculations of interaction between quasi-particles (electrons, phonons, etc) from first-principles calculations in the context of the many-body perturbation theory, and these properties are used to employ the semi-classical BTE for studying carrier dynamics in real materials. More rigorous approaches based on non-equilibrium Green's function such as Kadanoff-Baym equation are also emerging in the context of first-principles approach in recent years. A comprehensive review can be found in ref 127.
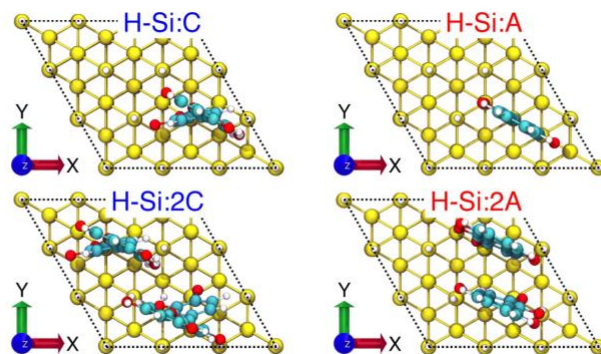
Figure 4.1 | Top view of the simulation cells for the H-Si:C, H-Si:2C, H-Si:A, and H-Si:2A interfaces. The H-Si(111) surface was modeled using a 144-Si-atom slab with eight layers.

4.2.2 Interface models

Representative semiconductor-molecule interfaces between a hydrogen-terminated Si(111) surface and two widely -used dye molecules, Cyanidin and Alizarin, were considered in this work to elucidate the impact of molecular adsorbate species on the HET process. Our earlier work showed noticeable HET with Cyanidin adsorbed at the H-Si(111) surface.[30] Alizarin was studied here because it is a dye molecule that is most widely studied both experimentally and theoretically in the literatures. [82,128-129] The molecule has its unoccupied electronic states energetically quite high, often well above the conduction band minimum (CBM) of many semiconductors.[82] To examine how surface coverage influences the HET process, surface coverages of ~11% (in terms of the number of Si-H units at the surface) and ~22% were studied, as shown in **Figure 4.1**. The molecules are adsorbed and oriented such that the π-π interaction is maximized. Short-hand notations are used for referring to the interface models as H-Si:C (11% coverage of Cyanidin), H-Si:2C (22% coverage of Cyanidin), H-Si:A (11% coverage of Alizarin), and H-Si:2A (22% coverage of Alizarin).

The H-Si(111) surface was modeled using a 3×3 supercell with eight layers of 144-Si-atom surface slab (with a surface area of ~0.45 nm^2 and thickness of ~2.4 nm) in this work. The bottom
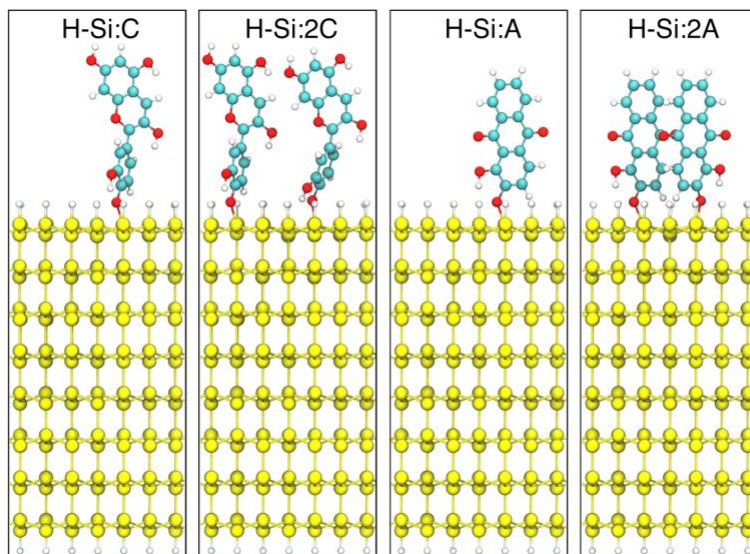
Figure 4.2 | Side view of the interface models investigated in this work.

three layers were held fixed in the bulk positions during the FPMD simulations. The slab was separated from its periodic images along the surface normal by a vacuum region of 15 Å such that the interaction between the repeating slabs is negligible. Side view of the four interface models investigated in this work is shown in **Figure 4.2**.

The spatial-resolved density of states (DOS) of the unoccupied electronic states for the interfaces of H-Si:C and H-Si:2C, H-Si:A, and H-Si:2A are shown in **Figure 4.3**, where the surface conduction band minimum (CBM) is set as the reference energy of 0. The spatial-resolved DOS is calculated by averaging the electron density in the surface plane. As can be seen in **Figure 4.3**, the unoccupied electronic states of the Alizarin molecule are energetically situated above the surface CBM, so that fast and efficient interfacial electron transfer could take place,[82] making it another ideal interface model to investigate HET process.
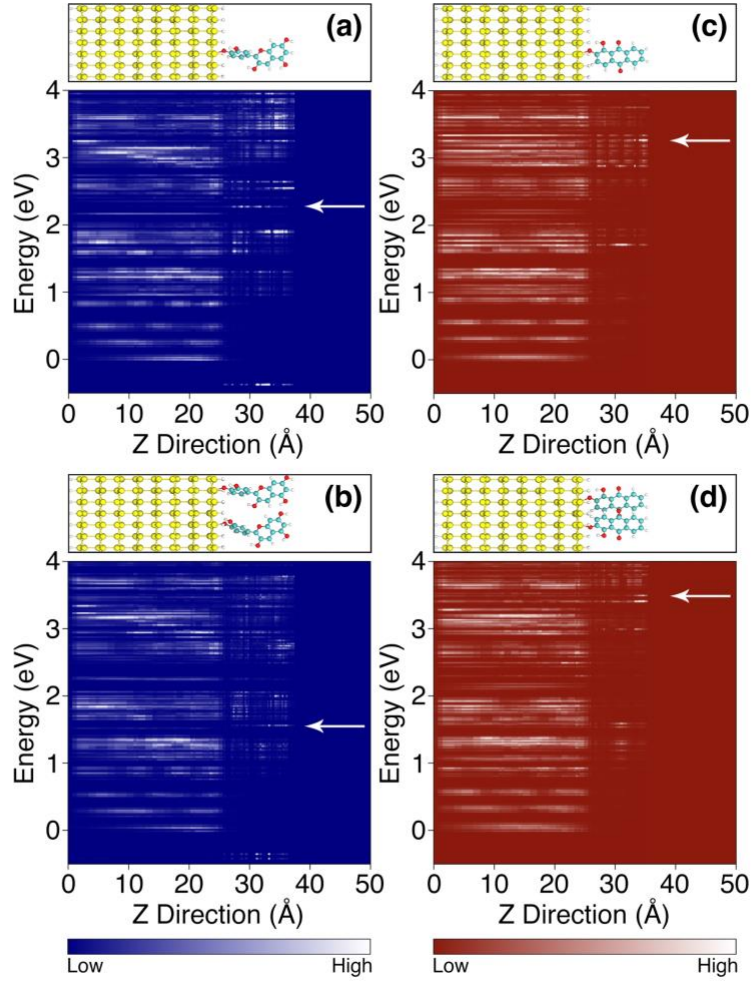
Figure 4.3 | Spatial-resolved density of states for (a) H-Si:C, (b) H-Si:2C, (c) H-Si:A, and (d) H-Si:2A interfaces, where the DOS is calculated by averaging the electron density in the surface plane. Hot electron states are indicated by arrows and the surface CBM is set as the reference energy of 0 eV in the spatial-resolved DOS figures.

4.3 Results and Discussion

Figure 4.4a-d shows the probability of locating the hot electron at a specific energy as a function of time for an ensemble of interfaces simulated at room temperature. The reference energy of 0 eV corresponds to the conduction band minimum (CBM) of the semiconductor surface. For simulating dynamics of the hot electron, a highly-excited electron was initially placed in a semiconductor state with the energy of ~3.6 eV above the surface CBM. As can be seen in **Figure 4.4a-d**, the excited
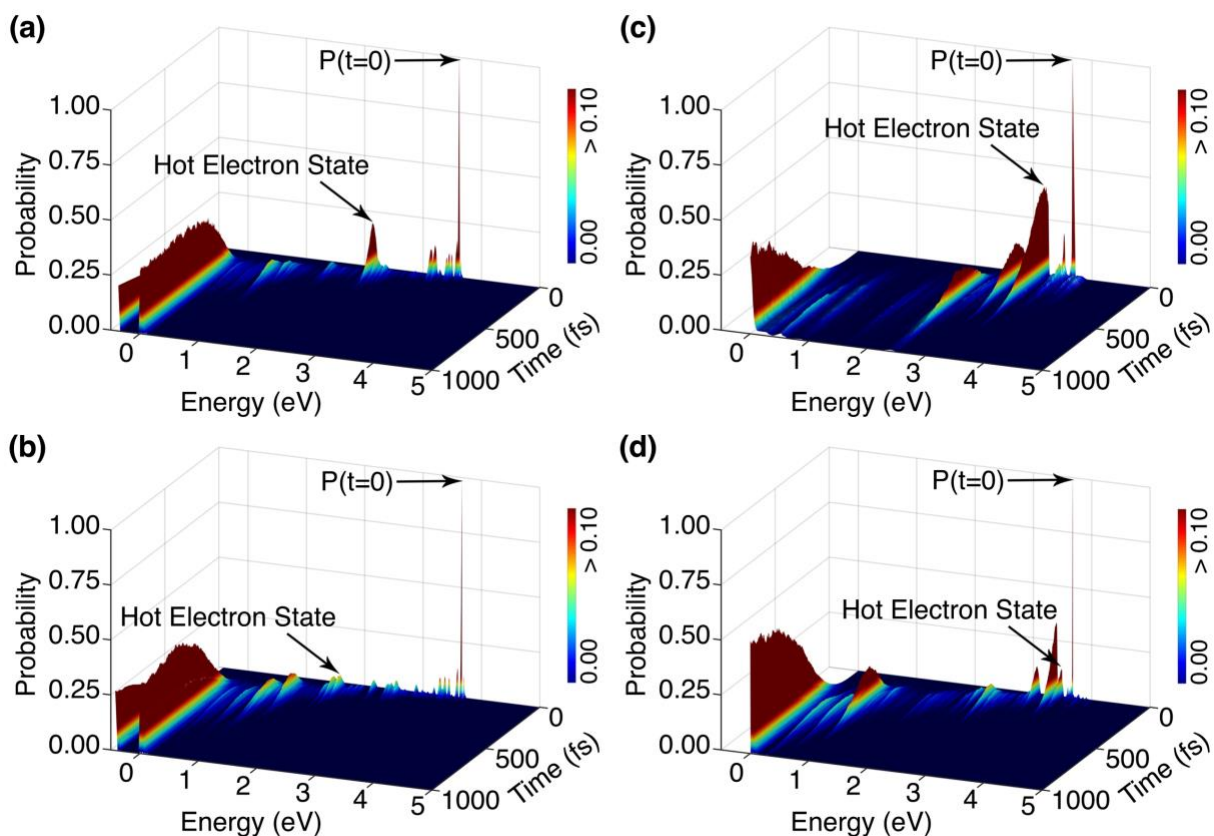
Figure 4.4 | Probability of locating the excited electron at a specific energy as a function of time at the interfaces of (a) H-Si:C, (b) H-Si:2C, (c) H-Si:A, and (d) H-Si:2A. The reference energy of 0 eV corresponds to the surface CBM. The hot electron accepting state that dominantly localized on the molecule is referred to as hot electron state. The excited electron was initially populated in a semiconductor state with energy of ~3.6 eV above the surface CBM as indicated by P(t=0).

electron dynamics does not exhibit probability change that follows a simple monotonic decay for any of these interfaces. In particular, the H-Si:A interface yields very slow relaxation due to significant trapping of the hot electron within the adsorbed molecule before it relaxes down to the surface CBM. This HET into a localized state of the adsorbed molecule was observed most prominently for the H-Si:A interface, but to a lesser extent for all other interfaces. These accepting molec ular states for the hot electron are referred to as hot electron states throughout this paper. The hot electron state is located energetically at 1.34, 2.09, 0.40, and 0.18 eV below the initial excited electronic state at the H-Si:C, H-Si:2C, H-Si:A, and H-Si:2A interfaces, respectively (see
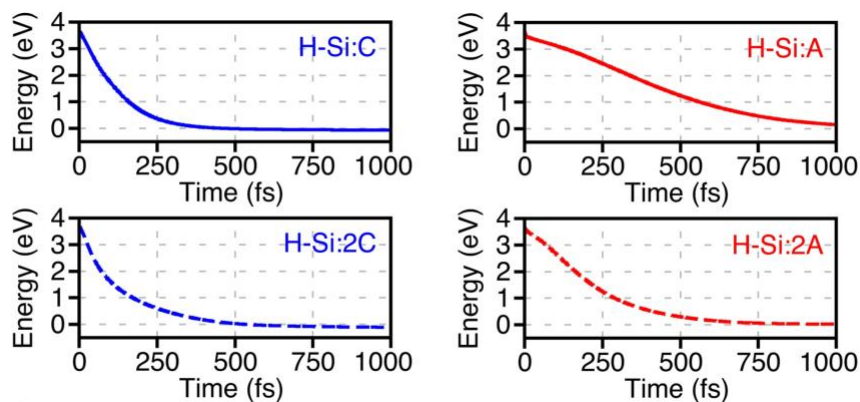
Figure 4.5 | Ensemble averaged energy for the excited electron at the interfaces.

Figure 4.4a-d). Time evolution of the ensemble-averaged energy for the hot electron is shown in **Figure 4.5**, and they do not follow an exponential decay as observed previously at the clean H-Si(111) surface[30] because of the HET to the adsorbed molecules.

Peak probability and lifetime of the hot electron within the adsorbed molecule are the two key quantities of interest for characterizing the HET because they indicate the extent to which the hot electron transfers into the adsorbate and the extended time that the hot electron resides within the molecule. Probability changes for the hot electron states are shown in **Figure 4.6a**. As can be seen, the peak probability in the hot electron state is much greater for the low-coverage than for the high-coverage (H-Si:C vs. H-Si:2C and H-Si:A vs. H-Si:2A), and it reaches as high as 0.42 for the H-Si:A interface (see **Table 4.1**). In addition to the peak probability, the residence time of hot electron

Table 4.1 | Peak probability and residence time of hot electron within the adsorbed molecule at the interfaces.

Interface	H-Si:C	H-Si:2C	H-Si:A	H-Si:2A
Peak Probability	0.23	0.04	0.42	0.13
Residence Time (fs)	81	106	192	53
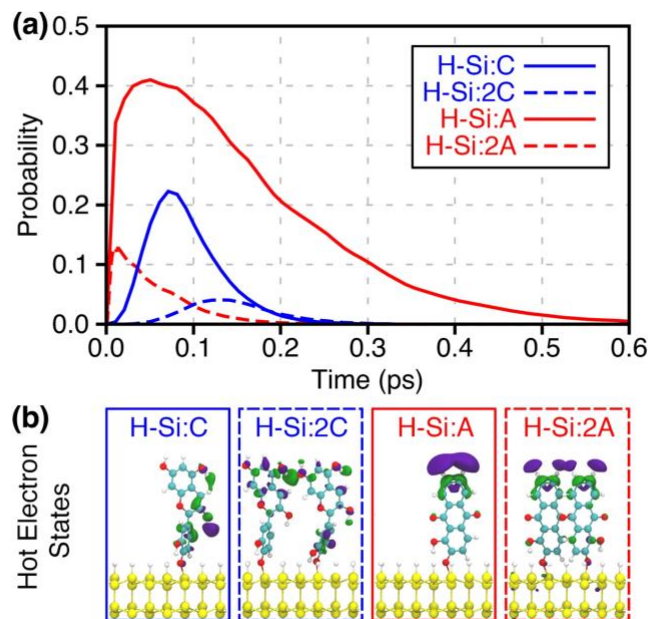
Figure 4.6 | (a) Probability change and (b) isosurface of the single-particle Kohn-Sham electronic wave function of the hot electron states at the interfaces. Hot electron states become delocalized over both molecules when the surface coverage is increased.

within the adsorbed molecule is another important factor for utilizing highly-excited electrons for some technological applications. We determined the hot electron lifetime by calculating the full width at half maximum of the probability rise, and the results are summarized in **Table 4.1**. Although the H-Si:2C interface exhibits a longer lifetime compared to the H-Si:C interface, the likelihood of finding the hot electron is very small. The hot electron lifetime within the adsorbed Alizarin molecule at the H-Si:A interface was found to be noticeably longer, comparable to the typical hot electron relaxation time for the clean H-Si(111) surface and bulk silicon.[30,58-59,118-121] At the same time, this is still much shorter than the typical time scales of redox reactions by adsorbed molecules at semiconductor-molecule interfaces, ranging from nanoseconds to microseconds.[130] We note also here that we do not observe excited electron relaxation within the molecule after the hot electron transfers into the molecule even though there exist energetically-lower electronic states localized
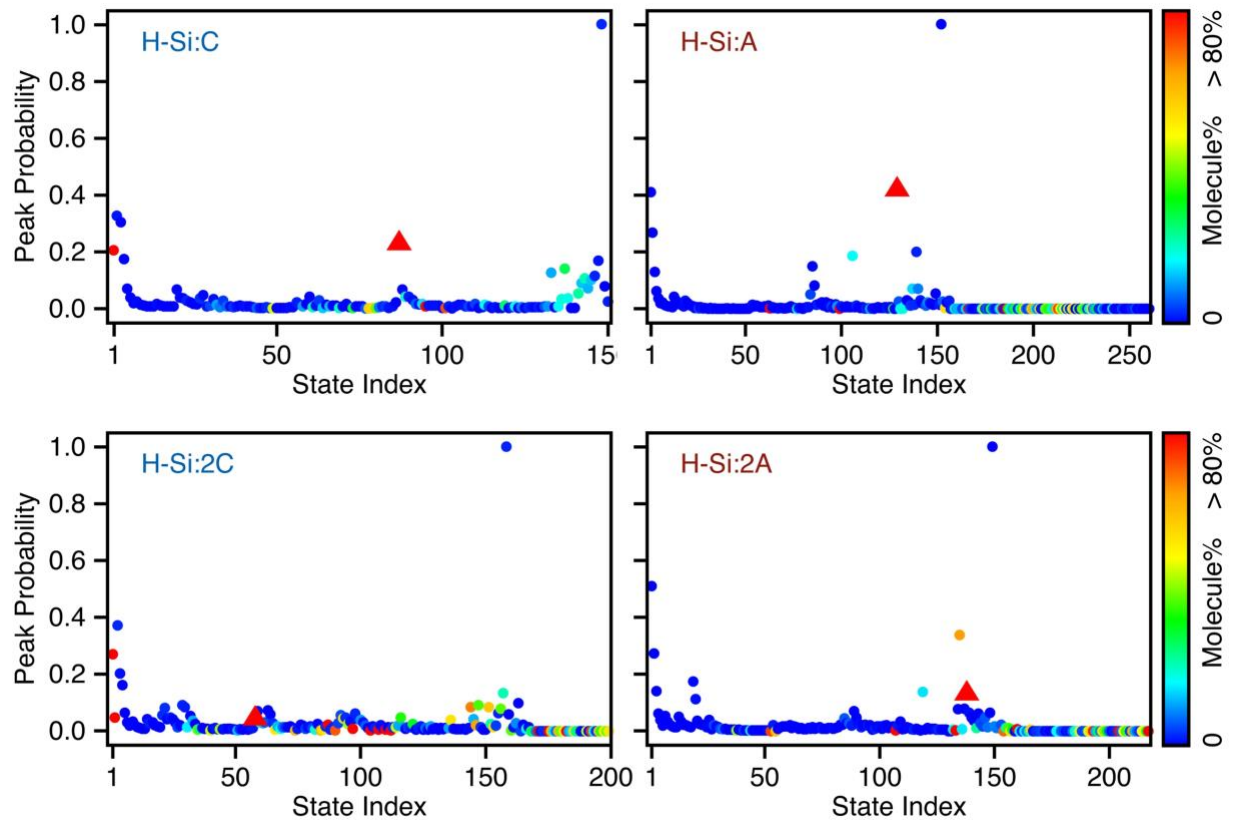
Figure 4.7 | Peak probability of the hot electron within the unoccupied electronic states as a function of state index based on time-averaged energy, together with the wave function contribution from the adsorbate for each unoccupied electronic state. Red triangle marker represents the pure molecular state with the largest hot electron probability and is referred to as hot electron state.

on the molecule. Rather, the excited electron transfers back to the semiconductor. Peak probability of the excited electron within the unoccupied electronic states as a function of state index based on time-averaged energy is shown in **Figure 4.7**, together with the wave function contribution from the adsorbate for each unoccupied electronic state. The red color indicates that the wave function is mainly localized on the surface adsorbate. Here, we consider an electronic state as a pure molecular state only if its wave function has more than 80% contribution from the adsorbed molecule. Among all the pure molecular states depicted by red color, the one with the largest hot electron probability is labeled by triangle marker, and is referred to as hot electron state throughout

73

this work. Although the high surface coverage interfaces (H-Si:2C and H-Si:2A) provide more molecular states localized on the adsorbed molecule (red dots in **Figure 4.7**) than the low coverage interfaces (H-Si:C and H-Si:A), the hot electron state becomes highly delocalized on both adsorbed molecules as can be seen in **Figure 4.6b**.

Comparing the two different surface coverages, one might have naively assumed that increasing surface coverage would enhance the HET process from semiconductor to the adsorbed molecule simply because the number of the hot electron states might increase as well. However, the results show otherwise (**Figure 4.6a**). As can be seen in **Figure 4.6b**, the hot electron states for the low-coverage cases are not the same as the hot electron states for the high-coverage cases. Our calculations show that the hot electron states do not remain localized on individual molecules when the surface coverage is increased, and the states become highly delocalized. In the case of Alizarin, the hot electron state becomes delocalized over both molecules when the surface coverage is increased (**Figure 4.6b**). However, for Cyanidin, the hot electron state does not simply become delocalized with the increased coverage, and other molecular states become more efficient in accepting the hot electron. In the case of Cyanidin, the delocalization is not simply due to the inter-molecular interaction but it also has to do with the interaction of the highly-polar molecules responding to the electrostatic field by the semiconductor surface. Without the surface, the hot electron states remain localized on individual molecule, but the surface causes the states to not only delocalize but to also change its spatial character.

Isosurface of the molecular states that correspond to the hot electron state of the H-Si:C interface for the two Cyanidin molecules are shown in **Figure 4.8**. The geometry of two Cyanidin molecules are directly taken from the H-Si:C interface as shown in **Figure 4.2**, and the bottom two oxygen atoms are terminated by hydrogen atoms (instead of the silicon surface). As can be seen in
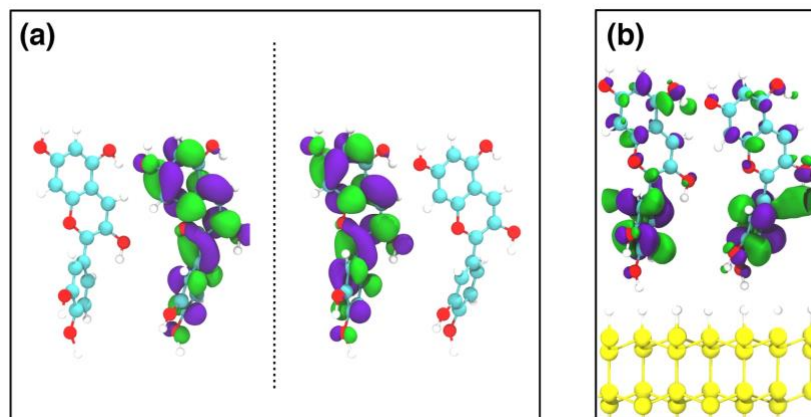
Figure 4.8 | Isosurface of the single-particle Kohn-Sham electronic wave function of the molecular states for (a) isolated two Cyanidin molecules, (b) the interface between Cyanidin molecules and the H-Si(111) surface with a separation distance of 1 angstrom. The geometry of the Cyanidin molecules was taken directly from the H-Si:C interface, where the bottom two oxygen atoms were terminated by hydrogen atoms.

Figure 4.8a, the molecular states for the two molecules without the surface are highly localized on individual molecules although there are no such corresponding states at the H-Si:2C interface. When the H-Si(111) surface was placed close to the two Cyanidin molecules with a separation distance of 1 angstrom as shown in **Figure 4.8b**, the molecular states become highly delocalized on both molecules as in the case of the H-Si:2C interface. The reason why the hot electron state does not remain localized on individual molecules is not simply because of the inter-molecular interaction but because of the presence of the semiconductor surface.

To understand this result from the first-principles dynamics simulations, we herein examine nonadiabatic couplings (NACs) since they have previously been found to play a key role in determining HET efficiency.[30,131] Time-averaged magnitudes of the nonadiabatic coupling between hot electron state and other semiconductor states are shown in **Figure 4.9**. **Figure 4.10** shows the density of NAC as a function of NAC magnitude between the hot electron state and higher-lying/lower-lying semiconductor states (i.e. semiconductor states energetically higher/lower than
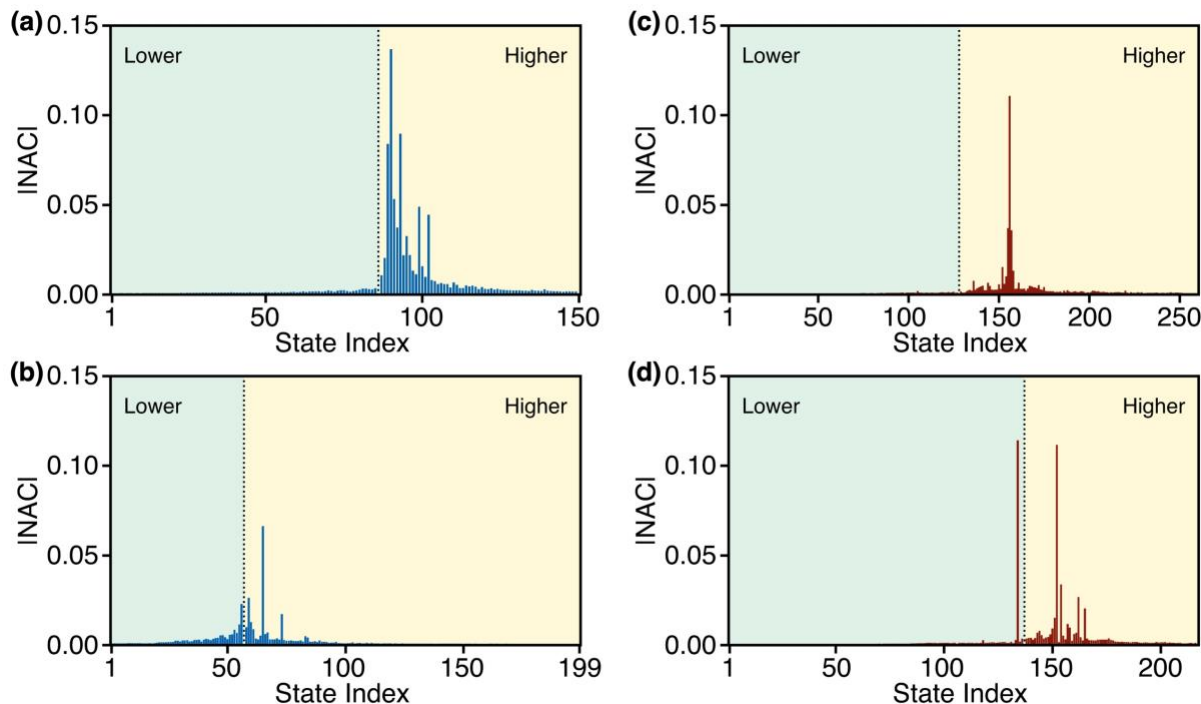
Figure 4.9 | NACs (in a.u.) between the hot electron state and the unoccupied semiconductor states at the four interfaces of (a) H-Si:C, (b) H-Si:2C, (c) H-Si:A, and (d) H-Si:2A. The positions of the hot electron states are labeled out in the matrix by dash lines.

the hot electron state). For the Cyanidin case (H-Si:C vs. H-Si:2C) as shown in **Figure 4.10a**, the low-coverage interface exhibits larger magnitudes for the NACs between the hot electron state and higher-lying semiconductor states than the high-coverage one. The hot electron is therefore much more likely to transfer into the molecule at the low-coverage interface. We also note that the NACs with lower-lying semiconductor states are significantly smaller for the low-coverage interfaces, making the hot electron state quite effective in retaining the excited electron within the adsorbed molecule for an extended time. For the Alizarin case (H-Si:A vs. H-Si:2A) as shown in **Figure 4.10b**, both the low and high-coverage interfaces exhibit similar NAC magnitudes between the hot electron state and higher-lying semiconductor states, including the presence of a well-defined peak in the NAC around ~0.11 a.u., this gives rise to the similar HET rate. This can be seen in **Figure**
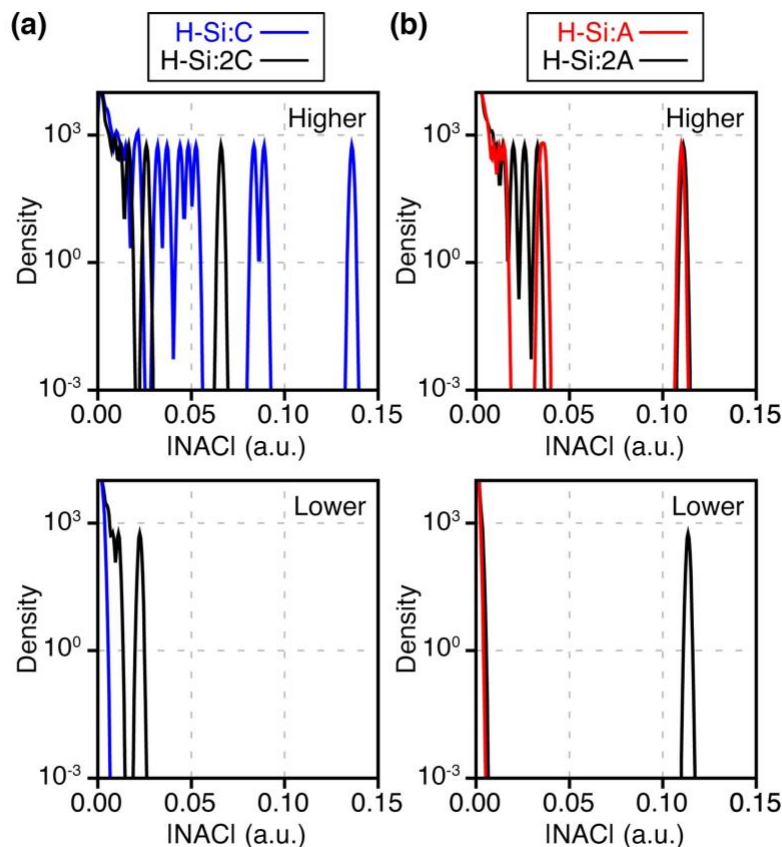
Figure 4.10 | Density of nonadiabatic coupling (NAC) as a function of NAC magnitude (in a.u.) between the hot electron state and higher-lying/lower-lying semiconductor states for the (a) Cyanidin and (b) Alizarin cases. Y-axis is shown in log scale. Bin size of 5×10^{-4} was used for the Gaussian broadening where $\sigma^2=5\times10^{-7}$.

4.6a. The rate of the initial increase in the probability for H-Si:A and H-Si:2A are the same (i.e. two red lines are on top of each other). At the same time, for the NACs between the hot electron state and lower-lying semiconductor states, only the high-coverage case of H-Si:2A but not the H-Si:A exhibits large NAC with ~0.11 a.u. (**Figure 4.10**). This leads to a rapid hot electron transfer from the adsorbed molecule back to the semiconductor at the H-Si:2A interface. Consequently, the hot electron residence time within the adsorbate is shorter for the H-Si:2A interface than the H-Si:A interface as summarized in **Table 4.1**. These characteristics in the NACs between the
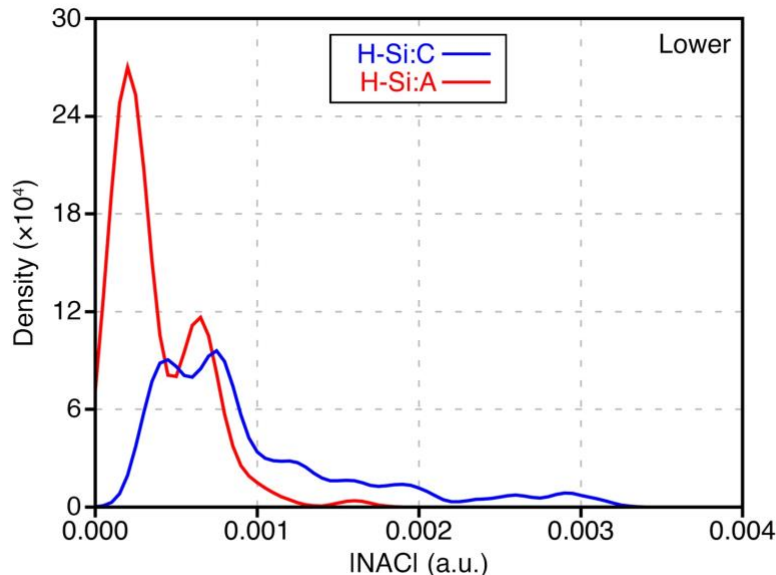
Figure 4.11 | Density of NAC as a function of NAC magnitude between the hot electron state and the lower-lying semiconductor states at the H-Si:C (blue) and H-Si:A (red) interfaces. Bin size of 5×10^{-4} was used for the Gaussian broadening where $\sigma^2=5\times10^{-7}$.

semiconductor and the molecule lead to the significant difference between the low and high-coverage interfaces in terms of the HET efficiency.

Another key difference is that the H-Si:A interface shows much larger HET probability than the H-Si:C interface. This can be explained by the difference in the NACs between the hot electron state and the lower-lying semiconductor states. Large NACs for the H-Si:C interface (see **Figure 4.11**) allow rapid return of the excited electron from the adsorbed molecule back to the semiconductor, inhibiting the probability build-up for the hot electron state localized within the molecule. The electronic energies are another ingredient that is ultimately responsible for the quantum dynamics. To examine if the significant HET probability at the H-Si:A interface could also be due to the fact that its hot electron state is energetically close to the initial state in the semiconductor, we performed another simulation for the H-Si:A interface with the hot electron state that is artificially shifted away to be the same energy as the H-Si:C case. The comparison of
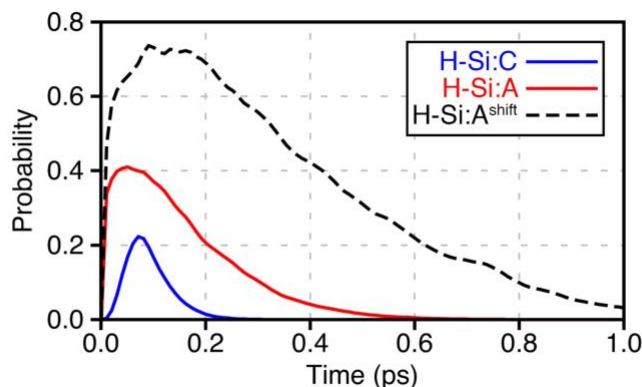
Figure 4.12 | Probability change of the hot electron state for the interfaces of H-Si:C (blue), H-Si:A (red), and H-Si:A^{shift} (dashed black). H-Si:A^{shift} represents the case where the hot electron state was artificially shifted away to the same energy of the H-Si:C interface.

the probability change for the hot electron state before and after shifting the hot electron state at the H-Si:A interface as well as the one at the H-Si:C interface is shown in **Figure 4.12**. What we found in comparison between H-Si:A and H-Si:A^{shift} is that the excited electron in the semiconductor transition to other semiconductor states more predominantly when the hot electron state is high-lying (the H-Si:A case). When the hot electron state is lower in energy, the excited electron is transitioned from more number of semiconductor states into the hot electron state while the hot electron undergoes relaxation within the semiconductor. As can be seen in **Figure 4.12**, the artificially-constructed simulation yields even higher HET probability compared to the original case, indicating that the energetic proximity of the hot electron state to the initial excited state is not the reason for the significant higher HET probability at the H-Si:A interface compared to the H-Si:C case as shown in **Figure 4.6a**.

4.4 Summary

In conclusion, we investigated the extent to which surface coverage and molecular adsorbate species influence the hot electron transfer (HET) process at semiconductor-molecule interfaces

using first-principles electron dynamics simulations. Our work shows that increasing the surface coverage does not necessarily enhance the HET probability as is often assumed. This is because the accepting molecular states for the hot electron can be delocalized among the adsorbed molecules at the semiconductor surface and the nonadiabatic couplings can be altered as a result. In fact, for both the Alizarin and the Cyanidin molecules we considered here, the HET process from semiconductor to the adsorbed molecule is significantly suppressed when the surface coverage is increased. The adsorbed molecular species itself was found to affect HET significantly. The fundamental reason for these observations can be traced back to the decisive role nonadiabatic couplings play in controlling the HET across the semiconductor surface and the adsorbed molecule. Developing a "design principle" at a molecular level for enhancing the HET process at semiconductor-molecule interfaces remains a great challenge, and controlling nonadiabatic couplings must be part of such a design principle in addition to the interface electron energy alignment as is often discussed.

CHAPTER 5: EXAMINING THE EFFECT OF EXCHANGE-CORRELATION APPROXIMATION IN FIRST-PRINCIPLES DYNAMICS SIMULATION OF INTERFACIAL CHARGE TRANSFER

5.1 Introduction

Interfacial electron transfer is at the heart of various optical and electronic device applications.[3-6,8-11] For instance, dynamics of excited electrons and holes (hot carriers) at heterogeneous interfaces play an essential role in achieving high conversion efficiency in solar cells,[10,12-13] and it is also of great interest for optoelectronic applications such as light-emitting diodes.[2,14-15] Developing a comprehensive knowledge of hot carrier dynamics calls for accurate modeling of excited carrier dynamics at an atomistic level because impartial interpretation of spectroscopic measurements is challenging when various processes operate with similar timescales. To this end, nonadiabatic molecular dynamics (NAMD)[43,46,79-81] have become quite popular in recent years for investigating hot carrier dynamics at semiconductor-molecule interfaces.[30,43,75,82-84] There exist various formulations of NAMD based on density functional theory (DFT) calculations.[77] A popular NAMD approach for studying hot carrier dynamics in large systems is based on fewest-switches surface hopping (FSSH) simulations[44,46,61,76] in the single-particle description with the so-called classical-path approximation (CPA).[43-44,132]

Three important ingredients are obtained from first-principles electronic structure calculations based on DFT for performing the FSSH simulation in this context: (i) nonadiabatic couplings (NACs), (ii) single-particle energy levels, and (iii) atomic trajectories (lattice movement). Despite the significant advancements and physical insights obtained from these simulations,[43,75,82-87] quantitative details of such simulations ultimately depend on the exchange-correlation (XC) approximation in DFT. Recently, Lin and Akimov reported that the PBE-GGA approximation[111] overestimates NACs up to an order of magnitude in comparison to those computed using the HSE06/PBE0-GGA-hybrid functionals[133-138] by considering silicon hydride molecules and silicon quantum dots.[78] The XC-derived differences in the NAC magnitudes were found to be size-dependent, due to the asymptotic behavior of the corresponding exchange functionals. Their work on the NACs sheds a key insight into how the underlying DFT electronic structure calculations could influence the NAMD simulation.

In this chapter, we examine the extent to which and how the XC approximation influences the interfacial charge transfer dynamics in the widely used NAMD simulation based on the FSSH approach discussed above. We are particularly interested in finding out how reliable the first-principles simulation could be for a "worst-case scenario". We consider an interface between a boron-nitride (BN) sheet and lithium ion (Li^+), which is likely a "severe" case in terms of the XC-introduced error. On one side of the interface, there are highly delocalized extended electronic states on the BN sheet, and there is a strongly localized electronic state resides on the monovalent Li^+ on the other side. The degree of localization of these electronic states and consequently the energy level alignments among them could be quite sensitive to the XC approximation because of the notorious self-interaction error.[139-140]
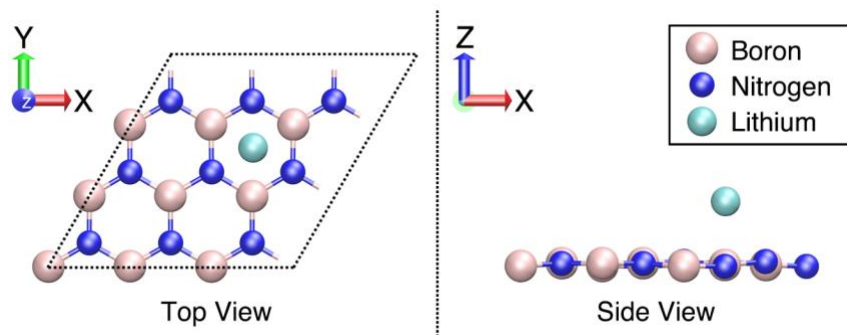
Figure 5.1 | Top and side view of the 3×3 super cell used in our calculations. Pink, blue, and cyan spheres represent B, N, and Li atoms, respectively.

5.2 Computational Details and Interface Model

In this present work, we consider a representative heterogeneous interface between a hexagonal boron-nitride (*h*-BN) sheet and lithium ion (Li$^+$). The 3×3 interface super cell employed in this work is shown in **Figure 5.1**. In our calculations, the interface was modeled by periodically repeating symmetric slabs. The vacuum region between the repeated slabs was set to 15 Å, so the interaction between the repeating slabs in the vacuum direction is negligible. The BN-Li$^+$ interface is chosen as the model system because different localizations of the wave functions across this interface make the simulations quite sensitive to the XC functionals for investigating a "worst-case scenario". We are able to identify the electronic states that are significantly contributed from the BN sheet and Li$^+$, respectively. Details will be discussed in the next section.

First-principles molecular dynamics (FPMD) simulations were performed for 12 ps with a time step of 0.48 fs at 295 K using a modified version of the Qbox code.[113] The Kohn-Sham (KS) wave functions were represented in plane-wave basis using norm-conserving pseudopotentials[112] with a kinetic energy cutoff of 50 Ry. Generalized gradient approximation parameterized by Perdew, Burke, and Ernzerhof (PBE[111]) and its hybrid (PBE0[133-134]) approximation were used for the exchange-correlation functional. Although the recursive subspace bisection algorithm[141-142] is
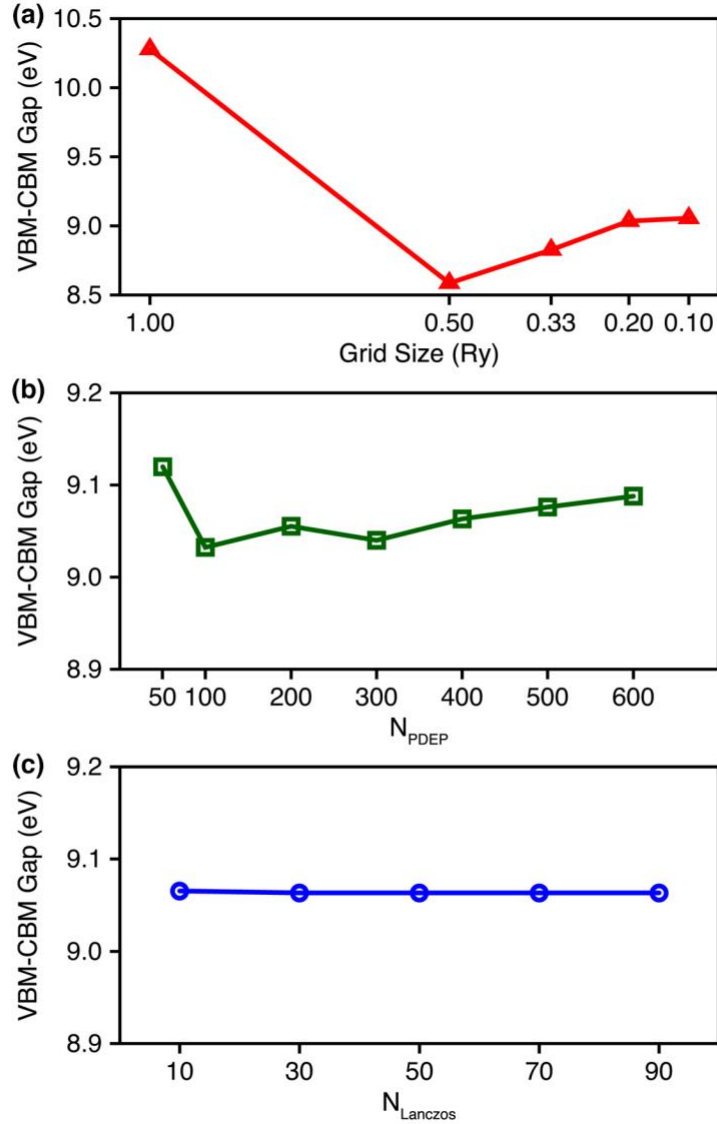
Figure 5.2 | Convergence tests of the parameters of (a) contour grid size (grid size), (b) projective dielectric eigenpotential basis vectors (N_{PDEP}), and (c) Lanczos steps ($N_{Lanczos}$) used in the G_0W_0 calculations with respect to the energy gap.

implemented in the Qbox code for hybrid XCs, we did not use the scheme. The KS single-particle energies and NACs were obtained from the FPMD simulation using the numerical prescription by Hammes-Schiffer and Tully.[76] Fewest-switches surface hopping (FSSH) simulation was then performed within the classical-path approximation (CPA) as described in Ref 30. This allows us to use a large number of atomic trajectories for converging the ensemble-averaged quantities

because the trajectories do not depend on the hops within the CPA. First, an ensemble of 4000 trajectories was generated by taking a 10 ps trajectory from various different temporal points in the FPMD simulation. Thus, each of these 10 ps long trajectories starts with different positions and momenta for atoms. Then, 500 FSSH simulations were performed for each trajectory, converging the sampling of the hopping probability distribution using the Monte Carlo method. A more detailed description can be found in Ref 30.

Quasi-particle (QP) energies were calculated using many-body perturbation theory, starting from KS wave functions and energies. Many-body corrections (MBCs) were calculated within the so-called "one-shot" G_0W_0 approximation,[106-108] starting from PBE and PBE0 KS wave functions and eigenvalues with the random-phase approximation for the screened Coulomb interaction. G_0W_0 calculations were performed using the WEST code[143] with the starting KS states obtained from Quantum Espresso code.[114] In our G_0W_0 calculations, we used a grid size of 0.10 Ry in the contour deformation technique[143] to evaluate the self-energy, 400 projective dielectric eigenpotential basis vectors to represent the dielectric matrix, 50 Lanczos steps for evaluating the irreducible polarizability, which is sufficient to obtain a well-converged energy gap within 0.025 eV. The convergence test for the G_0W_0 calculations are detailed in **Figure 5.2**.

5.3 Results and Discussion

5.3.1 Energy level alignments and atomic trajectory

Atom-projected density of states (PDOS) of the BN-Li$^+$ interface for the PBE and PBE0 XC functionals are shown in **Figure 5.3a** and **Figure 5.3b**, respectively. The lowest unoccupied electronic state is set as the reference energy of zero. For the PBE calculation, the lowest unoccupied molecular state (LUMO) is localized predominantly on the Li$^+$ (70% localization on the Li ion),
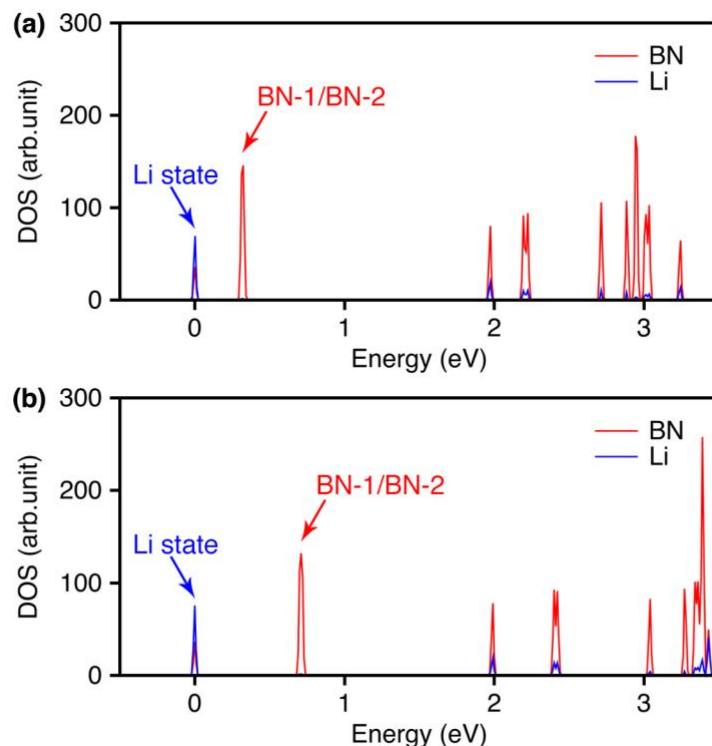
Figure 5.3 | Atom-projected density of states (PDOS) calculated using (a) PBE and (b) PBE0 XC approximations. The lowest unoccupied electronic state (Li state) is set to 0 as the reference energy.

and it is referred to as the Li state throughout this paper for convenience. Two quasi-degenerate states (LUMO+1 and LUMO+2) belong to the BN sheet (99%), and they are referred to as the BN-1 and BN-2 states in this work. Other unoccupied electronic states are highly delocalized over both the BN sheet and the Li ion. Although PBE0 approximation exhibits similar localization features for the Li state (72% localization on the Li ion) and BN states (99% localization on the BN sheet) as shown in **Figure 5.3b**, the energy level alignments are quite different between the PBE and PBE0 calculations. The energy difference between the Li state and BN-1 state are 0.31 eV and 0.70 eV for the PBE and PBE0 functionals, respectively.

Additionally, the lattice movement depends on the XC approximation. As shown in **Figure 5.4a**, PBE and PBE0 functionals show distinctly different distributions for the normal distance between
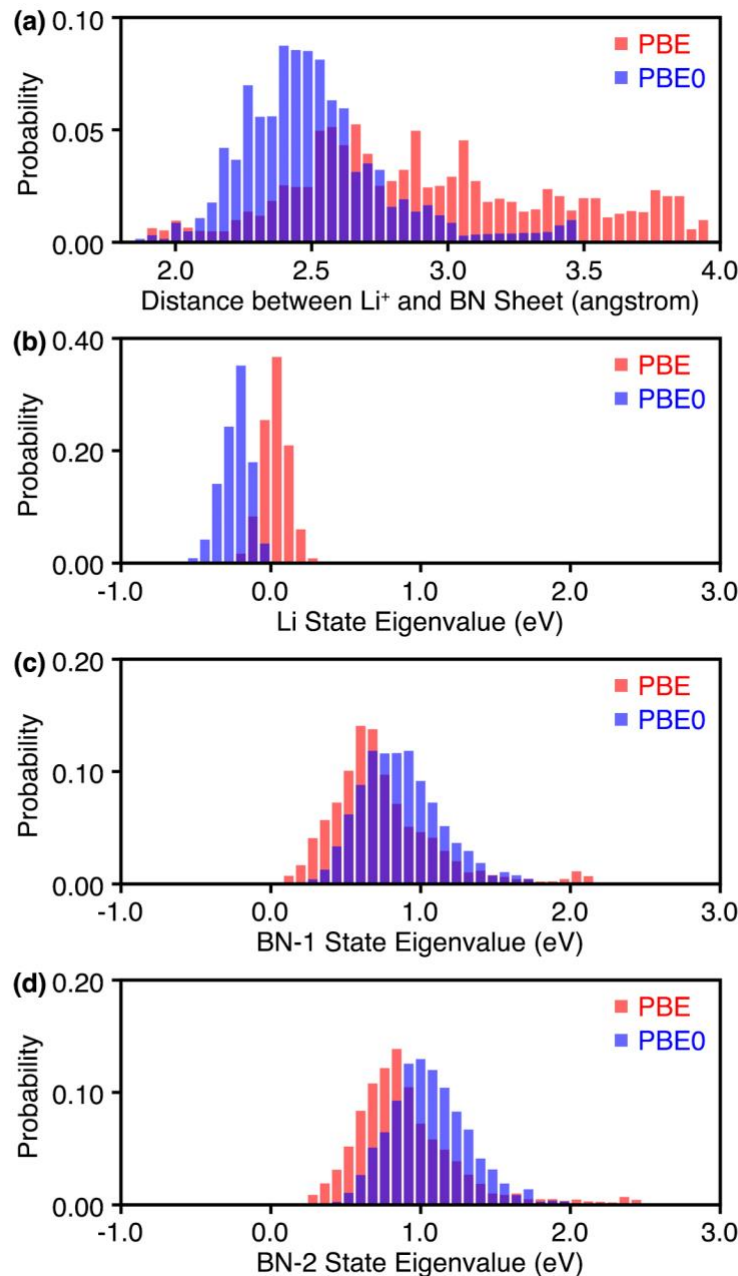
Figure 5.4 | (a) The normalized distribution of the normal distance between the Li ion and the BN sheet in FPMD simulations with PBE (red) and PBE0 (blue) XC approximations. The normalized distribution of the KS eigenvalues in FPMD simulations with PBE (red) and PBE0 (blue) XC approximations, for (b) Li state, (c) BN-1 state, and (d) BN-2 state. The eigenvalue of the Li state at the equilibrium structure is set to 0 as the reference energy for the eigenvalue distribution figures.

the Li ion and BN sheet. The FPMD simulation based on the PBE approximation shows the

distance distribution that is much broader and also centered farther than the FPMD result based on the PBE0 approximation. At the same time, the distributions of the eigenvalues in the FPMD simulations with the PBE and PBE0 approximations are similar, although their centers are shifted as shown in **Figure 5.4b-d**.

5.3.2 Nonadiabatic couplings

We now discuss the XC potential dependence of the nonadiabatic couplings (NACs). We implemented the numerical calculation of NACs using the time derivative by enforcing the phase continuity as in Refs 30,92-93, and they are calculated efficiently on-the-fly within the FPMD simulation. The NACs can be expressed as

$$
\begin{aligned}
D_{ij} &= \left\langle \psi_i\big(R(t)\big) \left| \frac{\partial}{\partial t} \right| \psi_j\big(R(t)\big) \right\rangle \\
&= \left\langle \psi_i\big(R(t)\big) \left| \nabla_R \right| \psi_j\big(R(t)\big) \right\rangle \cdot \frac{dR}{dt} \\
&= \frac{\left\langle \psi_i\big(R(t)\big) \left| \nabla_R \widehat{H} \right| \psi_j\big(R(t)\big) \right\rangle}{\varepsilon_j(R(t)) - \varepsilon_i(R(t))} \cdot dR/dt
\end{aligned}
\tag{5.1}
$$

where D_{ij} is the nonadiabatic coupling (NAC) between two states i and j, $\psi_i\big(R(t)\big)$ and $\varepsilon_i(R(t))$ are the single-particle eigenfunction and eigenvalue for state i at the nuclear coordinate $R(t)$, and $\widehat{H}$ is the Kohn-Sham Hamiltonian. The time-averaged magnitudes of the NAC matrices calculated using PBE and PBE0 approximations in the FPMD simulation are shown for the unoccupied electronic states in **Figure 5.5a**. The lowest unoccupied state (i.e. the Li state) is set to 1 as the reference state index. We focus on the nonadiabatic couplings between the Li state (state index of 1) and BN states (state indices of 2 and 3) to understand how the XC approximation influences the
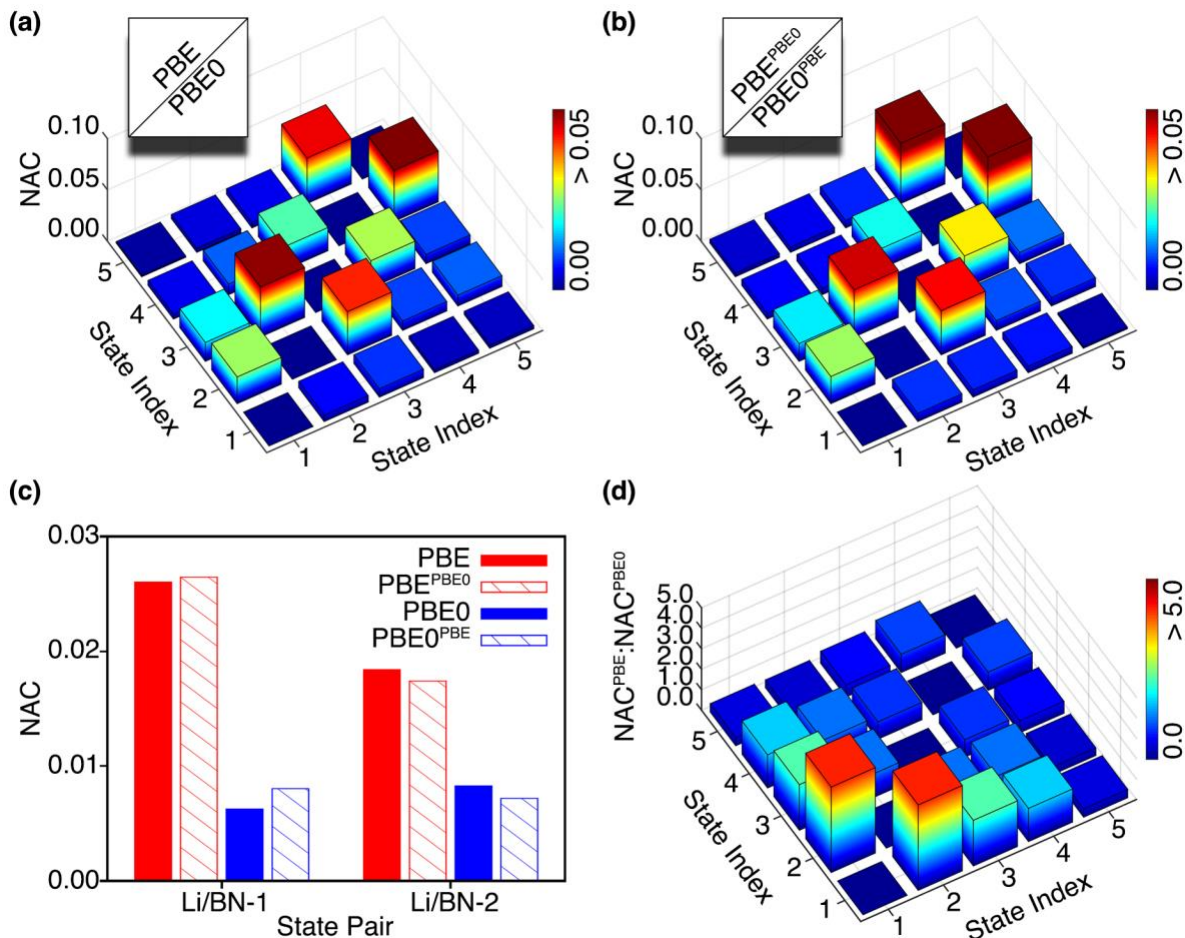
Figure 5.5 | Time-averaged nonadiabatic (NAC) matrices for unoccupied electronic states. State indices of 1, 2, and 3 represent the Li state (the lowest unoccupied electronic state), BN-1 state, and BN-2 state, respectively. NAC calculated from PBE and PBE0 approximations are shown in the upper-triangle and lower-triangle of (a). NAC calculated from PBE^{PBE0} (NAC calculated with PBE functional using the FPMD trajectories based on the forces from the PBE0 functional) and $PBE0^{PBE}$ (NAC calculated with PBE0 functional using the FPMD trajectories based on the forces from the PBE functional) are shown in the upper-triangle and lower-triangle of (b). Time-averaged NAC values between the Li state (index of 1) and BN states (index of 2 and 3) computed from PBE, PBE0, PBE^{PBE0}, and $PBE0^{PBE}$ calculations are summarized in (c). Ratio of the NAC magnitudes between PBE and PBE0 calculations (NAC^{PBE}: NAC^{PBE0}) is shown in (d).

interfacial charge transfer dynamics. Therefore, only a small portion of the NAC matrix (i.e. NAC values among the first five unoccupied states) is shown. Because the NAC matrix is antisymmetric with the diagonal elements being 0, we show the PBE and PBE0 comparison in the matrix figure as the upper-triangle and lower-triangle, respectively. In the time-averaged NAC matrices,

elements (1,2) and (1,3) represent the nonadiabatic couplings between the Li state and BN states and their magnitudes are summarized in **Figure 5.5c** for clarity. **Figure 5.5c** shows that compared to the PBE0 approximation, nonadiabatic couplings between the Li state and BN states obtained from the PBE functional overestimates the NACs by 318% for $NAC_{Li/BN-1}$ and 123% for $NAC_{Li/BN-2}$. Similar trends were recently reported by Lin and Akimov for silicon hydride molecules and silicon quantum dots.[78] They found that the PBE functional could overestimate NACs up to an order of magnitude, in comparison to those computed using hybrid XC functionals. The ratio of the time-averaged NAC magnitudes between PBE and PBE0 (NAC^{PBE}: NAC^{PBE0}) is shown in **Figure 5.5d**, where the diagonal elements are simply set to 0. Except for the NAC elements (1,2) and (1,3), other NAC elements do not exhibit significant difference between the PBE and PBE0 functional calculations because the corresponding electronic state pairs are highly delocalized over the BN-Li+ interface and thus not very sensitive to the XC approximation. This observation is consistent with the Hartree-Fock exchange in the hybrid functional reducing the delocalization error of the KS wave functions,[139-140] therefore minimizing NAC magnitudes.[78] The overestimation of the $NAC_{Li/BN-1}$ and $NAC_{Li/BN-2}$ obtained using the PBE functional can be also explained by its smaller energy separations compared to the corresponding PBE0 values (see **Figure 5.3**) since the NAC is roughly proportional to the reciprocal of the energy separation between two states i and j when the KS wave functions do not vary considerably between the XC functionals (see EQUATION 5.1).

While the differences between the PBE and PBE0 calculations for the NACs might be reasonably attributed to the extent of the KS wave function localization, the FPMD simulations show the XC-dependent atomic trajectories as well. Given the significant difference in the lattice movement as shown in **Figure 5.4a**, the XC-derived differences in the NAC magnitudes might not be necessarily due to the KS wave functions (see EQUATION 5.1). In order to quantify the relative

importance of the wave function characteristics and the lattice movement for the NAC differences, we calculated NACs with the PBE functional using the FPMD trajectories based on the forces from the PBE0 functional (referred to as PBE^{PBE0}), and vice versa (PBE0^{PBE}). The time-averaged magnitudes of the NAC matrices calculated from the PBE^{PBE0} and PBE0^{PBE} calculations are shown in **Figure 5.5b**. We show the PBE^{PBE0} and PBE0^{PBE} comparison in the matrix figure as the upper-triangle and lower-triangle, respectively. The NAC values between the Li state and the two BN states are summarized in **Figure 5.5c** for clarity as well. The NACs between the Li state and BN states are quite similar between the PBE and PBE^{PBE0} results as well as between the PBE0 and PBE0^{PBE} calculations. At the same time, the NAC values differ considerably between the PBE^{PBE0} and PBE0 calculations as well as between the PBE0^{PBE} and PBE calculations. Therefore, we conclude that the differences in the NACs between the PBE and PBE0 calculations derive from the wave functions rather than from the lattice movement although the atomic trajectories are quite different between the FPMD simulations based on the PBE and PBE0 forces (see **Figure 5.4a**).

5.3.3 Interfacial charge transfer dynamics

As discussed in Introduction, the FSSH method is a widely employed NAMD simulation approach used for studying interfacial charge transfer.[44,46,61,76] In particular, formulation of the FSSH within the single-particle description has been pioneered by Prezhdo and co-workers within the so-called classical-path approximation (CPA).[43-44] The CPA assumes a classical equilibrium path that is representative of the system's nuclei at all times and surface hops do not significantly influence the nuclear dynamics. The time/trajectory-dependent single-particle energy levels and the NACs are both key elements in the FSSH approach for modeling the excited electron dynamics.[30,44]

As discussed above, PBE and PBE0 XC functionals yield distinctly different energy level alignments between the Li state and BN states. Going beyond the non-interacting electron picture of KS-DFT, it would be more appealing to employ the quasi-particle (QP) description using many-body perturbation theory approach.[132] In the so-called "one-shot" G_0W_0 approximation,[106-108] the QP energies depend on the starting DFT wave functions, thus QP energies are dependent of the XC approximations as well. Even within the G_0W_0 approximation, it is computationally impractical to take into account the time/trajectory dependence of the QP energies. Instead, we obtain the many-body corrections (MBCs) on top of KS energies at the equilibrium geometry, and we apply the computed MBCs to correct the time/trajectory-dependent KS energies to obtain the QP energies along the atomic trajectories, i.e. $\varepsilon_i^{G0W0@PBE}(t) = \varepsilon_i^{PBE}(t) + \Delta\epsilon_i^{MBC@PBE}(t = 0)$. This approach has been used successfully in our previous work of investigating excited electron dynamics at heterogeneous interfaces.[30] We first examine the validity of this approximation for this specific interface case by calculating the MBCs at several different geometries from the FPMD simulation. The MBCs were calculated for several structures that are taken from the FPMD simulation at evenly spaced time intervals (at t=2, 4, 6, and 8 picoseconds). **Figure 5.6** compares these MBCs to the MBCs obtained at the equilibrium structure. The averaged MBCs and their standard deviation for different electronic states (the Li state, BN-1 state, and BN-2 state) are also shown in **Figure 5.6**. Starting from the PBE XC approximation in the G_0W_0 calculation, the standard deviations of the MBCs were calculated to be 0.02, 0.38, and 0.37 eV for the Li state, BN-1 state, and BN-2 state, respectively. These standard deviations are quite minor in comparison to the averaged MBC values of 1.96, 2.42, and 2.49 eV. Starting from the PBE0 XC approximation in the G_0W_0 calculation, the standard deviations (0.02, 0.31, 0.31 eV for the Li, BN-1, and BN-2 state) are also much smaller than the averaged MBCs (1.44, 2.11, and 2.14 eV for the Li state, BN-1
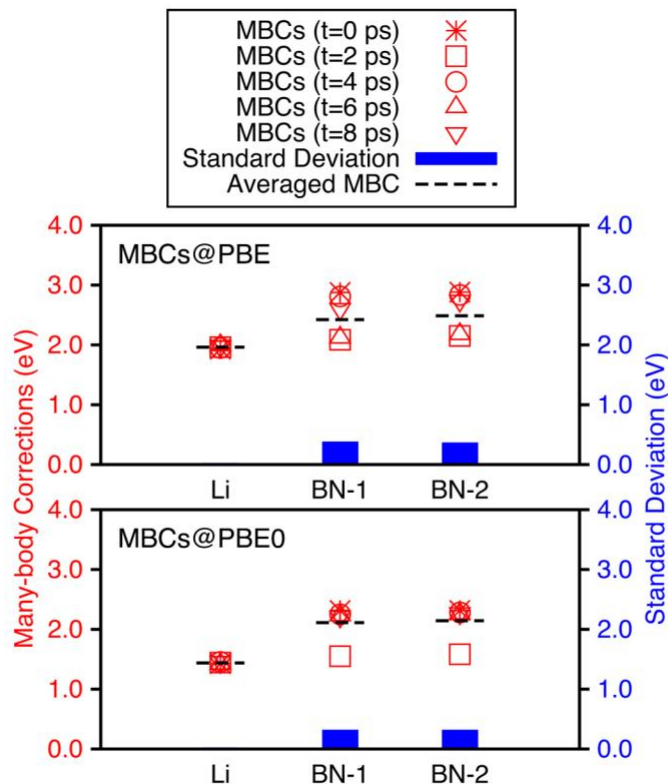
Figure 5.6 | Red symbols show many-body corrections (MBCs) for the equilibrium structure (at t=0 ps) and the dynamical structures that are taken from the FPMD simulations at evenly spaced time intervals (at t=2, 4, 6, and 8 ps). The averaged MBCs (black dashed line) and the standard deviation (blue box) for the electronic states are also shown.

state, and BN-2 state). These standard deviations are small enough such that the time/trajectory dependence of the MBCs can be neglected in the following FSSH simulations.

We consider here the extent to which the charge transfer kinetics is influenced by the XC approximation using the FSSH simulation. Four different cases are compared: (1) PBE energy levels with PBE NAC (ε^{PBE}: NAC^{PBE}), (2) PBE0 energy levels with PBE0 NAC (ε^{PBE0}: NAC^{PBE0}), (3) G_0W_0@PBE energy levels (QP energies starting from PBE-XC) with PBE NAC ($\varepsilon^{G0W0@PBE}$: NAC^{PBE}), and (4) G_0W_0@PBE0 energy levels (QP energies starting from PBE0-XC) with PBE0 NAC ($\varepsilon^{G0W0@PBE0}$: NAC^{PBE0}). The time-averaged energy level alignments from the PBE, PBE0, G_0W_0@PBE, and G_0W_0@PBE0 calculations are shown in **Figure 5.7**. The excited
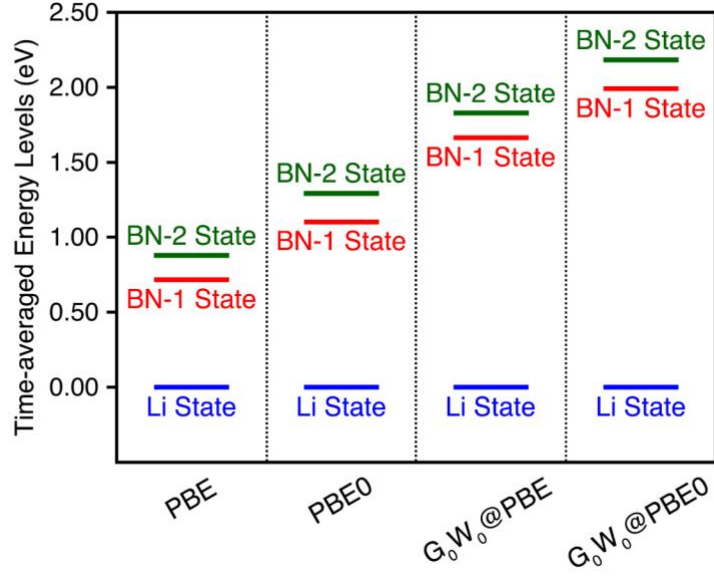
Figure 5.7 | Time-averaged energy levels from the FPMD simulation of the Li state (blue), BN-1 state (red), and BN-2 state (green) according to PBE, PBE0, G_0W_0@PBE, and G_0W_0@PBE0 calculations. The Li state is set to zero as the reference energy.
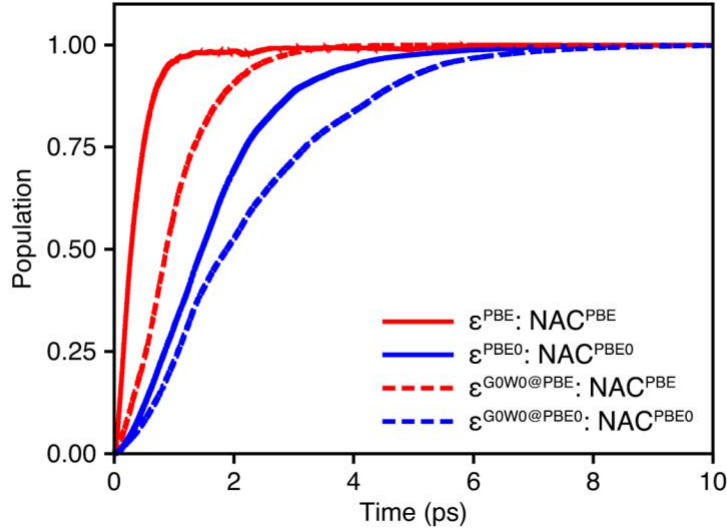
Figure 5.8 | Population change of the Li state calculated from the different ε: NAC combinations. Fitting the population change of the Li state to the two-state model given by Eq. 5.2 yields the time constant of the interfacial charge transfer as 0.37, 1.05, 1.74, and 2.40 ps for ε^{PBE}:NAC^{PBE}, $\varepsilon^{G0W0@PBE}$:NAC^{PBE}, ε^{PBE0}:NAC^{PBE0}, and $\varepsilon^{G0W0@PBE0}$:NAC^{PBE0}.

electron was initially placed in the BN-2 state in the FSSH simulations, and we follow the interfacial charge transfer through the population change in the Li state as shown in **Figure 5.8**. By

Table 5.1 | Interfacial charge transfer time constant τ calculated by fitting the population change of the Li state to Eq. 5.2 according to different **ε: NAC** pairs.

ε: NAC	ε^{PBE} NAC^{PBE}	$\varepsilon^{G0W0@PBE}$ NAC^{PBE}	ε^{PBE0} NAC^{PBE0}	$\varepsilon^{G0W0@PBE0}$ NAC^{PBE0}
τ (ps)	0.37	1.05	1.74	2.40

fitting the population change of the Li state to a two-state model

$$P_{Li}(t) = 1 - exp(-t/\tau) \tag{5.2}$$

the time constant τ can be obtained for the interfacial charge transfer as summarized in **Table 5.1**. The time constant varies by almost an order of magnitude from sub-picosecond to few picoseconds, depending on the ε: NAC combination. As expected, the energy level alignments play an important role as can be seen, for example, by comparing ε^{PBE}: NAC^{PBE} (0.37 ps), and $\varepsilon^{G0W0@PBE}$: NAC^{PBE} (1.05 ps). Here, we find that the interfacial charge transfer rate is quite sensitive to both the energy level alignments and nonadiabatic coupling while the lattice movements (atomic trajectories) were found unimportant as discussed above.

5.4 Summary

In conclusion, we examined the extent to which exchange-correlation (XC) approximation influences modeling of interfacial charge transfer using fewest-switches surface hopping (FSSH) simulation within the single-particle description.[43-44] We considered a heterogeneous interface between a lithium ion (Li$^+$) and an extended boron-nitride (BN) sheet here, being an extreme case in which wave function localization and the energy level alignments are highly sensitive to the XC

approximation. Generalized gradient approximation (PBE) and its hybrid (PBE0) approximation were examined in this work because the hybrid PBE0 approximation is known to remedy some key shortcomings of the PBE-GGA approximation. The PBE0 hybrid XC approximation yields nonadiabatic couplings (NACs) that are significantly smaller than the PBE-GGA approximation by an order of magnitude for localized electronic states. This is consistent with the recent finding by Lin and Akimov on silicon clusters.[78] This XC-derived difference in the NACs was found to stem from the Kohn-Sham (KS) wave function characteristics rather than from the lattice movement although first-principles molecular dynamics trajectories, along which NACs are obtained, differ noticeably between the two XC functionals.

In addition to NACs, the FSSH simulation depends on the energy levels. While we do not employ the NAC calculation from quasi-particle (QP) wave functions because of its prohibitively large computational cost, we examined how the use of QP energies influences the simulation result. The interfacial charge transfer time scale was found to vary as much as, but not more than, one order of magnitude from sub-picosecond to few picoseconds. The time scale is quite sensitive to both the energy level alignments and NAC while the lattice movements (atomic trajectories) were found unimportant. While the order of magnitude consistency for the charge transfer rate for this rather extreme model of heterogeneous interface (consisting of a lithium ion and an extended boron-nitride sheet) is encouraging, continued advancement in electronic structure methods is required for quantitatively accurate determination of the transfer rate. Although we focused here on the single-particle description for investigating excited electron transfer, we note here that the NACs between the many-body ground state and an excited state are also related to the NACs among the KS single-particle states.[132,144-150] Nonadiabatic dynamics simulations based on the

linear-response time-dependent DFT for describing excited states[77] might observe a similar dependence on the XC approximation.

CHAPTER 6: CONCLUSIONS

To realize better device performance for several advanced technological applications, a quantitative and predictive understanding of excited charge carrier dynamics must be obtained. In particular, excited carrier dynamics at semiconductor-molecule heterogeneous interface is of great concern in photovoltaic and photoelectrochemical devices that are based on the dye-sensitized solar cell (DSSC) concept, because such a dynamical process significantly impacts the device performance. Although transient absorption spectroscopy measurements have been extensively used to investigate excited electron dynamics, isolating the spectral signatures and excited carrier dynamics that are specific to distinct dynamical processes is still challenging. This is because several dynamical processes with similar time scales are operating simultaneously at the heterojunctions during the excited carrier relaxation. These dynamical processes can occur in parallel, they compete with each other and ultimately determine the efficiency of the device. Most importantly, the interplay among these kinetic processes that excited carriers can undergo significantly obfuscates the details of excited carrier dynamics. Realizing these difficulties, developing a comprehensive knowledge of excited carrier dynamics in complex systems (such as semiconductor-molecule heterogeneous interfaces) calls for accurate modeling of excited carrier dynamics at the atomistic level. In this work, we developed and applied a quantitative formulation based on first-principles (*ab initio*) quantum theory to elucidate how excited carrier processes at semiconductor-molecule interfaces depend on the atomistic details, such as molecular chemisorption, defect states, and adsorbate species on the surface.

We turned to first-principles quantum theory simulations because they are able to provide a unique perspective on the excited carrier dynamics and most closely mimic the processes as they can occur in nature. First-principles simulation complements the simplified phenomenological models, which allowed us to systematically investigate the influence of various interface characteristics of the excited carrier dynamics by varying the model parameters. The atomistic simulation treats the interface in full, realistic detail, and describes the evolving geometric and electronic structure of the organic molecule and the semiconductor surface in real time. The *ab initio* treatment of the interface makes it possible to avoid fitting parameters and to build the theory starting from the fundamental laws of physics. In this work, we investigated excited charge carrier dynamics at heterogeneous interface between semiconductor and organic molecules from several aspects by synergistically combining the fewest-switches surface hopping (FSSH) algorithm, G_0W_0 many-body perturbation theory calculations, and first-principles molecular dynamics.

First, we investigated hot electron dynamics at semiconductor-molecule type-II interface by studying a representative interface between a hydrogen-passivated silicon (111) surface and cyanidin molecule. The interfacial electron transfer from semiconductor to the adsorbed molecule was found to be largely decoupled from the excited electron relaxation process within the semiconductor conduction band. While the hot electron relaxation was found to take place on a time scale of several hundred femtoseconds, the subsequent interfacial electron transfer was slower by an order of magnitude. At the same time, this secondary process of picosecond electron transfer is comparable in time scale to typical electron trapping into defect states in the energy gap. However, the corresponding time scale of the interfacial electron transfer is much shorter than the typical time scales reported for back electron transfer between a semiconductor and a molecule in the case of oxide materials. These findings point to the importance of excited electron trapping by

defect-induced states below the conduction band for understanding the overall back electron transfer mechanism for oxide materials. At the same time, hot electron transfer from semiconductor to the adsorbed molecule at high energy levels was observed at this representative interface, although the lifetime of excited electron within the adsorbed molecule was short. How hot electron transfer among adsorbed molecules might influence the residence time of excited electron within the molecule is another interesting question for a future study.

Following the previous work, we investigated the extent to which molecular details such as surface coverage and molecular adsorbate species influence the hot electron transfer (HET) process at semiconductor-molecule heterogeneous interfaces. Our work shows that increasing the surface coverage does not necessarily enhance the HET probability as is often assumed. This is because the accepting molecular states for the hot electron can be delocalized among the adsorbed molecules at the semiconductor surface and the nonadiabatic couplings can be altered as a result. In fact, for both the adsorbed molecule species we considered here (alizarin and cyanidin), the HET process from semiconductor to the adsorbed molecule is significantly suppressed when the surface coverage is increased. The adsorbed molecular species itself was also found to affect HET significantly. The fundamental reason for these observations can be traced back to the decisive role nonadiabatic couplings play in controlling the HET across the semiconductor surface and the adsorbed molecule. Although developing a "design principle" at a molecular level for enhancing the HET process at semiconductor-molecule interfaces remains a great challenge for the community, controlling nonadiabatic couplings must be part of such a design principle in addition to the interface electron energy alignment as is often discussed.

To date, we have shown that our first-principles electron dynamics simulations are able to offer insights into the atomistic details of excited carrier dynamics at semiconductor-molecule

heterogeneous interfaces. However, there still exist some challenges for such a numerical approach based on the FSSH algorithm: (i) how accurate are the single-particle energies and nonadiabatic couplings (NACs) in describing excited carrier dynamics? (ii) How valid is the mixed quantum-classical description that we employed in our approach? The first question arises because the use of approximated exchange-correlation (XC) functionals in the first-principles molecular dynamics simulation, as well as in the G_0W_0 calculations. The second concern arises due to the fact that the decoherence effect was not taken into account in the density matrix for the excited carrier in our previous investigations. In this work, we addressed the first concern from first-principles quantum theory simulation, while the latter one still needs further detailed investigation.

We examined the extent to which the XC approximation influences modeling interfacial charge transfer using FSSH simulations within the single-particle description. A heterogeneous interface between a lithium ion and an extended boron-nitride sheet was considered, the system being an extreme case in which wave function localization and energy level alignments are highly sensitive to the XC approximation. The PBE0 hybrid XC approximation yields NACs that are an order of magnitude smaller than the values obtained from the PBE-GGA approximation for localized electronic states. This difference between the two XC functionals for the calculated NACs was found to derive mainly from the wave function characteristics rather than from the lattice movement although first-principles molecular dynamics trajectories, along which NACs are obtained, differ noticeably between the two XC functionals. Using the NACs and single-particle energy level alignments at different levels of theory, FSSH simulations were performed to model the electron transfer dynamics at the interface. The electron transfer time scale was found to vary as much as, but not more than, one order of magnitude. The time scale was found to be quite sensitive to both NACs and energy level alignments. While the order of magnitude consistency for

the charge transfer rate is encouraging even for this rather extreme example of a heterojunction interface, continued advancement in electronic structure methods is required for quantitatively accurate determination of the transfer rate.

APPENDIX A: DERIVATION OF THE EQUATION OF MOTION OF THE SINGLE-PARTICLE GREEN'S FUNCTION

Within many-body perturbation theory (MBPT), starting from the equation of motion (EOM) of single-particle Green's function, one can finally connect the interacting Green's function and non-interacting Green's function via Dyson's equation. In this section, the full derivation of the EOM of the single-particle Green's function is provided. It should be pointed out here that the derivation of the EOM of the single-particle Green's function can be found in many places in the literature, such as in the work by Friedrich and Schindlmayr,[151] as well as in the work by Yang and co-workers.[152] Such a complex and tedious derivation process varies significantly depending on the individual, although the fundamental structure stays the same. The notations in the derivation which I have presented here are consistent with the ones used in the main text of this dissertation.

Given the many-particle Hamiltonian

$$\hat{H} = \sum_i \left[-\frac{\hbar^2}{2m} \nabla_i^2 + v_{ext}(r_i) \right] + \frac{1}{2} \sum_{i,j} v(r_i, r_j) \tag{A1}$$

where m is the electron mass, $v_{ext}(r_i)$ is the potential created by the atomic nuclei, and $v(r_i, r_j)$ is the Coulomb interaction between two particles, which can be expressed in the following form

$$v(r, r') = \frac{e^2}{4\pi\varepsilon_0 |r - r'|} \tag{A2}$$

where e is the electron charge and ε_0 is the vacuum dielectric constant. When we use the field operators as defined in the SECTION 2.4.2 of the main text, EQUATION A1 can be expressed as

$$\hat{H} = \sum_\lambda \int dy \hat{\psi}_\lambda^\dagger(y) H_0 \hat{\psi}_\lambda(y)$$

$$+ \frac{1}{2} \sum_{\alpha'\beta'} \sum_{\delta'\gamma'} \iint dy dz \hat{\psi}_{\alpha'}^\dagger(y) \hat{\psi}_{\beta'}^\dagger(z) v_{\alpha'\beta'\delta'\gamma'}(y - z) \hat{\psi}_{\delta'}(z) \hat{\psi}_{\gamma'}(y). \tag{A3}$$

One should notice that EQUATION A3 is just a mathematical reformulation of EQUATION A1 and we have not included the time (t) in the above expressions nor in the following equations for the sake of simplicity. Instead, we will have t included later. Here we use short-hand notations of h_0 and v to represent the first term and the second term on the right-hand side of EQUATION A3, respectively. The physical meaning of these two parts are the same as we have discussed in the main text.

Realizing the fact that field operators satisfy the following relations

$$\left[\hat{\psi}_\alpha(x), \hat{\psi}_{\alpha'}(y)\hat{\psi}_{\beta'}(z)\right] = 0, when\ \alpha \neq \alpha'\ and\ \alpha \neq \beta' \tag{A4}$$

$$\left[\hat{\psi}_\alpha(x), \hat{\psi}_{\alpha'}^\dagger(y)\hat{\psi}_{\beta'}^\dagger(z)\right] = 0, when\ \alpha \neq \alpha'\ and\ \alpha \neq \beta' \tag{A5}$$

$$\left[\hat{\psi}_\alpha(r), \hat{\psi}_{\beta'}^\dagger(r')\right]_\mp = \delta_{\alpha\beta}\delta(r - r') \tag{A6}$$

$$\left[\hat{\psi}_\alpha(r), \hat{\psi}_\beta(r')\right]_\mp = \left[\hat{\psi}_\alpha^\dagger(r), \hat{\psi}_\beta^\dagger(r')\right]_\mp = 0 \tag{A7}$$

These four equations are going to be used in the following derivation. In addition, we have the following expression

$$\left[\hat{\psi}_\alpha(x), H\right] = \left[\hat{\psi}_\alpha(x), h_0 + v\right] = \left[\hat{\psi}_\alpha(x), h_0\right] + \left[\hat{\psi}_\alpha(x), v\right] \tag{A8}$$

Let's first evaluate the first term on the right-hand side of EQUATION A8 of $\left[\hat{\psi}_\alpha(x), h_0\right]$, by using EQUATION A6 and EQUATION A7 we have:

$$\begin{aligned}
\left[\hat{\psi}_\alpha(x), h_0\right] &= \sum_\lambda \int dy\, \hat{\psi}_\alpha(x)\hat{\psi}_\lambda^\dagger(y)h_0(y)\hat{\psi}_\lambda(y) - \sum_\lambda \int dy\, \hat{\psi}_\lambda^\dagger(y)h_0(y)\hat{\psi}_\lambda(y)\hat{\psi}_\alpha(x) \\
&= \sum_\lambda \int dy\left[\hat{\psi}_\alpha(x)\hat{\psi}_\lambda^\dagger(y)h_0(y)\hat{\psi}_\lambda(y) - \hat{\psi}_\lambda^\dagger(y)h_0(y)\hat{\psi}_\lambda(y)\hat{\psi}_\alpha(x)\right] \\
&= \sum_\lambda \int dy\, h_0(y)\left[\hat{\psi}_\alpha(x)\hat{\psi}_\lambda^\dagger(y)\hat{\psi}_\lambda(y) - \hat{\psi}_\lambda^\dagger(y)\hat{\psi}_\lambda(y)\hat{\psi}_\alpha(x)\right] \\
&= \sum_\lambda \int dy\, h_0(y)\left[\hat{\psi}_\alpha(x)\hat{\psi}_\lambda^\dagger(y) + \hat{\psi}_\lambda^\dagger(y)\hat{\psi}_\alpha(x)\right]\hat{\psi}_\lambda(y) \\
&= \sum_\lambda \int dy\, h_0(y)\left[\hat{\psi}_\alpha(x), \hat{\psi}_\lambda^\dagger(y)\right]_+ \hat{\psi}_\lambda(y)
\end{aligned} \tag{A9}$$

$$= \sum_{\lambda} \int dy h_0(y) \delta_{\alpha\lambda} \delta(x-y) \hat{\psi}_{\lambda}(y)$$

$$= h_0(x) \hat{\psi}_{\alpha}(x)$$

Now let's re-write the second term on the right-hand side of EQUATION A8 of $[\hat{\psi}_{\alpha}(x), v]$, by using

EQUATION A6 and EQUATION A7 we have:

$$[\hat{\psi}_{\alpha}(x), v] = \frac{1}{2} \sum_{\alpha'\beta'} \sum_{\delta'\gamma'} \int \int dy dz \hat{\psi}_{\alpha}(x) \hat{\psi}^{\dagger}_{\alpha'}(y) \hat{\psi}^{\dagger}_{\beta'}(z) v_{\alpha'\beta'\delta'\gamma'}(y-z) \hat{\psi}_{\delta'}(z) \hat{\psi}_{\gamma'}(y)$$

$$- \frac{1}{2} \sum_{\alpha'\beta'} \sum_{\delta'\gamma'} \int \int dy dz \hat{\psi}^{\dagger}_{\alpha'}(y) \hat{\psi}^{\dagger}_{\beta'}(z) v_{\alpha'\beta'\delta'\gamma'}(y-z) \hat{\psi}_{\delta'}(z) \hat{\psi}_{\gamma'}(y) \hat{\psi}_{\alpha}(x)$$

$$= \frac{1}{2} \sum_{\alpha'\beta'} \sum_{\delta'\gamma'} \int \int dy dz \left[\hat{\psi}_{\alpha}(x) \hat{\psi}^{\dagger}_{\alpha'}(y) \hat{\psi}^{\dagger}_{\beta'}(z) v_{\alpha'\beta'\delta'\gamma'}(y-z) \hat{\psi}_{\delta'}(z) \hat{\psi}_{\gamma'}(y) \right.$$

$$\left. - \hat{\psi}^{\dagger}_{\alpha'}(y) \hat{\psi}^{\dagger}_{\beta'}(z) v_{\alpha'\beta'\delta'\gamma'}(y-z) \hat{\psi}_{\delta'}(z) \hat{\psi}_{\gamma'}(y) \hat{\psi}_{\alpha}(x) \right]$$

$$= \frac{1}{2} \sum_{\alpha'\beta'} \sum_{\delta'\gamma'} \int \int dy dz \left[\hat{\psi}_{\alpha}(x) \hat{\psi}^{\dagger}_{\alpha'}(y) \hat{\psi}^{\dagger}_{\beta'}(z) v_{\alpha'\beta'\delta'\gamma'}(y-z) \hat{\psi}_{\delta'}(z) \hat{\psi}_{\gamma'}(y) \right.$$

$$\left. - \hat{\psi}^{\dagger}_{\alpha'}(y) \hat{\psi}^{\dagger}_{\beta'}(z) v_{\alpha'\beta'\delta'\gamma'}(y-z) \hat{\psi}_{\alpha}(x) \hat{\psi}_{\delta'}(z) \hat{\psi}_{\gamma'}(y) \right]$$

$$= \frac{1}{2} \sum_{\alpha'\beta'} \sum_{\delta'\gamma'} \int \int dy dz \left[\hat{\psi}_{\alpha}(x) \hat{\psi}^{\dagger}_{\alpha'}(y) \hat{\psi}^{\dagger}_{\beta'}(z) - \hat{\psi}^{\dagger}_{\alpha'}(y) \hat{\psi}^{\dagger}_{\beta'}(z) \right] v_{\alpha'\beta'\delta'\gamma'}(y \quad\quad\text{(A10)}$$

$$- z) \hat{\psi}_{\delta'}(z) \hat{\psi}_{\gamma'}(y)$$

$$= \frac{1}{2} \sum_{\alpha'\beta'}^{\alpha=\alpha'} \sum_{\delta'\gamma'}^{\alpha=\alpha'} \int \int dy dz \left[\hat{\psi}_{\alpha}(x), \hat{\psi}^{\dagger}_{\alpha'}(y) \hat{\psi}^{\dagger}_{\beta'}(z) \right] v_{\alpha'\beta'\delta'\gamma'}(y-z) \hat{\psi}_{\delta'}(z) \hat{\psi}_{\gamma'}(y)$$

$$+ \frac{1}{2} \sum_{\alpha'\beta'}^{\alpha=\beta'} \sum_{\delta'\gamma'}^{\alpha=\beta'} \int \int dy dz \left[\hat{\psi}_{\alpha}(x), \hat{\psi}^{\dagger}_{\alpha'}(y) \hat{\psi}^{\dagger}_{\beta'}(z) \right] v_{\alpha'\beta'\delta'\gamma'}(y$$

$$- z) \hat{\psi}_{\delta'}(z) \hat{\psi}_{\gamma'}(y)$$

$$= \frac{1}{2} \sum_{\alpha'\beta'}^{\alpha=\alpha'} \sum_{\delta'\gamma'}^{\alpha=\alpha'} \int dz \left[\hat{\psi}_{\alpha}(x), \hat{\psi}^{\dagger}_{\alpha'}(x) \hat{\psi}^{\dagger}_{\beta'}(z) \right] v_{\alpha\beta'\delta'\gamma'}(x-z) \hat{\psi}_{\delta'}(z) \hat{\psi}_{\gamma'}(x)$$

$$+ \frac{1}{2} \sum_{\alpha'\beta'}^{\alpha=\beta'} \sum_{\delta'\gamma'}^{\alpha=\beta'} \int dy \left[\hat{\psi}_{\alpha}(x), \hat{\psi}^{\dagger}_{\alpha'}(y) \hat{\psi}^{\dagger}_{\beta'}(x) \right] v_{\alpha'\alpha\delta'\gamma'}(y-x) \hat{\psi}_{\delta'}(x) \hat{\psi}_{\gamma'}(y)$$

Here we use the short-hand notation of I and II to represent $\left[\hat{\psi}_\alpha(x), \hat{\psi}_{\alpha'}^\dagger(x)\hat{\psi}_{\beta'}^\dagger(z)\right]$ and

$\left[\hat{\psi}_\alpha(x), \hat{\psi}_{\alpha'}^\dagger(y)\hat{\psi}_{\beta'}^\dagger(x)\right]$ in EQUATION A10. By using EQUATION A6 we have

$$
\begin{aligned}
I &= \hat{\psi}_\alpha(x)\hat{\psi}_\alpha^\dagger(x)\hat{\psi}_{\beta'}^\dagger(z) - \hat{\psi}_\alpha^\dagger(x)\hat{\psi}_{\beta'}^\dagger(z)\hat{\psi}_\alpha(x) \\
&= \hat{\psi}_\alpha(x)\hat{\psi}_\alpha^\dagger(x)\hat{\psi}_{\beta'}^\dagger(z) + \hat{\psi}_\alpha^\dagger(x)\hat{\psi}_\alpha(x)\hat{\psi}_{\beta'}^\dagger(z) \\
&= \left[\hat{\psi}_\alpha(x), \hat{\psi}_\alpha^\dagger(x)\right]_+ \hat{\psi}_{\beta'}^\dagger(z) \\
&= \hat{\psi}_{\beta'}^\dagger(z)
\end{aligned}
\tag{A11}
$$

and

$$
\begin{aligned}
II &= \hat{\psi}_\alpha(x)\hat{\psi}_{\alpha'}^\dagger(y)\hat{\psi}_\alpha^\dagger(x) - \hat{\psi}_{\alpha'}^\dagger(y)\hat{\psi}_\alpha^\dagger(x)\hat{\psi}_\alpha(x) \\
&= 0
\end{aligned}
\tag{A12}
$$

Now, insert EQUATION A11 and EQUATION A12 into EQUATION A10 we have

$$
\left[\hat{\psi}_\alpha(x), v\right] = \frac{1}{2}\sum_{\alpha'\beta'}\sum_{\delta'\gamma'}\int dz\, \hat{\psi}_{\beta'}^\dagger(z) v_{\alpha\beta'\delta'\gamma'}(x-z)\hat{\psi}_{\delta'}(z)\hat{\psi}_{\gamma'}(x)
\tag{A13}
$$

Inserting EQUATION A9 and EQUATION A13 into EQUATION A8, we have the following expression

$$
\left[\hat{\psi}_\alpha(x), H\right] = h_0(x)\hat{\psi}_\alpha(x) + \frac{1}{2}\sum_{\alpha'\beta'}\sum_{\delta'\gamma'}\int dz\, \hat{\psi}_{\beta'}^\dagger(z) v_{\alpha\beta'\delta'\gamma'}(x-z)\hat{\psi}_{\delta'}(z)\hat{\psi}_{\gamma'}(x)
\tag{A14}
$$

For field operators, the EOM can be read as

$$
i\frac{d}{dt}A = [A, H]
\tag{A15}
$$

Therefore, EQUATION A14 can be re-written as

$$
i\frac{\partial \psi_\alpha(x,t)}{\partial t} = h_0(x)\hat{\psi}_\alpha(x,t) + \sum_{\beta'}\sum_{\delta'\gamma'}\int dy\, \hat{\psi}_{\beta'}^\dagger(y) v_{\alpha\beta'\delta'\gamma'}(x-y)\hat{\psi}_{\delta'}(y)\hat{\psi}_{\gamma'}(x)
\tag{A16}
$$

where we have combined the α' and β' in EQUATION A14 due to the fact that they only represent

different spin conditions. Consequently, the pre-factor of $1/2$ in EQUATION A14 does not exist in

EQUATION A16 anymore. In addition, we have included time t in the expression and have switched

z to y in EQUATION A16 because x, y, and z are arbitrary indices. Now, let's left multiply both sides of EQUATION A16 by $\hat{\psi}_\alpha^\dagger(z,t_z)$, we can have the following relation

$$i\hat{\psi}_\alpha^\dagger(z,t_z)\frac{\partial\psi_\alpha(x,t_x)}{\partial t}$$

$$= h_0(x)\hat{\psi}_\alpha^\dagger(z,t_z)\hat{\psi}_\alpha(x,t_x) \tag{A17}$$

$$+ \hat{\psi}_\alpha^\dagger(z,t_z)\sum_{\beta'}\sum_{\delta'\gamma'}\int dy\,\hat{\psi}_{\beta'}^\dagger(y)v_{\alpha\beta'\delta'\gamma'}(x-y)\hat{\psi}_{\delta'}(y)\hat{\psi}_{\gamma'}(x)$$

which can be further expressed as

$$i\frac{\partial}{\partial t_x}\langle\hat{\psi}_\alpha^\dagger(z,t_z)\psi_\alpha(x,t_x)\rangle$$

$$= h_0(x)\langle\hat{\psi}_\alpha^\dagger(z,t_z)\psi_\alpha(x,t_x)\rangle \tag{A18}$$

$$+ \sum_{\beta'}\sum_{\delta'\gamma'}\int dy\cdot v_{\alpha\beta'\delta'\gamma'}(x-y)\langle\hat{\psi}_\alpha^\dagger(z,t_z)\hat{\psi}_\beta^\dagger(y,t_y)\hat{\psi}_{\delta'}(y)\hat{\psi}_{\gamma'}(x)\rangle$$

If $t_z \geq t_x$, we have

$$\left[i\frac{\partial}{\partial t}-h_0(x)\right]iG(x,z) = -\int dy\cdot v(x,y)G_2(x,y,y^+,z) \tag{A19}$$

If $t_z < t_x$, we have

$$\left[i\frac{\partial}{\partial t}-h_0(x)\right]G(x,z) = \delta(x-z)\delta(t_x-t_z) - i\int dy\cdot v(x,y)G_2(x,y,y^+,z) \tag{A20}$$

Finally, we can have the EOM of single-particle Green's function as the following form

$$\left[i\frac{\partial}{\partial t_1}-h_0(r_1)\right]G(1,2) + i\int d3\cdot v(1^+,3)G_2(1,3;2,3^+) = \delta(1,2) \tag{A21}$$

where h_0 is the same as the one used in EQUATION 2.67 in the main text. The first and second terms on the right-hand side of EQUATION A21 represent the non-interacting and interacting terms in the single-particle Green's function, respectively, where we assume the first term can be determined exactly by solving the independent-particle Green's function G_0 as we have already discussed in EQUATION 2.43 in the main text.[102]

APPENDIX B: DERIVATION OF THE QUASI-PARTICLE EQUATION

Inserting the Lehmann representation of Green's function, as in EQUATION 2.38, into the EOM

for the Green's function of a stationary system in the frequency domain

$$[\hbar\omega - \hat{h}_0(r_1)]G(r_1, r_2; \omega) - \int \Sigma(r_1, r_2; \omega)G(r_3, r_2; \omega)dr_3 = \delta(r_1 - r_2) \tag{A22}$$

which is equivalent to the Dyson's equation, yields

$$\sum_i \frac{\phi_i^*(r_2)}{\hbar\omega - \varepsilon_i \mp i\eta}\left\{[\hbar\omega - \hat{h}_0(r_1)]\phi_i(r_1) - \int \Sigma(r_1, r_2; \omega)\phi_i(r_3)dr_3\right\} = \delta(r_1 - r_2) \tag{A23}$$

Now, we multiply EQUATION A23 by $\left(\hbar\omega - \varepsilon_j\right)$ and take the limit $\omega \to \varepsilon_i$ on both sides. If we

assume that the system is nondegenerate (i.e. all ε_i are different), the left-hand side becomes

$$\lim_{\omega\to\varepsilon_i}\left(\hbar\omega - \varepsilon_j\right)\sum_i \frac{\phi_i^*(r_2)}{\hbar\omega - \varepsilon_i \mp i\eta}\left\{[\hbar\omega - \hat{h}_0(r_1)]\phi_i(r_1) - \int \Sigma(r_1, r_2; \omega)\phi_i(r_3)dr_3\right\}$$

$$= \phi_j^*(r_2)\left\{[\varepsilon_j - \hat{h}_0(r_1)]\phi_j(r_1) - \int \Sigma(r_1, r_2; \varepsilon_j)\phi_j(r_3)dr_3\right\} \tag{A24}$$

and the right-hand side becomes

$$\lim_{\omega\to\varepsilon_i}\left(\hbar\omega - \varepsilon_j\right)\delta(r_1 - r_2) = 0 \tag{A25}$$

Since $\phi_j^*(r_2)$ does not vanish for all position r_2, the expression in the curly bracket must be zero.

This leads directly to the quasi-particle equation as we had in EQUATION 2.68

$$\hat{h}_0(r_1)\phi_n(r_1) + \int \Sigma(r_1, r_2; \varepsilon_n)\phi_n(r_2)dr_2 = \varepsilon_n\phi_n(r_1) \tag{A26}$$

APPENDIX C: DERIVATION OF THE HEDIN'S EQUATIONS

In this section, we are going to show how to derive the Hedin's equations as given in EQUATION 2.70 to EQUATION 2.74 in the main text. Here, we closely follow Hedin's original work published in 1965.[102] One can find detailed discussions in Hedin's original paper.

Before we start, let's define some useful terms. First, we define the inverse Green's function G^{-1} as:

$$\int G(1,3)G^{-1}(3,2)d(3) = \delta(1,2) \tag{A27}$$

Then, we define the inverse dielectric function ϵ^{-1} as:

$$\epsilon^{-1}(1,2) = \frac{\delta V(1)}{\delta \phi(2)} \tag{A28}$$

which means the external potential change at position r_1, $\delta V(1)$, due to a small variation of the external potential at position r_2, $\delta \phi(2)$. One can also understand it as how the change at position r_2 will affect position r_1. We also define dielectric function ϵ as

$$\epsilon(1,2) = \frac{\delta \phi(1)}{\delta V(2)} \tag{A29}$$

Thus, we have

$$V(1) = \phi(1) + V_H(1)$$
$$= \phi(1) + \int \frac{n(r_3,t_1)}{|r_1 - r_3|} dr_3 \tag{A30}$$
$$= \phi(1) + \int v(1,3)n(r_3,t_1)dr_3$$

where n is the electron density and $v(1,3)$ is the Coulomb interaction between two particles that are located at position r_3 and r_1. The first and the second term on the right-hand side of EQUATION A30 represents the external potential and Hartree potential, respectively. We can use the short-hand

notation of $n(3)$ to represent the electron density at position r_3 where 3 represents position r_3.

Therefore, EQUATION A30 can be re-written in the following form:

$$V(1) = \phi(1) + \int v(1,3)n(3)d3 \tag{A31}$$

$$\delta V(1) = \delta\phi(1) + \int v(1,3)\delta n(3)d3 \tag{A32}$$

$$\frac{\delta V(1)}{\delta V(2)} = \frac{\delta\phi(1)}{\delta\phi(2)} + \int v(1,3)\frac{\delta n(3)}{\delta n(2)}d3 \tag{A33}$$

By using the dielectric function as defined in EQUATION A28, we then have

$$\epsilon^{-1}(1,2) = \delta(1,2) + \int v(1,3)P^{red}(3,2)d3 \tag{A34}$$

where $P^{red}(3,2)$ is defined as the reduced polarizability

$$P^{red}(3,2) = \frac{\delta n(3)}{\delta n(2)} \tag{A35}$$

Similar to V, we can do the same with ϕ. Here, we can reform EQUATION A31 in the following form

$$\phi(1) = V(1) - \int v(1,3)n(3)d3 \tag{A36}$$

$$\delta\phi(1) = \delta V(1) - \int v(1,3)\delta n(3)d3 \tag{A37}$$

$$\frac{\delta\phi(1)}{\delta V(2)} = \frac{\delta V(1)}{\delta V(2)} - \int v(1,3)\frac{\delta n(3)}{\delta V(2)}d3 \tag{A38}$$

By using the dielectric function as defined in EQUATION A29, we have

$$\epsilon(1,2) = \delta(1,2) - \int v(1,3)P(3,2)d3 \tag{A39}$$

where $P(3,2)$ is defined as the irreducible polarizability which has the following form

$$P(3,2) = \frac{\delta n(3)}{\delta V(2)} \tag{A40}$$

After all these useful terms defined, now we are ready to derive the Hedin's equations.

C.1 Screened Coulomb Potential W

Let's first define the screened Coulomb potential W as

$$W(1,2) = \int \epsilon^{-1}(1,3)v(3,2)d3 \tag{A41}$$

Inserting EQUATION A34 in to EQUATION A41, we have

$$W(1,2) = \int \left[\delta(1,3) + \int v(1,4)P^{red}(4,3)d4\right]v(3,2)d3$$

$$= \delta(1,3)\int v(3,2)d3 + \int\int v(1,4)P^{red}(4,3)v(3,2)d(3,4) \tag{A42}$$

where the first term on the right-hand side is non-zero only if $1 \equiv 3$. In the second term on the right-hand side, the 3 and 4 are indistinguishable, so we can switch 3 and 4 to obtain the following expression

$$W(1,2) = v(1,2) + \int\int v(1,3)P^{red}(3,4)v(4,2)d(3,4) \tag{A43}$$

Since we have already defined the reducible and irreducible polarizability as shown in EQUATION A35 and EQUATION A40, we now have the following expressions

$$\delta n(3) = P^{red}(3,4)\delta\phi(4) = P(3,4)\delta V(4) \tag{A44}$$

$$P^{red}(3,4) = \frac{P(3,4)\delta V(4)}{\delta\phi(4)}$$

$$= \frac{P(3,4)}{\delta\phi(4)}\frac{\delta V(4)}{\delta\phi(3)}\delta\phi(3) \tag{A45}$$

$$= P(3,4)\epsilon^{-1}(4,3)\frac{\delta\phi(3)}{\delta\phi(4)}$$

Inserting EQUATION A45 into EQUATION A43 we have

$$W(1,2) = v(1,2) + \int\int v(1,3)P(3,4)\epsilon^{-1}(4,3)\frac{\delta\phi(3)}{\delta\phi(4)}v(4,2)d(3,4)$$

$$= v(1,2) + \int\int v(1,3)P(3,4)\epsilon^{-1}(4,3)\delta(3,4)v(4,2)d(3,4) \tag{A46}$$

where EQUATION A46 is non-zero only if $3 \equiv 4$. Therefore, we have

$$W(1,2) = v(1,2) + \int\int v(1,3)P(3,4)\epsilon^{-1}(4,3)v(3,2)d(3,4) \tag{A47}$$

As we have already defined the screened coulomb potential in EQUATION A41, inserting it into EQUATION A47 we have the following form for screened Coulomb potential

$$W(1,2) = v(1,2) + \int\int v(1,3)P(3,4)W(4,2)d(3,4) \tag{A48}$$

C.2 Self-energy Σ

After the derivation of the screened Coulomb potential, we can easily acquire the derivation for self-energy term. We know the two-particle Green's function has the following form

$$i\hbar\frac{\partial}{\partial t_1}G(1,2) = \delta(1,2) + h(1)G(1,2) - i\hbar\int v(1^+,3)G(1,3;2,3^+)d3 \tag{A49}$$

Here, we have used the short-hand notation of $1 = (r_1, t_1)$ and $1^+ = (r_1, t_1 + \eta)$, where η is an infinitesimal positive time. For the functional derivative of the Green's function with respect to the change of the external potential we have[102]

$$\left.\frac{\delta G(1,2)}{\delta V(3)}\right|_{V=0} = G(1,2)G(3,3^+) - G(1,3;2,3^+) \tag{A50}$$

This allows us to eliminate the two-particle Green's function, as in EQUATION A49, and the integral part in EQUATION A49 becomes

$$-i\hbar\int v(1^+,3)G(1,3;2,3^+)d3$$

$$= -i\hbar\left(\int v(1,3)G(3,3^+)d3\right)G(1,2) + i\hbar\int v(1^+,3)\frac{G(1,2)}{\delta V(3)}d3 \tag{A51}$$

where the first term at the right-hand of $-i\hbar(\int v(1,3)G(3,3^+)d3)$ is the Hartree potential. Then, we have the following expression for the integral term in the two-particle Green's function by using the expression of self-energy in EQUATION 2.58 in the main text

$$-i\hbar\int v(1^+,3)G(1,3;2,3^+)d3 = V^H(1)G(1,2) + i\hbar\int \Sigma(1,3)G(3,2)d3 \tag{A52}$$

Therefore, by using the definition of the inverse Green's function, as in EQUATION A27, we have the following form for the self-energy term

$$\Sigma(1,2) = i\hbar \int \int v(1^+,3) \frac{\delta G(1,4)}{\delta V(3)} G^{-1}(4,2) d3 d4$$

$$= i\hbar \int \int v(1^+,3) G(1,4) \frac{\delta G^{-1}(4,2)}{\delta V(3)} d3 d4 \qquad (A53)$$

$$= i\hbar \int \int W(1^+,3) G(1,4) \Gamma(4,2;3) d3 d4$$

where Γ is the vertex function that we will discuss later.

C.3 Irreducible Polarizability P

Now we are going to derive the irreducible polarizability P that we have already introduced in EQUATION A40. From the field operator and the Green's function, we know the following relationships

$$n(r) = \langle \Phi_0^N | \hat{\psi}^\dagger \hat{\psi} | \Phi_0^N \rangle \qquad (A54)$$

and

$$G(r,r^+) = i \langle \Phi_0^N | \hat{\psi}^\dagger \hat{\psi} | \Phi_0^N \rangle \qquad (A55)$$

where Φ_0^N is the ground state many-body wave function for the system with N particles. Therefore, we have

$$n(r) = iG(r,r^+) \qquad (A56)$$

From EQUATION A40, we have

$$P(1,2) = \frac{\delta n(1)}{\delta V(2)} = \frac{\delta n(1,1^+)}{\delta V(2)} = i \frac{\delta G(1,1^+)}{\delta V(2)} \qquad (A57)$$

Now right multiply EQUATION A27 by $G(4,1^+)$ we have

$$\int G(1,3) G^{-1}(3,4) G(4,1^+) d(1,3,4) = \int \delta(1,4) G(4,1^+) d(1,4) \qquad (A58)$$

where EQUATION A58 is non-zero only if $1 \equiv 4$, and we have used a single integral symbol to represent a double or triple integral in the equation just for simplicity. Now taking the derivative with respect to $\delta V(2)$, the left-hand side (LHS) of EQUATION A58 becomes

$$LHS = \int \frac{\delta G(1,3)}{\delta V(2)} G^{-1}(3,4) G(4,1^+) d(1^+,3,4) + \int G(1,3) \frac{\delta G^{-1}(3,4)}{\delta V(2)} G(4,1^+) d(1^+,3,4)$$
$$+ \int G(1,3) G^{-1}(3,4) \frac{\delta G^{-1}(4,1^+)}{\delta V(2)} d(1^+,3,4) \tag{A59}$$
$$= \int G(1,3) \frac{\delta G^{-1}(3,4)}{\delta V(2)} G(4,1^+) d(1^+,3,4)$$

Since $t_1 \cong t_1^+$ and $1 \equiv 4$, we acquire

$$LHS = \int G(1,3) \frac{\delta G^{-1}(3,4)}{\delta V(2)} G(4,1) d(3,4) \tag{A60}$$

Similarly, we have the right-hand side (RHS) of EQUATION A58 as

$$RHS = \frac{\delta G(4,1^+)}{\delta V(2)} = \frac{\delta G(1,1^+)}{\delta V(2)} \tag{A61}$$

According to EQUATION A57, we can re-write EQUATION A61 as

$$RHS = \frac{P(1,2)}{i} \tag{A62}$$

Since $LHS = RHS$, it follows that

$$\int G(1,3) \frac{\delta G^{-1}(3,4)}{\delta V(2)} G(4,1) d(3,4) = \frac{P(1,2)}{i} \tag{A63}$$

Now we define vertex function Γ as

$$\Gamma(3,4;2) = -\frac{\delta G^{-1}(3,4)}{\delta V(2)} \tag{A64}$$

Then, we have the irreducible polarizability written as

$$P(1,2) = -i \int G(1,3) \Gamma(3,4;2) G(4,1) d(3,4) \tag{A65}$$

C.4 Vertex Function Γ

As we have defined the vertex function in EQUATION A64, when we change indices we have

$$\Gamma(1,2;3) = -\frac{\delta G^{-1}(1,2)}{\delta V(3)} \tag{A66}$$

Because we have the following relation between the inverse Green's function and the self-energy as in EQUATION 2.58 of the main text[102]

$$G^{-1} = G_0^{-1} - \Sigma \tag{A67}$$

where G is the one-particle interacting Green's function and G_0 is the one-particle non-interacting Green's function. Therefore, we can write the vertex function as

$$\Gamma(1,2;3) = -\frac{\delta G_0^{-1}(1,2)}{\delta V(3)} + \frac{\delta \Sigma(1,2)}{\delta V(3)} \tag{A68}$$

From the independent-particle Green's function G_0 as shown in EQUATION 2.43 of the main text, we have

$$\left[i\frac{\partial}{\partial t_1} - H_0(1) - V(1)\right] G_0(1,2) = \delta(1,2) \tag{A69}$$

$$\left[i\frac{\partial}{\partial t_1} - H_0(1) - V(1)\right] G_0(1,2) G_0^{-1}(2,3) = \delta(1,2) G_0^{-1}(2,3) \tag{A70}$$

$$\left[i\frac{\partial}{\partial t_1} - H_0(1) - V(1)\right] \int G_0(1,2) G_0^{-1}(2,3) d2 = \int \delta(1,2) G_0^{-1}(2,3) d2 \tag{A71}$$

$$\left[i\frac{\partial}{\partial t_1} - H_0(1) - V(1)\right] \delta(1,3) = \delta(1,2) G_0^{-1}(2,3) \tag{A72}$$

$$G_0^{-1}(2,3) = \left[i\frac{\partial}{\partial t_1} - H_0(1) - V(1)\right] \frac{\delta(1,3)}{\delta(1,2)} \tag{A73}$$

$$G_0^{-1}(2,3) = \left[i\frac{\partial}{\partial t_1} - H_0(1) - V(1)\right] \delta(2,3) \tag{A74}$$

We can re-write EQUATION A74 by using different indices as

$$G_0^{-1}(1,2) = \left[i\frac{\partial}{\partial t_1} - H_0(1) - V(1)\right] \delta(1,2) \tag{A75}$$

Therefore, we have

$$-\frac{G_0^{-1}(1,2)}{\delta V(3)} = \frac{\delta V(1)}{\delta V(3)}\delta(1,2) + V(1)\frac{\delta(1,2)}{\delta V(3)} \tag{A76}$$

The second term at the right-hand side of EQUATION A76 is 0 because

$$\delta(1,2) = \begin{cases} 0, when\ 1 \neq 2 \\ 1, when\ 1 = 2 \end{cases} \tag{A77}$$

which means $\delta(1,2)$ is always a constant, there is no change with a small external potential change

at position r_3. Hence, we have the following form

$$-\frac{G_0^{-1}(1,2)}{\delta V(3)} = \delta(1,2)\delta(1,3) \tag{A78}$$

By using chain-rule differentiation, we have the following expressions

$$\frac{\delta G(1,2)}{\delta\phi(3)} = -\int G(1,4)\frac{\delta G^{-1}(4,5)}{\delta\phi(3)}G(5,2)d(4,5) \tag{A79}$$

and

$$\frac{\delta G(1,2)}{\delta V(3)} = -\int G(1,4)\frac{\delta G^{-1}(4,5)}{\delta V(3)}G(5,2)d(4,5) \tag{A80}$$

Where, by using the definition of the vertex function, we have

$$\frac{\delta G(1,2)}{\delta V(3)} = -\int G(1,4)\Gamma(4,5;3)G(5,2)d(4,5) \tag{A81}$$

In addition, we can re-write the second term on the right-hand side of EQUATION A68 as

$$\frac{\delta\Sigma(1,2)}{\delta V(3)} = \frac{\delta\Sigma(1,2)}{\delta G(4,5)}\frac{\delta G(4,5)}{\delta V(3)} \tag{A82}$$

By using EQUATION A81, we can re-write EQUATION A82 as

$$\begin{aligned}\frac{\delta\Sigma(1,2)}{\delta V(3)} &= \frac{\delta\Sigma(1,2)}{\delta G(4,5)}\int G(4,6)\Gamma(6,7;3)G(7,5)d(6,7) \\ &= \int \frac{\delta\Sigma(1,2)}{\delta G(4,5)}G(4,6)\Gamma(6,7;3)G(7,5)d(6,7)\end{aligned} \tag{A83}$$

Inserting EQUATION A78 and EQUATION A83 into EQUATION A68, we can have

$$\Gamma(1,2;3) = \delta(1,2)\delta(1,3) + \int \frac{\delta\Sigma(1,2)}{\delta G(4,5)}G(4,6)\Gamma(6,7;3)G(7,5)d(6,7) \tag{A84}$$

116

Now, putting together EQUATION 2.29 from the main text, EQUATION A48, EQUATION A53, EQUATION A65, and EQUATION A84, we arrive at the Hedin's equations as shown in EQUATION 2.70 to EQUATION 2.74 in the main text.

REFERENCES

(1)   Kirk, A. P.; Fischetti, M. V., *Phys. Rev. B* **2012,** *86*, 165206.

(2)   Nozik, A. J.; Beard, M. C.; Luther, J. M.; Law, M.; Ellingson, R. J., et al., *Chem. Rev.* **2010,** *110*, 6873.

(3)   O'Regan, B.; Gratzel, M., *Nature* **1991,** *353*, 737.

(4)   Asbury, J. B.; Hao, E.; Wang, Y.; Ghosh, H. N.; Lian, T., *J. Phys. Chem. B* **2001,** *105*, 4545.

(5)   Gratzel, M., *Nature* **2001,** *414*, 338.

(6)   Gregg, B. A., *J. Phys. Chem. B* **2003,** *107*, 4688.

(7)   Shoute, L. C. T.; Loppnow, G. R., *J. Am. Chem. Soc.* **2003,** *125*, 15636.

(8)   Ardo, S.; Meyer, G. J., *Chem. Soc. Rev.* **2009,** *38*, 115.

(9)   Concepcion, J. J.; Jurss, J. W.; Brennaman, M. K.; Hoertz, P. G.; Patrocinio, A. O. T., et al., *Acc. Chem. Res.* **2009,** *42*, 1954.

(10)   Hagfeldt, A.; Boschloo, G.; Sun, L.; Kloo, L.; Pettersson, H., *Chem. Rev.* **2010,** *110*, 6595.

(11)   Nieto-Pescador, J.; Abraham, B.; Gundlach, L., *J. Phys. Chem. Lett.* **2014**, 3498.

(12)   Ross, R. T.; Nozik, A. J., *J. Appl. Phys.* **1982,** *53*, 3813.

(13)   Nozik, A. J., *Phys. E* **2002,** *14*, 115.

(14)   Colvin, V. L.; Schlamp, M. C.; Alivisatos, A. P., *Nature* **1994,** *370*, 354.

(15)   Zhao, J.; Bardecker, J. A.; Munro, A. M.; Liu, M. S.; Niu, Y., et al., *Nano Lett.* **2006,** *6*, 463.

(16) Knowles, K. E.; Tice, D. B.; McArthur, E. A.; Solomon, G. C.; Weiss, E. A., *J. Am. Chem. Soc.* **2010,** *132*, 1041.

(17) Morris-Cohen, A. J.; Frederick, M. T.; Cass, L. C.; Weiss, E. A., *J. Am. Chem. Soc.* **2011,** *133*, 10146.

(18) Würfel, P., *Sol. Energy Mater. Sol. Cells* **1997,** *46*, 43.

(19) Nozik, A. J., *Annu. Rev. Phys. Chem.* **2001,** *52*, 193.

(20) Pandey, A.; Guyot-Sionnest, P., *J. Phys. Chem. Lett.* **2010,** *1*, 45.

(21) Sambur, J. B.; Novet, T.; Parkinson, B. A., *Science* **2010,** *330*, 63.

(22) Tisdale, W. A.; Williams, K. J.; Timp, B. A.; Norris, D. J.; Aydil, E. S., et al., *Science* **2010,** *328*, 1543.

(23) Tisdale, W. A.; Zhu, X.-Y., *Proc. Natl. Acad. Sci.* **2011,** *108*, 965.

(24) Tian, Y.; Tatsuma, T., *J. Am. Chem. Soc.* **2005,** *127*, 7632.

(25) Furube, A.; Du, L.; Hara, K.; Katoh, R.; Tachiya, M., *J. Am. Chem. Soc.* **2007,** *129*, 14852.

(26) Wu, K.; Rodríguez-Córdoba, W. E.; Yang, Y.; Lian, T., *Nano Lett.* **2013,** *13*, 5255.

(27) Wu, K.; Chen, J.; McBride, J. R.; Lian, T., *Science* **2015,** *349*, 632.

(28) Tan, S.; Liu, L.; Dai, Y.; Ren, J.; Zhao, J., et al., *J. Am. Chem. Soc.* **2017,** *139*, 6160.

(29) Elenewski, J. E.; Cai, J. Y.; Jiang, W.; Chen, H., *J. Phys. Chem. C* **2016,** *120*, 20579.

(30) Li, L.; Kanai, Y., *J. Phys. Chem. Lett.* **2016,** *7*, 1495.

(31) Pelouch, W. S.; Ellingson, R. J.; Powers, P. E.; Tang, C. L.; Szmyd, D. M., et al., *Phys. Rev. B* **1992,** *45*, 1450.

(32)   Sercel, P. C., *Phys. Rev. B* **1995,** *51*, 14532.

(33)   Schroeter, D. F.; Griffiths, D. J.; Sercel, P. C., *Phys. Rev. B* **1996,** *54*, 1486.

(34)   Allan, G.; Delerue, C., *Phys. Rev. B* **2009,** *79*, 195324.

(35)   Cooney, R. R.; Sewall, S. L.; Anderson, K. E. H.; Dias, E. A.; Kambhampati, P., *Phys. Rev. Lett.* **2007,** *98*, 177403.

(36)   Cooney, R. R.; Sewall, S. L.; Dias, E. A.; Sagar, D. M.; Anderson, K. E. H., et al., *Phys. Rev. B* **2007,** *75*, 245311.

(37)   Guyot-Sionnest, P.; Wehrenberg, B.; Yu, D., *J. Chem. Phys.* **2005,** *123*, 074709.

(38)   Frederick, M. T.; Amin, V. A.; Weiss, E. A., *J. Phys. Chem. Lett.* **2013,** *4*, 634.

(39)   Peterson, M. D.; Cass, L. C.; Harris, R. D.; Edme, K.; Sung, K., et al., *Annu. Rev. Phys. Chem.* **2014,** *65*, 317.

(40)   Henderson, M. A.; White, J. M.; Uetsuka, H.; Onishi, H., *J. Am. Chem. Soc.* **2003,** *125*, 14974.

(41)   Graetzel, M.; Janssen, R. A. J.; Mitzi, D. B.; Sargent, E. H., *Nature* **2012,** *488*, 304.

(42)   Prezhdo, O. V.; Duncan, W. R.; Prezhdo, V. V., *Acc. Chem. Res.* **2008,** *41*, 339.

(43)   Akimov, A. V.; Neukirch, A. J.; Prezhdo, O. V., *Chem. Rev.* **2013,** *113*, 4496.

(44)   Prezhdo, O. V.; Duncan, W. R.; Prezhdo, V. V., *Prog. Surf. Sci.* **2009,** *84*, 30.

(45)   Zhang, Z.; Yates, J. T., *Chem. Rev.* **2012,** *112*, 5520.

(46)   Tully, J. C., *J. Chem. Phys.* **1990,** *93*, 1061.

(47) Man, M. K. L.; Margiolakis, A.; Deckoff-Jones, S.; Harada, T.; Wong, E. L., et al., *Nat. Nanotechnol.* **2017,** *12*, 36.

(48) Petek, H., *Nat. Nanotechnol.* **2017,** *12*, 3.

(49) Malliaras, G.; Friend, R., *Phys. Today* **2005,** *58*, 53.

(50) Ramakrishna, S.; Willig, F.; May, V., *J. Chem. Phys.* **2001,** *115*, 2743.

(51) Ramakrishna, S.; Willig, F.; May, V.; Knorr, A., *J. Phys. Chem. B* **2003,** *107*, 607.

(52) Wang, H.; Thoss, M., *J. Phys. Chem. A* **2003,** *107*, 2126.

(53) Thoss, M.; Kondov, I.; Wang, H., *Chem. Phys.* **2004,** *304*, 169.

(54) Wang, L.; Willig, F.; May, V., *J. Chem. Phys.* **2006,** *124*, 014712.

(55) Kondov, I.; Čížek, M.; Benesch, C.; Wang, H.; Thoss, M., *J. Phys. Chem. C* **2007,** *111*, 11970.

(56) Wang, L.; Willig, F.; May, V., *J. Chem. Phys.* **2007,** *126*, 134110.

(57) Fischetti, M. V.; Laux, S. E.; Crabbé, E., *J. Appl. Phys.* **1995,** *78*, 1058.

(58) Sjodin, T.; Petek, H.; Dai, H.-L., *Phys. Rev. Lett.* **1998,** *81*, 5664.

(59) Ichibayashi, T.; Tanimura, K., *Phys. Rev. Lett.* **2009,** *102*, 087403.

(60) Buriak, J. M.; Sikder, M. D. H., *J. Am. Chem. Soc.* **2015,** *137*, 9730.

(61) Parandekar, P. V.; Tully, J. C., *J. Chem. Phys.* **2005,** *122*, 094102.

(62) Knauf, R. R.; Brennaman, M. K.; Alibabaei, L.; Norris, M. R.; Dempsey, J. L., *J. Phys. Chem. C* **2013,** *117*, 25259.

(63)   Ashford, D. L.; Gish, M. K.; Vannucci, A. K.; Brennaman, M. K.; Templeton, J. L., et al., *Chem. Rev.* **2015,** *115*, 13006.

(64)   Farnum, B. H.; Morseth, Z. A.; Lapides, A. M.; Rieth, A. J.; Hoertz, P. G., et al., *J. Am. Chem. Soc.* **2014,** *136*, 2208.

(65)   Yang, Y.; Liu, Z.; Lian, T., *Nano Lett.* **2013,** *13*, 3678.

(66)   Green, A. N. M.; Palomares, E.; Haque, S. A.; Kroon, J. M.; Durrant, J. R., *J. Phys. Chem. B* **2005,** *109*, 12525.

(67)   Akbari, A.; Berini, P., *Appl. Phys. Lett.* **2009,** *95*, 021104.

(68)   Sun, D.; Aivazian, G.; Jones, A. M.; Ross, J. S.; Yao, W., et al., *Nat. Nanotechnol.* **2012,** *7*, 114.

(69)   Sobhani, A.; Knight, M. W.; Wang, Y.; Zheng, B.; King, N. S., et al., *Nat. Commun.* **2013,** *4*, 1643.

(70)   Brongersma, M. L.; Halas, N. J.; Nordlander, P., *Nat. Nanotechnol.* **2015,** *10*, 25.

(71)   Atwater, H. A.; Polman, A., *Nat. Mater.* **2010,** *9*, 205.

(72)   Clavero, C., *Nat. Photonics* **2014,** *8*, 95.

(73)   Yu, S.; Kim, Y. H.; Lee, S. Y.; Song, H. D.; Yi, J., *Angew. Chem., Int. Ed.* **2014,** *126*, 11385.

(74)   Linic, S.; Christopher, P.; Ingram, D. B., *Nat. Mater.* **2011,** *10*, 911.

(75)   Abuabara, S. G.; Rego, L. G. C.; Batista, V. S., *J. Am. Chem. Soc.* **2005,** *127*, 18234.

(76)   Hammes-Schiffer, S.; Tully, J. C., *J. Chem. Phys.* **1994,** *101*, 4657.

(77)   Barbatti, M.; Crespo-Otero, R., Surface Hopping Dynamics with DFT Excited States. In *Density-Functional Methods for Excited States*, Ferré, N.; Filatov, M.; Huix-Rotllant, M., Eds. Springer International Publishing: Cham, 2016; pp 415.

(78)   Lin, Y.; Akimov, A. V., *J. Phys. Chem. A* **2016,** *120*, 9028.

(79)   Drukker, K., *J. Comput. Phys.* **1999,** *153*, 225.

(80)   Doltsinis, N. L.; Marx, D., *Phys. Rev. Lett.* **2002,** *88*, 166402.

(81)   Hammes-Schiffer, S.; Stuchebrukhov, A. A., *Chem. Rev.* **2010,** *110*, 6939.

(82)   Duncan, W. R.; Stier, W. M.; Prezhdo, O. V., *J. Am. Chem. Soc.* **2005,** *127*, 7941.

(83)   Jakubikova, E.; Snoeberger Iii, R. C.; Batista, V. S.; Martin, R. L.; Batista, E. R., *J. Phys. Chem. A* **2009,** *113*, 12532.

(84)   Kolesov, G.; Vinichenko, D.; Tritsaris, G. A.; Friend, C. M.; Kaxiras, E., *J. Phys. Chem. Lett.* **2015,** *6*, 1624.

(85)   Long, R.; Prezhdo, O. V., *J. Am. Chem. Soc.* **2011,** *133*, 19240.

(86)   Han, Y.; Tretiak, S.; Kilin, D., *Mol. Phys.* **2014,** *112*, 474.

(87)   Tritsaris, G. A.; Vinichenko, D.; Kolesov, G.; Friend, C. M.; Kaxiras, E., *J. Phys. Chem. C* **2014,** *118*, 27393.

(88)   Li, Y.; Galli, G., *Phys. Rev. B* **2010,** *82*, 045321.

(89)   Wippermann, S.; Vörös, M.; Rocca, D.; Gali, A.; Zimanyi, G., et al., *Phys. Rev. Lett.* **2013,** *110*, 046804.

(90)   Tully, J. C.; Preston, R. K., *J. Chem. Phys.* **1971,** *55*, 562.

(91)   Von Neumann, J., *Mathematical foundations of quantum mechanics*. Princeton university press: 1955.

(92)   Hu, C.; Sugino, O.; Hirai, H.; Tateyama, Y., *Phys. Rev. A* **2010,** *82*, 062508.

(93)   Reeves, K. G.; Schleife, A.; Correa, A. A.; Kanai, Y., *Nano Lett.* **2015,** *15*, 6429.

(94)   Parr, R. G., *Density-functional theory of atoms and molecules*. Clarendon Press; Oxford University Press: Oxford [England]; New York, 1989.

(95)   Kohanoff, J. J., *Electronic structure calculations for solids and molecules : theory and computational methods*. Cambridge University Press: Cambridge, UK ;New York, 2006.

(96)   Kohn, W.; Sham, L. J., *Phys. Rev.* **1965,** *140*, A1133.

(97)   Car, R.; de Angelis, F.; Giannozzi, P.; Marzari, N., First-Principles Molecular Dynamics. In *Handbook of Materials Modeling: Methods*, Yip, S., Ed. Springer Netherlands: Dordrecht, 2005; pp 59.

(98)   Feynman, R. P., *Phys. Rev.* **1939,** *56*, 340.

(99)   Fetter, A. L., *Quantum theory of many-particle systems*. San Francisco, McGraw-Hill [c1971]: 1971.

(100)   Ping, Y.; Rocca, D.; Galli, G., *Chem. Soc. Rev.* **2013,** *42*, 2437.

(101)   Mattuck, R. D., *A guide to Feynman diagrams in the many-body problem*. McGraw-Hill: New York, 1976.

(102)   Hedin, L., *Phys. Rev.* **1965,** *139*, A796.

(103)   Hedin, L.; Lundqvist, S., Effects of Electron-Electron and Electron-Phonon Interactions on the One-Electron States of Solids. In *Solid State Physics*, Frederick Seitz, D. T.; Henry, E., Eds. Academic Press: 1970; Vol. Volume 23, pp 1.

(104)   Adler, S. L., *Phys. Rev.* **1962,** *126*, 413.

(105)   Wiser, N., *Phys. Rev.* **1963,** *129*, 62.

(106)   Hybertsen, M. S.; Louie, S. G., *Phys. Rev. Lett.* **1985,** *55*, 1418.

(107)   Hybertsen, M. S.; Louie, S. G., *Phys. Rev. B* **1986,** *34*, 5390.

(108)   Onida, G.; Reining, L.; Rubio, A., *Rev. Mod. Phys.* **2002,** *74*, 601.

(109)   Yang, Y.; Rodríguez-Córdoba, W.; Lian, T., *J. Am. Chem. Soc.* **2011,** *133*, 9246.

(110)   Okano, M.; Sakamoto, M.; Teranishi, T.; Kanemitsu, Y., *J. Phys. Chem. Lett.* **2014,** *5*, 2951.

(111)   Perdew, J. P.; Burke, K.; Ernzerhof, M., *Phys. Rev. Lett.* **1996,** *77*, 3865.

(112)   Hamann, D. R.; Schlüter, M.; Chiang, C., *Phys. Rev. Lett.* **1979,** *43*, 1494.

(113)   Gygi, F., *IBM J. Res. Dev.* **2008,** *52*, 137.

(114)   Paolo, G.; Stefano, B.; Nicola, B.; Matteo, C.; Roberto, C., et al., *J. Phys.: Condens. Matter* **2009,** *21*, 395502.

(115)   Marini, A.; Hogan, C.; Grüning, M.; Varsano, D., *Comput. Phys. Commun.* **2009,** *180*, 1392.

(116)   Godby, R. W.; Needs, R. J., *Phys. Rev. Lett.* **1989,** *62*, 1169.

(117)   Oschlies, A.; Godby, R. W.; Needs, R. J., *Phys. Rev. B* **1995,** *51*, 1527.

(118)   Doany, F. E.; Grischkowsky, D.; Chi, C. C., *Appl. Phys. Lett.* **1987,** *50*, 460.

(119)   Doany, F. E.; Grischkowsky, D., *Appl. Phys. Lett.* **1988,** *52*, 36.

(120)   Jeong, S.; Zacharias, H.; Bokor, J., *Phys. Rev. B* **1996,** *54*, R17300.

(121)   Goldman, J. R.; Prybyla, J. A., *Phys. Rev. Lett.* **1994,** *72*, 1364.

(122)   Higashi, G. S.; Chabal, Y. J.; Trucks, G. W.; Raghavachari, K., *Appl. Phys. Lett.* **1990,** *56*, 656.

(123)   Car, R.; Parrinello, M., *Phys. Rev. Lett.* **1985,** *55*, 2471.

(124)   Li, L.; Wong, J. C.; Kanai, Y., *J. Chem. Theory Comput.* **2017,** *13*, 2634.

(125)   Bernardi, M.; Vigil-Fowler, D.; Lischner, J.; Neaton, J. B.; Louie, S. G., *Phys. Rev. Lett.* **2014,** *112*, 257402.

(126)   Jhalani, V. A.; Zhou, J.-J.; Bernardi, M., *Nano Lett.* **2017,** *17*, 5012.

(127)   Bernardi, M., *Eur. Phys. J. B* **2016,** *89*, 239.

(128)   Huber, R.; Moser, J.-E.; Grätzel, M.; Wachtveitl, J., *J. Phys. Chem. B* **2002,** *106*, 6494.

(129)   Stier, W.; Duncan, W. R.; Prezhdo, O. V., *Adv. Mater.* **2004,** *16*, 240.

(130)   Boschloo, G.; Hagfeldt, A., *Acc. Chem. Res.* **2009,** *42*, 1819.

(131)   Cánovas, E.; Wang, H.; Karakus, M.; Bonn, M., *Chem. Phys.* **2016,** *471*, 54.

(132)   Ren, J.; Vukmirović, N.; Wang, L.-W., *Phys. Rev. B* **2013,** *87*, 205117.

(133)   Perdew, J. P.; Ernzerhof, M.; Burke, K., *J. Chem. Phys.* **1996,** *105*, 9982.

(134)   Adamo, C.; Barone, V., *J. Chem. Phys.* **1999,** *110*, 6158.

(135)   Heyd, J.; Scuseria, G. E.; Ernzerhof, M., *J. Chem. Phys.* **2003,** *118*, 8207.

(136)   Heyd, J.; Scuseria, G. E., *J. Chem. Phys.* **2004,** *120*, 7274.

(137)   Heyd, J.; Scuseria, G. E., *J. Chem. Phys.* **2004,** *121*, 1187.

(138)   Heyd, J.; Peralta, J. E.; Scuseria, G. E.; Martin, R. L., *J. Chem. Phys.* **2005,** *123*, 174101.

(139)   Mori-Sanchez, P.; Cohen, A. J.; Yang, W., *J. Chem. Phys.* **2006,** *124*, 091102.

(140)   Cohen, A. J.; Mori-Sanchez, P.; Yang, W., *J. Chem. Phys.* **2007,** *126*, 191109.

(141)   Gygi, F., *Phys. Rev. Lett.* **2009,** *102*, 166406.

(142)   Gygi, F.; Duchemin, I., *J. Chem. Theory Comput.* **2013,** *9*, 582.

(143)   Govoni, M.; Galli, G., *J. Chem. Theory Comput.* **2015,** *11*, 2680.

(144)   Chernyak, V.; Mukamel, S., *J. Chem. Phys.* **2000,** *112*, 3572.

(145)   Hu, C.; Hirai, H.; Sugino, O., *J. Chem. Phys.* **2007,** *127*, 064103.

(146)   Tavernelli, I.; Curchod, B. F. E.; Rothlisberger, U., *J. Chem. Phys.* **2009,** *131*, 196101.

(147)   Tavernelli, I.; Tapavicza, E.; Rothlisberger, U., *J. Chem. Phys.* **2009,** *130*, 124107.

(148)   Tavernelli, I.; Curchod, B. F. E.; Laktionov, A.; Rothlisberger, U., *J. Chem. Phys.* **2010,** *133*, 194104.

(149)   Proetto, C., *Phys. Rev. A* **2013,** *88*, 056501.

(150)   Ou, Q.; Fatehi, S.; Alguire, E.; Shao, Y.; Subotnik, J. E., *J. Chem. Phys.* **2014,** *141*, 024114.

(151)   Friedrich, C.; Schindlmayr, A., *NIC Series* **2006**, 335.

(152)   Zhang, D.; Steinmann, S. N.; Yang, W., *J. Chem. Phys.* **2013,** *139*, 154109.